Dielectric properties of carbon nanotube-BaTiO hybrids reinforced PVDF composites

Benhui Fan

THESE DE DOCTORAT
DE
L'UNIVERSITE PARIS-SACLAY
PREPAREE A
"CentraleSupélec"

ECOLE DOCTORALE N° 579
Sciences mécaniques et énergétiques, matériaux et géosciences

Spécialité de doctorat : génie mécanique

Par

Mlle. Benhui, Fan

Propriétés diélectriques des composites à matrice PVDF comportant des renforts hybrides nano/micro-échelles (nanotubes de carbone et BaTiO$_3$)

Thèse présentée et soutenue à Châtenay-Malabry, 16 Novembre 2015:

Composition du Jury :

M., Lubineau, Gilles	Professeur, KAUST	Président
M., Sylvestre, Alain	Professeur, G2Elab	Rapporteur
M., Jestin, Jacques	Chargé de recherche, HDR, CEA	Rapporteur
M., Bedoui, Fahmi	Maître de conférence, HDR, UTC	Examinateur
Mme. Barrau, Sophie	Maître de conférence, Univ. Lille 1	Examinatrice
M. Pruvost, Sébastien	Maître de conférence, INSA Lyon	Examinateur
M. Bai, Jinbo	Directeur de Recherche, CentraleSupeléc	Directeur de thèse

Titre : Propriétés diélectriques des composites à matrice PVDF comportant des renforts hybrides nano/micro-échelles (nanotubes de carbone et BaTiO₃)

Mots clés : propriétés diélectriques, dispersion, structure, le traitement thermique

Résumé : La dispersion des nanotubes de carbone (NTC) dans le polyfluorure de vinylidène (PVDF) est un grand défi pour avoir de meilleures propriétés diélectriques. Les hybrides, titanate de baryum (BT)-NTC, ayant une structure particulière sont révélés être efficaces pour l'amélioration de la dispersion de NTC dans la matrice de polymère et la réduction du seuil de percolation du matériau composite. Cette thèse vise à atteindre une haute performance diélectrique du composite via la conception de charges ayant une structure favorable ainsi que l'étude exhaustive de l'interaction entre les NTC et la matrice de polymère semi-cristallin.

Dans le chapitre 1, un bref revu de l'état de l'art sur le contexte général des matériaux diélectrique est introduite ainsi les progrès récents dans ce domaine sont présentés pour mieux comprendre les composites et leurs application.

Dans le chapitre 2, nous préparons deux types d'hybrides avec deux structures différentes. Les premiers hybrides sont préparés par un dépôt chimique en phase vapeur (CVD). Les BT forment le noyau de ces hybrides et les NTC croient dessus (H-NTC-BT). Les deuxième hybrides sont préparées par réaction hydrothermale où NTC sont revêtus par les BT (H-BT-NTC). Par la suite, nous préparons des composites avec une matrice de PVDF renforcés par les deux types d'hybrides déjà synthétisés cela en coulant la solution puis par extrusion-injection. En outre, les méthodes de caractérisation de la morphologie, des propriétés thermiques, diélectriques et la cristallisation sont également introduites dans ce chapitre.

Dans le chapitre 3, les comportements diélectriques de H-NTC-BT/PVDF sont étudiés en détails. Une augmentation dramatique de la permittivité diélectrique est observée après le traitement thermique. Ce changement peut être dû à la réorganisation du réseau conducteur de NTC et la recristallisation de PVDF. Par la modélisation et la caractérisation expérimentale, Nous déduisons que cette augmentation significative de la permittivité diélectrique après le traitement thermique est dû au rétrécissement de la distance de NTC dans des couches amorphes voisine de PVDF d'un côte et au polymorphe β à l'interface NTC-PVDF d'un autre.

Dans le chapitre 4, la dispersion des NTC dans la matrice du composite PVDF est étudiée par la conception de différentes structures. Tout d'abord, une comparaison du seuil de percolation de H-NTC-BT/PVDF calculé et celui déterminé expérimentalement est menée pour mieux comprendre la morphologie de H-NTC-BT. Ensuite, deux comparaisons sont menées:

- La première compare les facteurs de transformation de la dispersion des NTC dans les composites H-NTC-BT/PVDF et NTC/PVDF cela en mesurant de la conductivité AC dans les différentes couches de ces composites.

- La deuxième compare trois types de composites de PVDF renforcés par des hybrides ayant la même fraction volumique de NTC et BT mais des structures différentes. L'effet de ces différentes structures de ces hybrides est étudié en comparant leurs propriétés diélectriques.

Pour finir conclusions générales sont présentées dans le chapitre 5 ainsi les perspectives prévues pour les travaux futurs.

Title : Dielectric properties of carbon nanotube-BaTiO3 hybrids reinforced PVDF composites

Keywords : Dielectric properties, dispersion, structure, thermal treatment

Abstract: The dispersion of carbon nanotube (CNT) in polyvinylidene fluoride (PVDF) is always a big challenge for the high dielectric property. CNT-barium titanate (BT) hybrids with the special structure are proved to be effective for improving the dispersion of CNT in polymer matrix and reduce the percolation threshold of composite. This thesis aims to achieve high dielectric performance of composites via designing fillers with the favorable structure as well as comprehensively study interactions between CNT and semi-crystalline polymer matrix.

In chapter 1, we provide a general introduction about dielectric material's background knowledge. Meanwhile the development including recent breakthroughs and their applications for dielectric field are also provided in this chapter.

In chapter 2, we prepare two hybrids with different structures. The first hybrids are prepared by chemical vapor deposition (CVD) method. It is with the structure of BT as a core and CNTs growing outsides (H-CNT-BT). The second hybrids are prepared by hydrothermal reaction where BT particles are coated outside CNT (H-BT-CNT). Meanwhile, we fabricate hybrids reinforced PVDF matrix composites by solution casting plus extrusion-injection way. Additionally, methods for characterization involving morphology, thermal and dielectric properties as well as crystallization are also introduced in this chapter.

In chapter 3, dielectric behaviors of H-CNT-BT/PVDF are studied concretely. A dramatic increment on dielectric permittivity is observed after thermal treatment. This change may result from the change of CNT's conductive network and the behavior of PVDF's re-crystallization. By calculating work and experimental characterization, the shrinkage of neighboring CNT's distance in PVDF's amorhous layers and the induced β polymorph at CNT-PVDF interface may cause the significant increment in dielectric permittivity after thermal treatment.

In chapter 4, CNT's dispersion in PVDF matrix composites is studied by designing different structures. Firstly, a comparison between calculated and experimental percolation threshold of H-CNT-BT/PVDF is conducted for studying morphology parameters of H-CNT-BT. Afterwards, two comparisons are conducted: one is between H-CNT-BT/PVDF and CNT/PVDF. Processing factors for CNT's dispersion are discussed via measuring different depth's AC conductivity from out layer to core. The other is among three hybrids reinforced PVDF composites. Hybrids structure's effect on CNT's dispersion is discussed via comparing dielectric properties of composites with same volume fractions of CNT and BT but different structures.

In chapter 5, general conclusions are formed according to works and perspectives are provided for the improvement of the future work.

Acknowledgement

Firstly, I would like to express my sincere gratitude to my supervisor Mr. Jinbo Bai for continuous support on my Ph.D study and related research works, for his patience and motivation. Otherwise, I could not finish my thesis. Meanwhile, I would also like to take this opportunity to express my gratitude to the financial support from China Scholarship Council (CSC).

Besides my supervisor, I would like to thank the rest of my thesis committees: Prof. Alain Sylvestre, Prof. Jacques Jestin, Prof. Gilles Lubineau, Dr. Fahmi Bedoui, Dr. Sébastien Pruvost and Dr. Sophie Barrau, for their insightful comments which help me to improve the quality of my thesis.

Then I would like to thank my master's supervisor Prof. Zhimin Dang for recommending me to do Ph.D studying in Jinbo's group. My sincere thanks also go to Prof. Guohua Hu for his helpful suggestions on polymer processing as well as continuous encouragement and care for my life in France.

I also thank engineers of laboratory who have helped me to do measurements: Françoise Garnier for SEM, Paul Haghi-Ashtiani for STEM and EDS, Pascale Gemeiner for Raman and Nicolas Guiblin for XRD. Meanwhile, I also thank Farida Djebbari, Sokona Konate, Ecri Perrin, Gilbert Le Gal and Thomas Reiss.

Additionally, I am also grateful to labmates for their help on my research work: Hang Zhao, Ahlem Raies, Yang Ma, Lu Liu, Xiaoxin Lu, Wang Chow, Xue Bai, Wenlong Wang, etc. In particular, I am grateful to Dr. Diana Salem, Dr. Lynda Belkadi, Dr. Delong He and my former colleague, Dr. Tao Zhou, for their careful correction on my thesis as well as my university classmate, Wanghui Chen, for the discussion and support to my study.

Last but not the least, I would like to thank my parents for their accompaniments and comforts especially when I am in low mood. Their smile and sweet words are so magic for me to face difficulties bravely in my life.

Content

Acronyms

AC	Alternating current
BT	Barium titanate
CNT	Carbon nanotube
CTE	Coefficient of thermal expansion
CVD	Chemical vapor deposition
DC	Direct Current
DFT	Density functional theory
DMAc	Dimethyl acetamide
DMF	Dimethyl formamide
DSC	Differential scanning calorimetry
EDS	Energy-dispersive X-ray spectroscopy
FTIR	Fourier transform infrared spectrometer
H-BT-CNT	Hybrids barium titanate-carbon nanotube
H-CNT-BT	Hybrids carbon nanotube-barium titanate
LBL	Layer-by-layer
M- CNT/BT	Mechanical mixing of carbon nanotube/barium titanate
MWNT	Multi-wall carbon nanotube
MD	Molecular dynamics
PA	Polyamide
PANI	Polyaniline
PC	Polycarbonate
PET	Polyester
PMMA	Poly(methyl methacrylate)
PPS	Polyphenylene sulfide
PVDF	Polyvinylidene fluoride
PVP	Polyvinyl pyrrolidone
PVT	Pressure-volume-temperature
SEM	Scanning electron microscope
STEM	Scanning transmission electron microscope
SAXS	Small-angle X-ray scattering
TEM	Transmission electron microscope

Tg	Glass transition temperature
TGA	Thermal gravimetric analysis
TrFE	Trifluoroethylene
WAXD	Wide-angle X-ray diffraction
XRD	X-ray diffraction

Symbols

Chapter 1

C	Capacitor
A	Area of plate for a parallel plate capacitor
d	Distance between two plates of parallel plate capacitor
ε_0	Absolute permittivity
Q	Charge on the electrode
ε_r	Relative dielectric permittivity
p	Electric dipole moment
a	Vector from the negative charge to the positive charge
E	Strength of electric field
ε_r'	Real part of dielectric permittivity
ε_r''	Imaginary part of dielectric permittivity
$tan\delta$	Dielectric loss tangent
E_b	Dielectric strength
ε_{eff}	Dielectric permittivity for the composite
ε_m	Dielectric permittivity for the matrix
ε_f	Dielectric permittivity for the filler
φ	Volume fraction of the filler
q	Critical exponent in percolation threshold
f	Volume fraction of conductive filler
f_c	Percolation threshold
d	Diameter of the filler
t	Thickness of interface

Chapter 2

$\Delta_f G^o$	Gibbs function of reaction
K	Equilibrium constant
R	Ideal gas constant
Q	Reaction quotient
T	Temperature

Chapter 3

$f_{H\text{-}CNT\text{-}BT}$	Volume fraction of H-CNT-BT
f_{CNT}	Volume fraction of CNT
f_{BT}	Volume fraction of BT
ε'	Relative dielectric permittivity
$tan\delta$	Dielectric loss
R_t	Tunneling resistance
σ_t	Tunneling conductivity
e	The elementary charge
h	Planck's constant
A	Cross-section area of the junction
λ	Tunneling energy barrier height
Z	Impedance
R	Resistance
C	Capacitor
s	Parameter of frequency
σ	Conductivity
φ	Ratio of CNT's resistance and tunneling resistance
ρ	Resistivity
d	Distance between neighboring CNTs
I_c	Intensity of crystalline diffraction
I_a	Intensity of amorphous halo
$Xc\%$	Crystallinity
q	Momentum transfer or scattering vector
$\beta\%$	Content of β polymorph in the PVDF crystallinity
L_a	Thickness of amorphous layer
L_c	Thickness of crystalline lamellae
L_p	Thickness of long period

Chapter 4

V_{ex}	Excluded volume
V_{core}	Volume of core
$V_{total\,BT}$	Total BT volume in H-CNT-BT
$V_{total\,CNT}$	Total CNT volume in H-CNT-BT
$V_{single\,BT}$	Single BT volume in H-CNT-BT
$V_{single\,CNT}$	Single BT volume in H-CNT-BT
i	Thickness of the interface outside the particle
r_p	Radius of BT particle

r_c	Radius of CNT
r_{c+i}	Radius of CNT with a polymer interface
t	Ratio of CNT with a hard core and a soft shell
l	Length of CNT
a	Aspect ratio
w_t	Weight fraction of CNT in H-CNT-BT
n	Number of CNTs on a single BT particle
N_A	Avogadro constant
$N_{total\ BT}$	Whole number of BT
$N_{total\ CNT}$	Whole number of CNT
M_{BT}	Molar mass of BT
ρ_{CNT}	Density of CNT
ρ_{BT}	Density of BT
q_p	Inversely proportional
s	Effective length of CNT in H-CNT-BT
m	Modified factor

Chapter 1 General Introduction

_____

Introduction

In this chapter, we review basic knowledge of dielectric theory and materials with high dielectric performance applied for nanocomposites. Theoretical models for calculating composite's dielectric permittivity, percolative behavior and interface property are also introduced for better understanding dielectric property of nanocomposites. Meanwhile, we also provide recent developments on dispersing carbon nanotubes and processing polymer matrix composites in order to provide a background for progresses as well as problems existing in this field. Additionally, the nature of polyvinylidene fluoride including molecular chains, crystallization and the crystalline transition are also illustrated comprehensively in the last part of this chapter.

1.1 Dielectric property

1.1.1 Dielectric permittivity and polarization

The parallel plate capacitor equation with free space as an insulator is given by

$$C = \frac{\varepsilon_0 A}{d}$$

where ε_0 is the absolute permittivity ($8.854 \times 10^{-12} F/m$), A is the plate area and d is the separation between two plates. The structure is shown in *Figure 1.1*. If there is a material medium between two plates, then the capacitance (the charge storage ability per unit voltage) will increase by the factor of ε_r, where ε_r is called the dielectric constant of medium or its relative permittivity.

Conductive plates

A dielectric material is placed between two conducting plates (electrodes), each of area A and with a separation of d
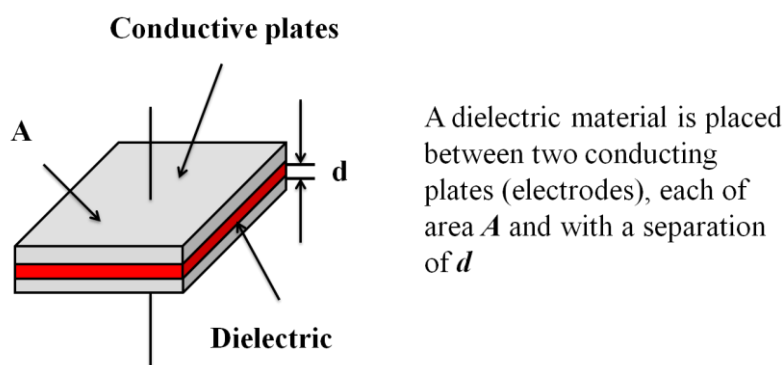
Dielectric

Figure 1.1 The common structure of the plate capacitor

Consider what happens when a dielectric slab (a slab of any non-conductive material) is inserted into a parallel plate capacitor, as shown in *Figure 1.2*. During the insertion of dielectric slab, there is an external current flow which indicates that an addition charge is stored on both plates. The charge on electrodes increases from Q_0 to Q. The relative permittivity ε_r is also defined to reflect this increase in the capacitance due to a dielectric medium.

$$\varepsilon_r = \frac{Q}{Q_0} = \frac{C}{C_0}$$
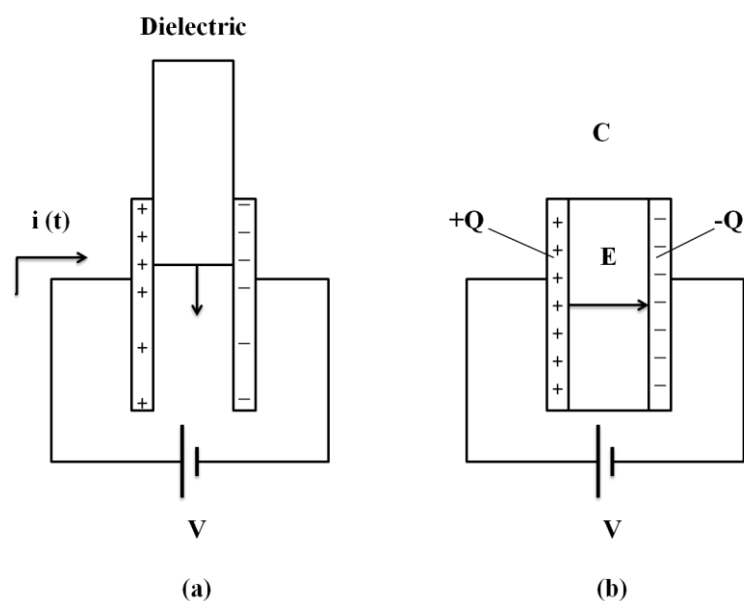
Figure.1.2 (a) As a slab of insulating material is inserted between two plates, there is an external current flow indicating that more charge is stored on the plates. **(b)** The capacitance has been increased due to the insertion of a medium between the plates. [1]

The increment in the stored charge is due to the polarization of medium where positive and negative charges are displaced from their equilibrium positions. Usually, the polarization can be divided into four kinds:

(1) Electric polarization

An electric dipole moment p is a simply separation between a negative and a positive charge with equal magnitude Q. If a is the vector from the negative charge to the positive one, the electric dipole moment is defined as a vector by

$$p = Qa$$

For a neutral atom, the net charge is zero. However, on the average, a neutral atom is rarely found and the atom usually has net dipole moment. When the atom is in an external electric field, an induced dipole moment will be developed. The electrons become easily displaced by the field because they are much lighter than the positive nucleus. Thus, as shown in *Figure 1.3*, the separation of negative charge center from positive one results in an induced dipole moment termed as the electric polarization.

7
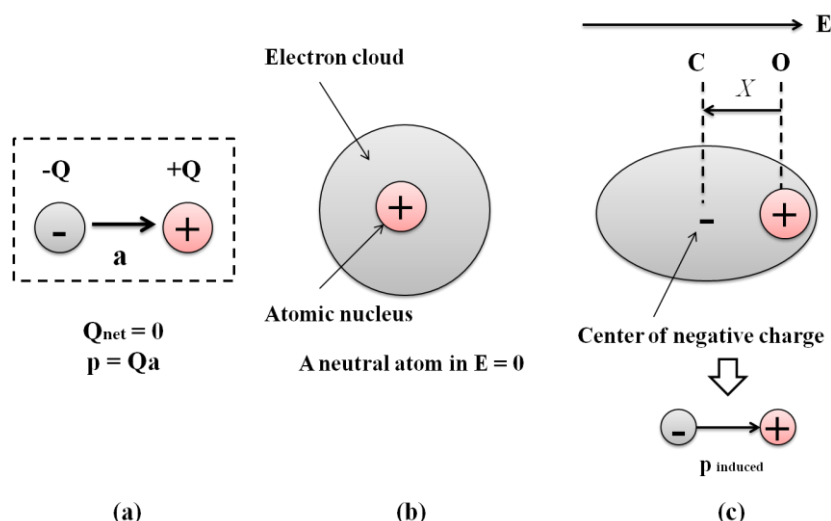
Figure 1.3 (a) is the definition of electric dipole moment, **(b)** and **(c)** are the origin of electronic polarization [1]

Meanwhile, for a solid with the covalent bonds, the electronic polarization from an atom is quite small. The main polarization comes from valence electrons. Valence electrons live not only in covalent bonds between ionic cores, but also in the whole crystal because they may tunnel from bond to bond and exchange places mutually. Valence electrons' wave function is delocalized instead of localized to any particular atom. Thus, as shown in *Figure 1.4*, when an electric field is applied, electrons in covalent bonds are much more flexible than those individual ionic cores. This type of electronic polarization, aroused by the displacement of electrons in covalent bonds, is responsible for the large dielectric permittivity of covalent types' materials.
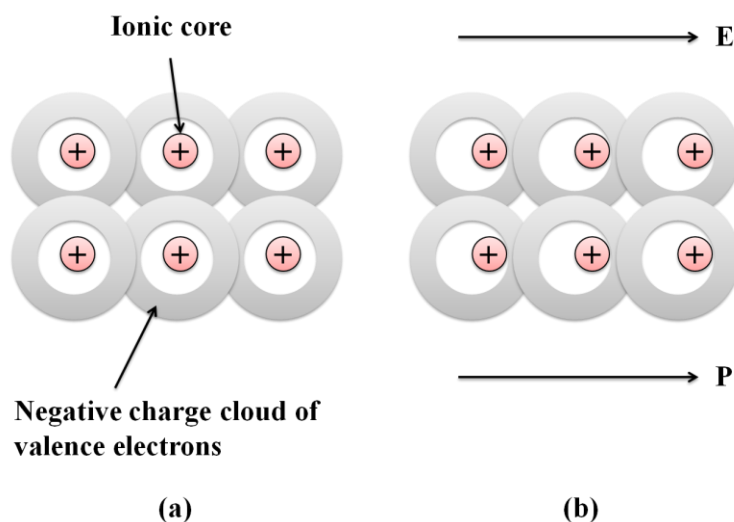
Figure 1.4 (a) Valence electrons in covalent bonds in the absence of an applied field. **(b)** When an electric field is applied to a covalent solid, valence electrons in covalent bonds shift very easily with respect to positive ionic cores. The whole solid becomes polarized due to the collective shift in the negative charge distribution of valence electrons. [1]

(2) Ionic polarization

　　Ionic polarization occurs in ionic crystals as shown in *Figure 1.5*. When an applied field is absent, the solid has no net polarization because dipole's moments of equal magnitude are lined up head to head and tail to tail so that net dipole's moment is zero. However, in the presence of a field *E* along the *x* direction, negative ions are pushed in the –*x* direction and positive ions in the +*x* direction about their equilibrium positions. Consequently, the dipole's moment p_+ in the +*x* direction increases to p'_+ while the dipole's moment p_- decreases to p'_-. At this time, the net dipole moment (average dipole moment) per ion pair is now p'_+-p'_- which depends on the electric field *E*. Additionally, each ion also has a core of electro that becomes displaced in the presence of an applied field with respect to the positive nuclei as we mentioned before. Hence, this part of dipole's moment caused by electrons also contributes to the polarization of a solid with the ionic polarization, although its magnitude is much smaller than ionic contribution in these solids.
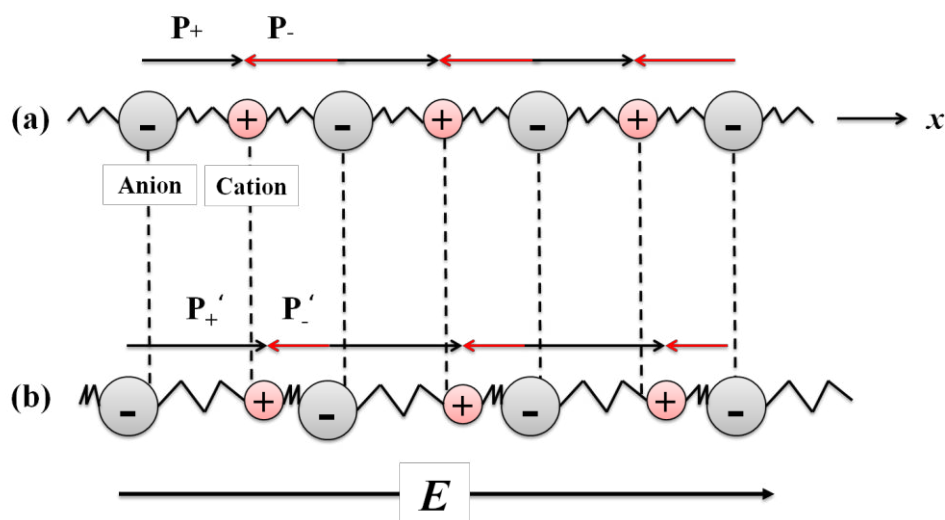
Figure 1.5 (a) Ion chain in the crystal without an applied field. Average or net dipole moment per ion is zero. **(b)** In the presence of an applied field, ions become slightly displaced, which leads to a net average dipole moment per ion. [1]

(3) Orientational polarization

This type polarization shown in *Figure 1.6* is typical for polar liquids and polar gases. It also happens in the solid if there are permanent dipoles within the structure. In general, molecules are randomly oriented as a result of thermal agitation when an electric field is absent. At once an electric field E is applied, dipoles will try to align parallel to the direction of E and consequently the material will exhibit net polarization. In order to align dipoles with E and lead to effective orientational polarization, the average dipole potential energy must be greater than average thermal energy. Hence, compared with the electronic and ionic polarization, orientational polarization is strongly temperature dependent and decreases as the temperature increasing.
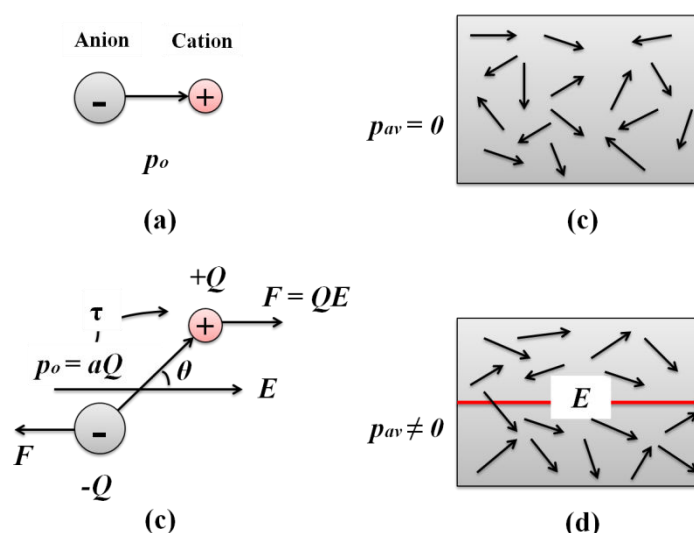
Figure 1.6 (a) A polar molecule possesses a permanent dipole moment p_0. **(b)** In absence of a field, thermal agitation of molecules results in zero net average dipole moment per molecule. **(c)** A dipole placed in a field experiences a torque that tries a rotate it to align p_0 with the field E. **(d)** In the presence of an applied field, dipoles try to rotate to align with the field against thermal agitation. There is now a net average dipole moment per molecule along the field. [1]

In the presence of electronic, ionic and orientational polarization mechanisms, the average induced dipole moment per molecule will be the sum of all contributions in terms of the local field. [1, 2] However, there is an essential polarization which is unavoidable for materials especially for composites: interfacial polarization. It cannot be simply added into the sum of the three polarization mechanisms since it occurs at interfaces where the field is not well defined.

(4) Interfacial polarization

Interfacial polarization appears because positive charges accumulate at the interface and remaining negative charges in the bulk together constitute dipoles moments that appear in the polarization vector. It occurs whenever there is an accumulation of charges at an interface between two regions especially for heterogeneous dielectric materials as shown in *Figure 1.7*. For a material, however perfect, it contains more or less defects, impurities and various mobile carries such as electrons, holes or ionized host or impurity ions. Under the presence of an applied

field, these positive ions migrate to the negative electrode and simply pile up at interfaces which raise positive space charge near the electrode. This additional charge on the interface appears as an increase in the dielectric permittivity.
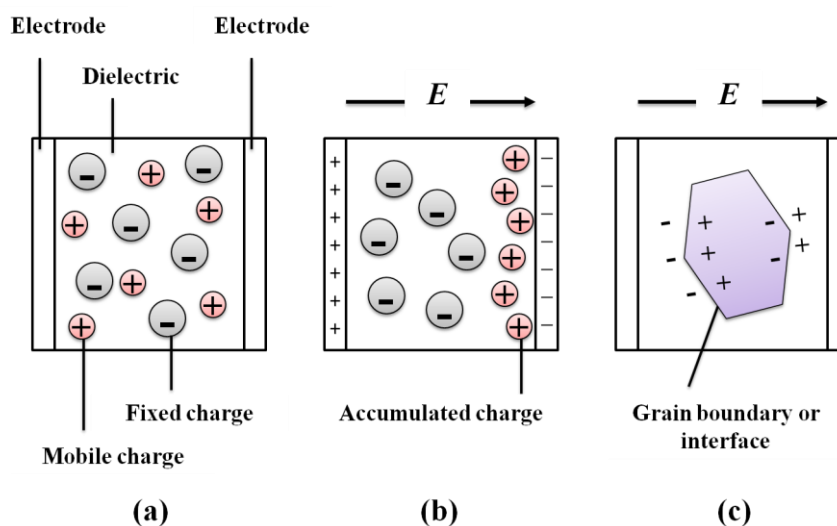
Figure 1.7 (a) A crystal with equal number of mobile positive ions and fixed negative ions. In the absence of a field, there is no net separation between all the positive charges and all the negative charges. **(b)** In the presence of an applied field, the mobile positive ions migrate toward the negative electrode and accumulate there. There is now an overall separation between the negative charges and positive charges in the dielectric. The dielectric therefore exhibits interfacial polarization. **(c)** Grain boundaries and interfaces between different materials frequently give rise to interfacial polarization. [1]

1.1.2 Frequency dependence

What we have already introduced is the static dielectric permittivity which is an effect of polarization under direct current (DC) conditions. While the voltage across a parallel plate capacitor is under a sinusoidal signal (alternating current (AC) field), then the polarization of the medium leads to an AC dielectric permittivity that is really different from the DC's case. Commonly, there are two factors against the immediate alignment of dipoles with the field. The first one is caused by thermal agitation which

randomizes the dipole orientations. The other one is attributed to interactions with neighbors in a viscous medium. This part will be particularly strong in the liquid or polymer where dipoles cannot response instantaneously to the applied field's change. Hence the dielectric permittivity of an insulating material depends on the frequency which can be described as a complex physical quantity:

$$\varepsilon_r = \varepsilon_r^{'} - i \cdot \varepsilon_r^{''}$$

where $\varepsilon_r{'}$ is the real part and $\varepsilon_r{''}$ is the imaginary part. $\varepsilon_r{'}$ represents the relative permittivity that can be used in calculating the capacitance. The imaginary part $\varepsilon_r{''}$ represents the energy lost in the dielectric medium as dipoles are oriented against random collision by the field. When the energy storage and transformation occur at the same rate, the energy will be transferred to heat most efficiently. The peak of $\varepsilon_r{''}$ is called a relaxation peak which is at the frequency when dipole's relaxations are the right rate for maximum power dissipation. This process is known as dielectric resonance.

We define the relative magnitude of $\varepsilon_r{''}$ with respect to $\varepsilon_r{'}$ through a quantity, *tanδ*, called the loss tangent (or loss factor), as

$$\tan \delta = \frac{\varepsilon_r^{''}}{\varepsilon_r^{'}}$$

The power dissipates per unit volume in the polarization mechanism is the energy loss per unit time to random molecular collisions as heat. Obviously, the dielectric loss is associated by three factors: frequency, electric field and *tanδ*.
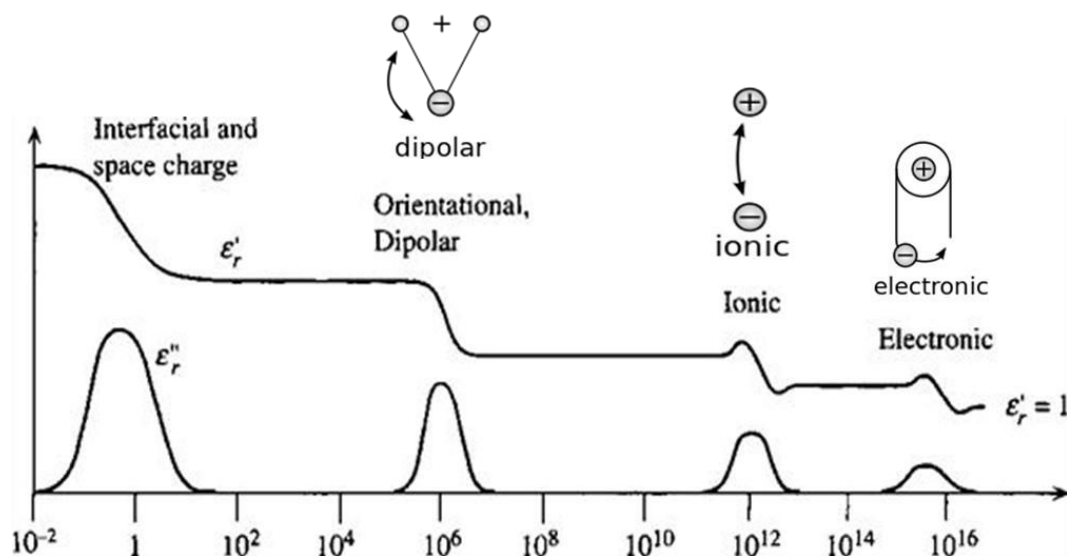
Figure 1.8 The frequency dependence of the real and imaginary parts of the dielectric permittivity in the presence of interfacial, orientational, ionic and electronic polarization mechanisms [1]

We can represent general features of the frequency dependence of the real and imaginary parts of the dielectric permittivity in *Figure 1.8*. Although the distinctive peaks in ε_r'' and transition features in ε_r' appear in certain frequency range, in real case these peaks and various features are broader with overlapping various peaks which exhibits a broad peak. Furthermore, at low frequencies, interfacial polarization's peak is even broader because there are numbers of mechanisms (various species of charge carriers) for the charges to accumulate at interfaces with individual speeds. Orientational polarization, although typically happens from radio to microwave frequencies, in some polymer materials, it involves a limited rotation of dipolar side groups attached to the polymer chain which can occur at lower frequencies depending on the temperature.

1.1.3 Dielectric materials

The property of a dielectric material can be described by several essential parameters depending on various application fields: polarization-electric field *P-E* relationship and breakdown field (dielectric strength, E_b) are for the high electric field

while the dielectric permittivity ε and dielectric loss *tanδ* are used for the weak electric field. [3-5] If we view the weak electric field application more concretely, for the application of integrated circuit insulation, a low dielectric permittivity is preferred. On the contrary, for the energy conversion and storage systems' application, a high dielectric permittivity is highly desirable. [4]

Due to the requirement for miniaturization in structure, it is trend of replacing discrete passives components by embedded ones. The schemes of discrete passives and embedded ones are shown in *Figure 1.9*, respectively. As one of essential components in embedded passives, materials for embedded capacitors are usually needed for high dielectric property. To meet the requirements of embedded capacitors, considerable research works have been devoted to develop materials with higher dielectric permittivity while low dielectric loss.
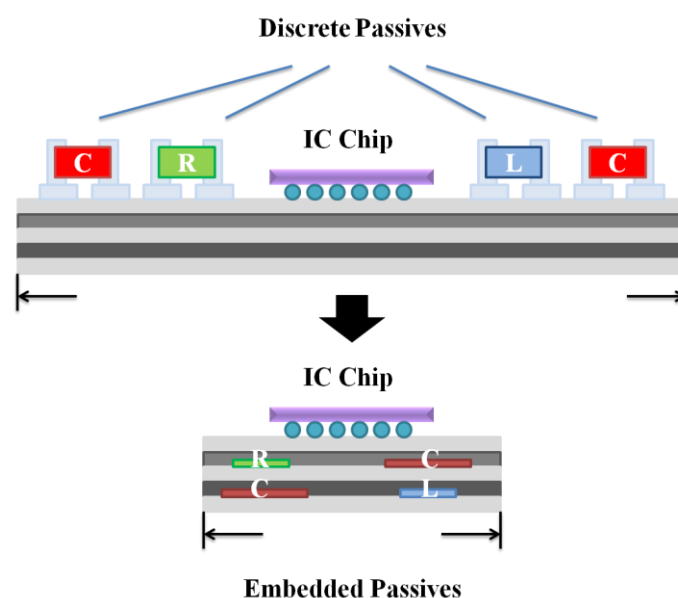
Figure 1.9 Schematic representation of size advantages of embedded passives as compared to discrete passives [6]

Conventional dielectric materials for capacitors are ceramics. In spite of high dielectric permittivity, ceramics usually need a high processing's temperature. Moreover, ceramic materials suffer brittle mechanical property and low dielectric strength which limit their widely application. Compared with ceramic materials,

advantages of common polymers are relatively high dielectric strength and mechanical flexibility. We list main index of common dielectric polymer films for recent capacitor's applications in *table 1*. However, due to instinct low dielectric permittivity, most polymers fail to meet the requirement for embedded capacitors which need materials with the dielectric permittivity in the range from 25 to 170. [7] Hence, the addition of inorganic fillers, especially nanoparticles, into polymer matrix to fabricate dielectric composites represents one of the most promising approaches for further improvement on dielectric property.

Table 1 Common polymer films for capacitors with their dielectric property [8]

Polymer film	ε_r	Maximum Temperature (^oC)	Breakdown strength (MW/m)	Energy Density (J/cm^3)	*Tanδ%* @1kHz
Polypropylene (PP)	2.2	105	640	1-1.2	<0.02
Polyester (PET)	3.3	125	570	1-1.5	<0.5
Polycarbonate (PC)	2.8	125	528	0.5-1	<0.15
Polyphenylene sulfide (PPS)	3	200	550	1-1.5	<0.03
Polyvinylidene fluoride (PVDF)	12	125	590	2.4	<1.8

According to the definition, nanoparticles are those particles with diameters below to micron dimension (<0.1μm). A more stringent definition considers nanoparticles as particles with properties depending on their sizes directly. In the latter case, restricted nanoparticles are those with sizes below 20nm. [7] Furthermore, the smaller the particles are, the more obvious surface properties will be which will strongly affect their interfacial properties, agglomeration and the physical property.

1.2 Composites for high dielectric permittivity

Based on the nanoparticles used, the polymer matrix composite can be classified into two types: one is the dielectric-dielectric composite where nanoparticles used are dielectrics; while the other is the conductor-dielectric composite where nanoparticles used are conductors. [4]

1.2.1 Simulations for dielectric-dielectric composites

Various formulas have been proposed to simulate the dielectric permittivity of dielectric-dielectric composite by analytical models. There are two well-known simplified models calculating the effective dielectric permittivity ε_{eff} for a composite: parallel and series models and they are shown in the *Figure 1.10 (a)* and *(b)*, respectively.
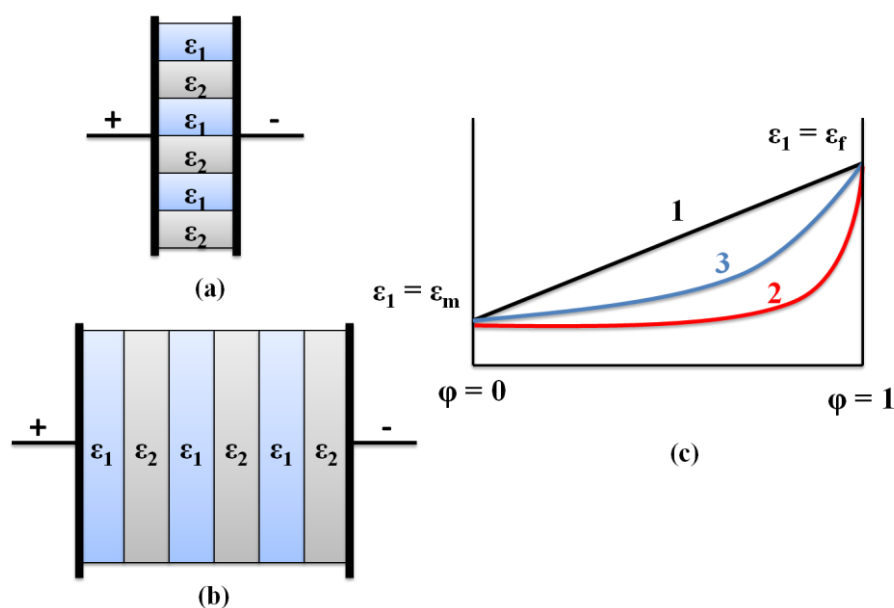
Figure 1.10 Schematic of structural patterns for parallel **(a)** and series **(b)** models. **(c)** Schematic of effective dielectric permittivity of a composite versus the composition: 1-parallel connection; 2-series connection; 3-real composite (Lictenecker's logarithmic mixing law) [4]

The formula can be simply written as:

$$\varepsilon_{eff}^{n} = (1 - \varphi)\varepsilon_{m}^{n} + \varphi\varepsilon_{f}^{n}$$

where φ is the volume fraction of fillers, ε_m and ε_f are the dielectric permittivities of matrix and fillers and n is either *+1* for parallel case or *-1* for series case. Compared with the experimental data obtained in *Figure 1.10 (c)*, we can find that ε_{eff} for the parallel model is always higher than that of series one while experimental one is usually between the two. [9]

$$((1 - \varphi)\varepsilon_{m}^{-1} + \varphi\varepsilon_{f}^{-1})^{-1} \leq \varepsilon_{eff} \leq (1 - \varphi)\varepsilon_{m} + \varphi\varepsilon_{f}$$

Besides series and parallel models, other models are provided as follows:

(1) Lichtenecker formula

As n approaching to 0, the equation can be equivalent to a logarithmic mixture rule which is known as the Lichtenecker formula (1926):

$$\log\varepsilon_{eff} = (1 - \varphi)\log\varepsilon_{m} + \varphi\log\varepsilon_{f}$$

Despite lacking enough scientific evidences, it has shown remarkable applicability to various heterogeneous media because it is a kind of compromise between the two extreme limits of series and parallel mixtures. [1, 10]

(2) Maxwell-Garnett formula

If the filler is spherical in shape, the composite can be treated as a dielectric sphere (filler) surrounded by a concentric spherical shell (matrix) as shown in *Figure 1.11*.
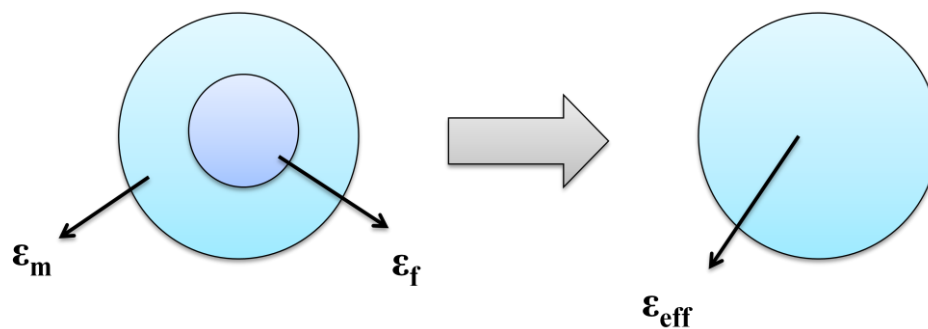
Figure 1.11 Schematic of Maxwell-Garnett formula[4]

The calculation for ε_{eff} can be written as

$$\frac{\varepsilon_{eff} - \varepsilon_m}{\varepsilon_{eff} + 2\varepsilon_m} = \varphi \cdot \frac{\varepsilon_f - \varepsilon_m}{\varepsilon_f + 2\varepsilon_m}$$

This is Maxwell-Garnett (also named as Maxwell-Wagner) mixing rule effective for calculating infinite dilution of dispersed phase (spherical particles are well separated by distances greater than their characteristic size). It is also argued that this mixing rule is an approximation of the Lichtenecker's logarithmic law. [12]

However, not all fillers are spherical shapes. When dispersed particles are not spherical in shape, it needs to be modified. A common way is to introduce a depolarization factor, which is related to their deviation from sphericity. Thus, Maxwell-Garnett is changed into a more general form:

$$\varepsilon_{eff} = \varepsilon_m \left[1 + \frac{\varepsilon_f(\varepsilon_f - \varepsilon_m)}{A(1 - \varphi)(\varepsilon_f - \varepsilon_m) + \varepsilon_m} \right] \text{ for } \varphi < 0.1$$

where *A* is the parameter of depolarization. When *A=1/3*, it is back to fillers with spherical shape. The value of *A* can be calculated or found in the reference. [12]

1.2.2 Simulations for conductor-dielectric composites

For conductor-dielectric composites, their properties are based on the percolation theory. In order to account for physical properties of heterogeneous materials, the percolation transition in properties is considered. This percolation transition lies in a fact that particles of minor phase (i.e. fillers) come into contact with each other and a continuous cluster extends throughout the system when the volume fraction of minor phase approaches the critical value f_c (percolation threshold). [13] In the case of dielectric property, as filler's content approaches to f_c, a dramatic change of composites' dielectric property will happen as indicated in *Figure 1.12*.
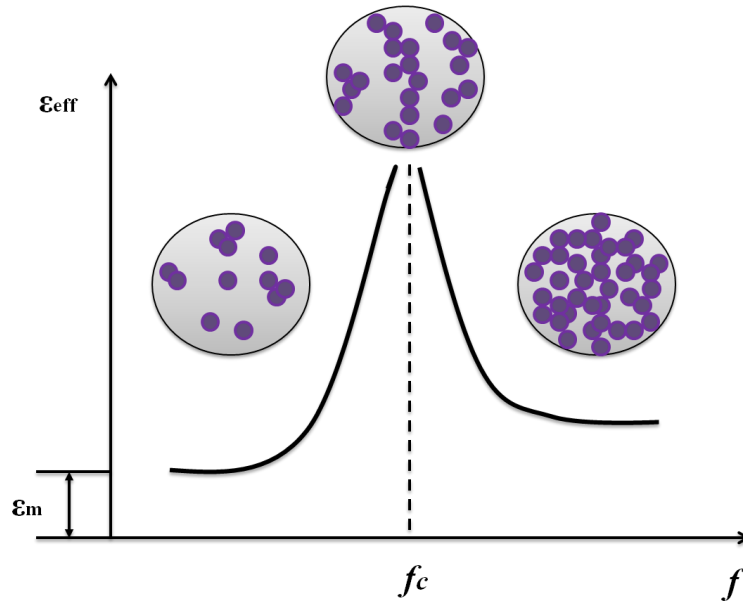
Figure 1.12 Schematic of ε_{eff} and volume fraction of fillers. The insets show the geometric phase transition of fillers (denoted by dark spots) in composite's microstructure near percolation threshold f_c. [4]

When f_c is approached from below, ε_{eff} diverges as follows:

$$\varepsilon_{eff} \propto \varepsilon_m |f - f_c|^{-q} \quad \text{for } f < f_c$$

where ε_m is the dielectric permittivity of the insulator matrix and q is a critical exponent which controls the variation of physical quantities near f_c. It varies from 0.8 to 1 in light of different interactions between matrix and fillers. [3] Moreover, q also depends on the spatial dimension of composites. As pointed out by Efros and Shklovski, [14] this formula infers the maximum value of dielectric permittivity achieved at f_c.

The dielectric behavior near f_c can be explained by micro-capacitor networks. [3, 13] Namely, each micro-capacitor is formed by neighboring conductive fillers and a very thin layer of dielectric in between. With a significant increase in the intensity of local electric field, each micro-capacitor contributes an abnormally large capacitance when fillers are close to f_c. This promotes the migration and accumulation of charge carries at the interfaces between fillers and matrix. The charges generated either by surface plasma resonance or by charge injection from the external electrodes are accumulated at the interfaces due to different relaxation times between fillers and

polymer matrix. This charges' accumulation may cause the Coulomb blockade by the insulating matrix until adjacent conductive fillers approach each other and the charges are tunneling (when the distance between the two neighboring particles is within tunneling range) or by Ohmic conduction (in the case of direct contact of neighboring particles).[13] This polarization caused by trapped or accumulated electric-charge carriers at interface is called interfacial polarization, also known as the Maxwell-Wagner effect. The interfacial polarization is responsible for the increment of dielectric permittivity especially at low frequency as it needs time for responding. If observed at high frequencies, the frequency response is the matrix dominant rather than the interface.

1.2.3 Interface between fillers and matrix

The interface sets up between two otherwise uniform phases A and B. Each atom or molecule in two-phase system equilibrates with its surrounding via short and long-range forces. Thus, the range which mutual forces are different from the 'bulk' is defined an interface AB as illustrated in *Figure 1.13 (a)*. As long as across interface AB, the intensity I of any property will change. Furthermore, the distances of property's change between A-B (t_1) and B-A (t_2) are usually different up to the property of interest.
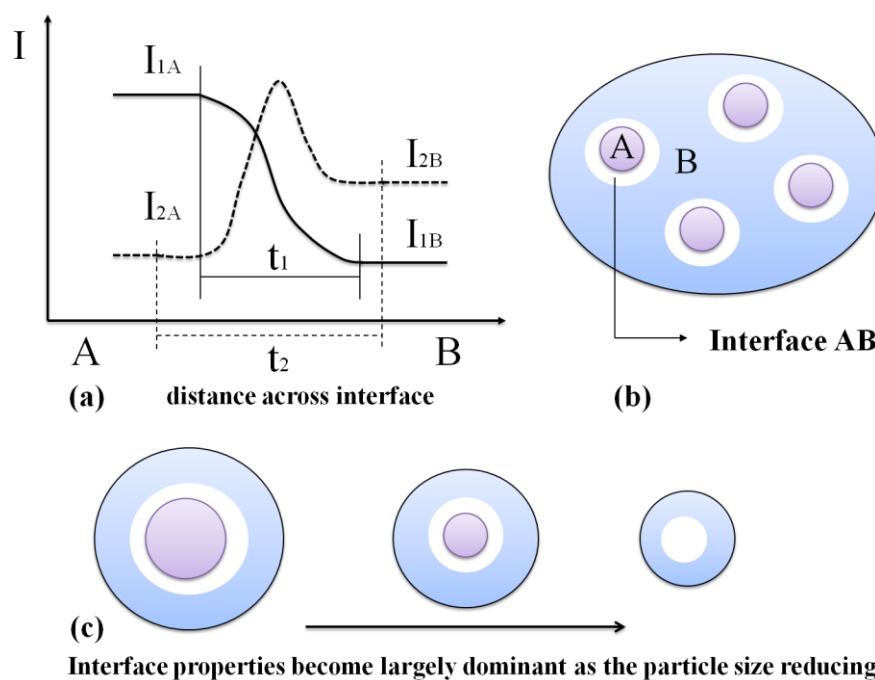
Figure 1.13 (a) The interface between two phases A and B defined by the intensities I_1 and I_2 of properties 1 and 2 as they vary over effective distances t_1 and t_2 between A and B. t_1 and t_2 will be of nanometric dimension. **(b)** Scheme of particle A with AB interface in the matrix B. **(c)** Particle size dependence of interface properties.[15]

Meanwhile, the interface also has another interesting phenomenon. Given a situation that A is the particle of finite size and surrounded by a polymer B with AB interface as shown in *Figure 1.13 (b)*, interface's effect will become increasingly significant as the particle's diameter reducing especially for nanoparticles. A following formula can describe the relationship among volume fraction of interface, thickness of shell and diameter of particle:

$$f = 3\frac{2t}{d}\left[1 - \left(\frac{2t}{d}\right) + \frac{1}{3}\left(\frac{2t}{d}\right)^2\right]$$

where *f* is the volume fraction of interface, *d* is the diameter of particle and *t* is the thickness of interface, respectively. [3, 15] According to this formula, the volume fraction of interface increases as the ratio of interface's thickness and particle's diameter increasing.

Additionally, the third important feature in nanometric system is also shown in

Figure 1.13 (c): a typical property of bulk *A* will be lost gradually as the particle's diameter shrinks and more elements of the particle come to reside in interface state which strengthens the influence of interface forces more than that of bulk forces. For the dielectric property of polymer matrix composite, as the diameter of particles reducing to the nanometric, the high dielectric property of nanoparticles usually acts as electrical defect centers in polymer matrix. Such a defect center effectively distorts the distribution of electric field and increases the local electrical field around the particles in the matrix where is much higher than the average field. Thus, the places with nanoparticles usually produce much leakage current and suffer low dielectric strength. However, given that nanoparticles are coated by a layer to barrier electron tunneling across the interface, the leakage current will be effectively controlled and the dielectric strength will be improved. Therefore, an ideal composite is supposed to comprise nanoparticles with grading dielectric permittivities from the center to the border by the bridge of interfaces.[13]

1.2.4 Gouy-Chapman diffusion layer and multi-layer core model

The morphology and property of interfaces have been widely investigated in many studies and generally they are affected by two parts. One is electrical interaction and the other is the surface characteristics of nanoparticles. On the one hand, in the case of electrical interaction, there is a model known as Gouy-Chapman diffusion layer shown in *Figure 1.14 (a)* which can illustrate the interfacial region between nanoparticles and polymer matrix. [15] If the nanoparticle is charged, an equalization of chemical potential will be established due to the ionization of surface groups and the adsorption of ions from the polymer matrix. According to colloid chemistry, a stern layer is usually formed attributed to the difference between inorganic nanoparticles and polymer matrix where a portion of counter ions is absorbed around nanoparticles by electrostatic Coulomb force and other forces. Two important interactions will be evoked in this layer. One is associated with the polarization from polymers involving dipole and molecular motion. The other is associated with a diffuse electrical double layer composed by positive and negative ions if the polymer

is solid electrolyte and contains mobile charges. According to Lewis et al's view, [15] the Debye length of the Gouy-Chapman diffusion layer can be calculated as several tens to one hundred nanometers. This indicates that nanoparticles are possibly to affect mutually and the electrically collaborative effect may be formed with the closest neighbors. Hence, as nanoparticle's volume fraction increasing, it can be anticipated that this interfacial overlapping phenomenon causes some collaborative effects which intensify interface's influence on the dielectric property.

On the other hand, in the case of interfaces' morphology and property, a comprehensive model has been proposed by Tanaka et al. [16, 17] This hypothetical multi-layered core model for the interface is based on a spherical inorganic particle embedded in a polymer matrix.
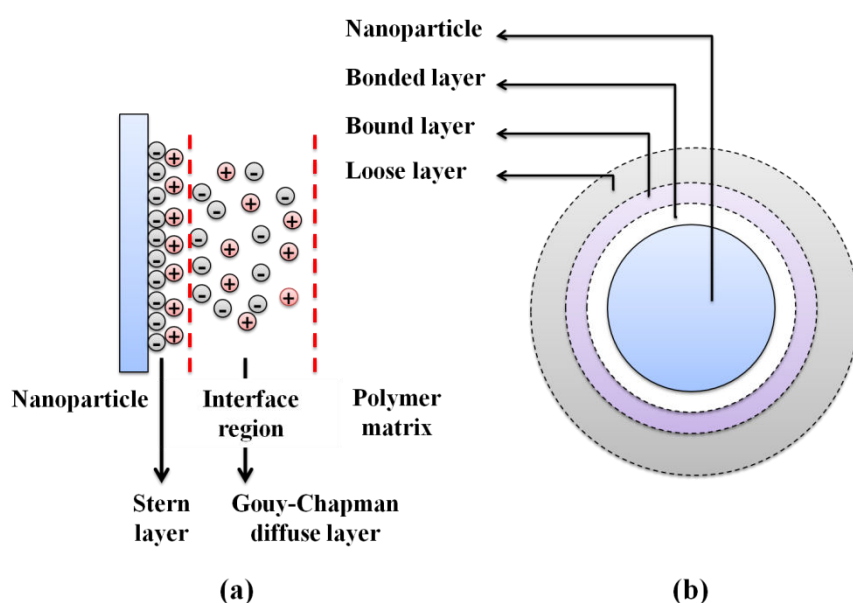
Figure 1.14 (a) The interface region of Gouy-Chapman formed in the positive charged nanoparticles. **(b)** Multi-layer core model for interfaces between inorganic nanoparticles and polymer matrix in a polymer nanocomposite. [3] It consists of a bonded layer, a bound layer and a loose layer. As the nanoparticle is positively charged, a diffuse electrical double layer would form in the interfacial region and overlap the three layers above.

As shown in *Figure 1.14 (b)*, the multi-layer core structure involves a bonded

layer, a bound layer and a loose layer gradually. The bonded layer is with the thickness around $1nm$ where the main interaction is consisted with short-range force such as ionic, covalent, hydrogen bonds, or van der waals force. Due to abundant unsaturated bonds like hydrogen and organic groups on the surfaces, nanoparticles are easy to be connected with polymer matrix. Thus, this layer is tightly bonded on both inorganic and organic substances and its strength largely depends on the polarity of particles and matrix. Usually the bigger the dielectric permittivity is, the stronger the force will be. Hence, bonded layer has an essential influence on the interfacial polarization.

The second layer is bound layer. It is consist of polymer chains which are bound or interacted to the bonded layer. It is associated with the polymer chains involving conformation, mobility, the degree of chain folding and stereographic structures. Its thickness is usually from 2 to $9nm$. Its morphology and strength are strongly influenced by the interfacial interaction strength of the bonded layer. It is postulated that tight binding such as ionic or covalent bonding will form a thick bound layer with a highly ordered structure. Besides the bonded layer's influence, the property of the bound layer also depends on surface property of nanoparticles and cohesive energy density of the polymer.

The third layer is loose layer which is a region loosely coupling to the bound layer. In this layer, polymer chains' conformation and mobility, and even free volume or crystallinity are all different from polymer matrix. But compared with inner two layers mentioned, the difference between the loose layer and polymer matrix is smaller. The thickness of this layer is about several tens of nanometers and they are randomly around the nanoparticle.

It is summarized that the binding strength in the bonded layer not only affects the thickness of interfacial region but also the local morphology and crystalline structure of the inner bound layer and even the loose layer. Therefore, the mutual effect of nanoparticles and polymer matrix in the interfacial region, especially in the bonded layer is crucial to the property of interface.

1.3 Nanoparticles used for composites

1.3.1 Nanoparticles for dielectric-dielectric composites

The key factor for improving dielectric permittivity in dielectric-dielectric composite is using nanoparticles with high dielectric permittivity. Researches in past few years have succeeded in promoting composites' dielectric performances by incorporating ferroelectric ceramic nanoparticles such as TiO_2, [18] ZrO_2, [19] $BaTiO_3$ (BT), [20-22] $CaCu_3Ti_4O_{12}$ [23] and $Pb(Zr,Ti)O_3$ [24]. Taking BT as an example, BT is a typical perovskite ceramic and its nanoparticles can be produced by micro-emulsion, sol-gel, and hydrothermal and so on. The high dielectric permittivity of BT results from its ferroelectric. This crystal is permanently polarized even in the absence of an applied field and it already possesses a finite polarization vector due to the separation of positive and negative charges. Moreover, BT's dielectric permittivity shows a clear size dependent which reduces dramatically from 5000 to hundreds as grain's size reducing from $1\mu m$ to $30nm$ due to crystalline phase's transition from tetragonal to cubic. But it does not mean that BT nanoparticles are inferior compared with microparticles. Dang et al. have studied BT's size dependency of dielectric permittivity for both BT/PVDF and BT/PI nanocomposites at low frequency. [20-22, 25] Although BT's ferroelectric property loses, the dielectric permittivity of composites with BT nanoparticles of smaller size is still much higher than that those of bigger size due to the strong interfacial polarization. Meanwhile, besides size's effect, temperature also influences greatly on BT's crystalline phase transition. A critical temperature of BT's crystalline phase transition from tetragonal to cubic phase, known as the Curie temperature, is around $437K$. Namely, BT exhibits neither permanent polarization nor ferroelectric above $437K$. On the contrary, it will come back to tetragonal phase with spontaneously polarized statement below $473K$. [26, 27] The effect of size and temperature on BT's crystalline phase's transition is shown in *Figure 1.15*.
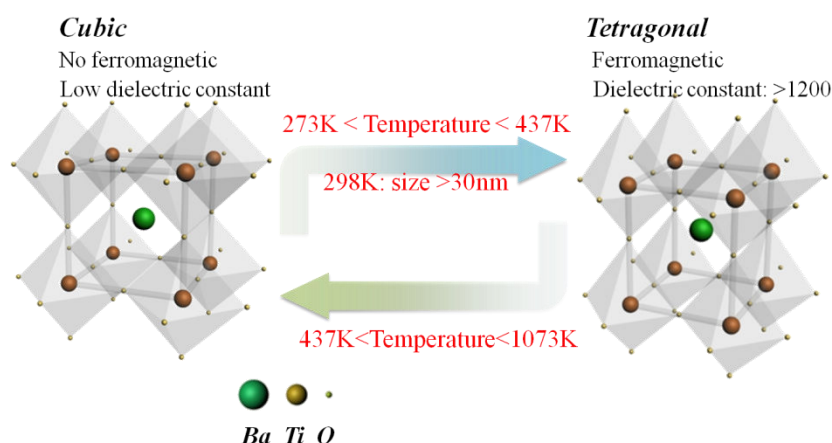
Figure 1.15 Size and temperature effects on two kinds crystal phases' mutual transition of BT particles

Lots of researches about BT reinforced polymer matrix composites have been reported in recent years. Kim et al. have studied the effect of various BT volume fractions on the dielectric permittivity and breakdown strength of poly(vinylidene fluoride-co-hexafluoro propylene) composites. The dielectric permittivity of composite achieves to 35 when BT's volume fraction is around 60%. Similar cases have also been found in BT/epoxy composites. [28] Kuo et al. have formed BT/epoxy with the dielectric permittivity of 50 which is almost ten times larger than epoxy's original dielectric permittivity. [29] Additionally, the effective surface modification of BT particles has also been proved to be effective for improving the dielectric property of composites. Zhou et al have reported that H_2O_2 modified BT can largely improve the dielectric strength of PVDF matrix composite due to the formation of hydrogen bond between electronphilic atoms on PVDF and –OH groups on the surface of BT. [30] Huang and Jiang have successful prepared core-shell structured BT/poly(methyl methacrylate) (PMMA) nanocomposite via in situ atom transfer radical polymerization (ATRP) of methyl methacrylate (MMA). The core-shell structure achieves its composite to extremely low dielectric loss. [31]

However, as mentioned before, dielectric properties of BT reinforced polymer matrix composites are temperature dependent which limits their further applications. [4] Moreover, in order to achieve higher dielectric permittivity, large amounts of BT

(more than 50%) is usually needed for the composite which reduces the mechanical flexibility of composites and makes them extremely brittle.[28] Hence, more works and studies in dielectric-dielectric composites are still needed for achieving high dielectric property of composites.

1.3.2 Nanoparticles for conductor-dielectric composites

Compared with the dielectric-dielectric composite, the addition of conductive nanoparticles has a stronger impact on composite's dielectric property. By replacing dielectric nanoparticles with conductive ones, percolative behavior will increase the dielectric permittivity dramatically (several tens times higher than the polymer matrix) in the vicinity of percolation threshold. Thus, it provides a potential alternative in virtual of extremely high dielectric permittivity with much lower fillers incorporating, as long as that they can also meet the requirement of the dielectric breakdown strength and low loss tangent. [3]

Among various conductive fillers, carbon nanotube (CNT) doubtlessly has attracted the most attention. CNT has a hollow structure with the walls formed by one-atom-thick sheets of carbon called graphene which are rolled at specific and discrete ("chiral") angles. CNT generally is categorized as single-walled nanotubes (SWNT) and multi-walled nanotubes (MWNT). [32] SWNT has a single seamless cylindrical wall with fullerene caps while MWNT has several graphite sheets which are concentrically rolled up around each other. Due to the unique structure, CNT has many advantages over other conductive fillers which can be included at least three points as follows:

1. The superior intrinsic conductivity ($10^5 \sim 10^8 S/m$) and excellent electric current carrying capacity which is 1000 times higher than copper wire.

2. The high compatibility with the polymer matrix which does not deteriorate the flexibility of polymer matrices.

3. A large and tunable aspect ratios which significantly reduces f_c in its composite. [13, 33]

1.4 Carbon nanotube and its polymer matrix composites

1.4.1 Synthesis of CNT by chemical vapor deposition

Chemical vapor deposition (CVD) is one of the most popular methods used to produce CNTs. In this process, thermal decomposition of a hydrocarbon vapor is conducted in the presence of metallic catalyst. Differently with high temperature electric arc discharge technique, a medium temperature range can meet for the synthesis which makes CVD popular for CNT's synthesis. The temperature used for CVD is usually less than $1000^{o}C$ and hydrocarbon compounds are decomposed on the substrate by inducing catalysts. The common procedures can be divided into the following four steps and the experimental set-up CVD used for CNT growth in its simplest form is shown in *Figure 1.16*. [34, 35]

1. Metallic nanoparticles are required to be well prepared on a substrate.

2. A substrate is placed in the furnace and a reduction treatment is carried out for nanoparticles upon heating under carries gases of Ar, H_2 or NH_3.

3. The hydrocarbon gas or the liquid carbon resources selected are introduced into the furnace.

4. CVD growth occurs at a suitable temperature by catalytic decomposition of the hydrocarbon molecules on the metallic nanoparticles.
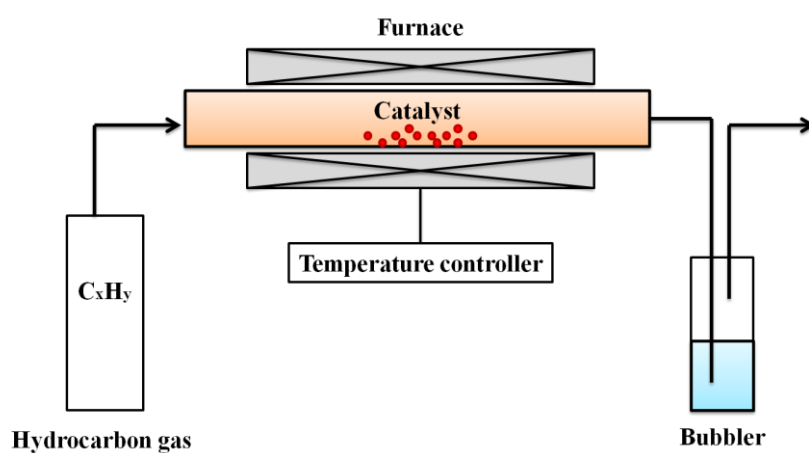

Figure 1.16   Schematic diagram of a CVD setup in its simplest form [34]

The transition metals such as iron, cobalt and nickel are suitable catalysts for the growth of CNT. Their advantages can be summarized as follows: (1) high solubility of carbon at high temperatures, (2) high carbon diffusion rate and (3) a wide CVD's temperature window for more choices of carbon sources due to high melting point and low equilibrium-vapor pressure of these metals. However, a bulk metal itself is not able to catalyze the decomposition of hydrocarbon vapor to form carbon filaments. Instead, it has to be dispersed into nanoparticle's forms before CVD which is indispensable for the CNT growth. According to the literatures there are several ways to prepare catalyst nanoparticles such as sol-gel, [36, 37] impregnation, [38, 39] and thermal deposition of solid organometallocenes (for example, ferrocene, cobaltocene and nickelocene) [34, 40, 41].

Meanwhile, the growth of CNT greatly depends on the nature of substrate despite the same catalyst used. In order to achieve an efficient CNT growth, substrates should be chemically inert to metallic particles because metal-substrate reactions (chemical bond formation) will block the catalyst activity. Furthermore, the surface morphology and textural properties of the substrate will also greatly affect both yield and quality of CNTs. According to relative researches, nanopores on the surface of substrate will not only increase the yield of CNT but also provide the narrow distribution of CNT's diameter. Additionally, substrate's thickness and shape are also important for CNT's growth. Commonly, the substrate for hybrids in our group involves alumina (Al_2O_3), [42, 43] graphene nano-sheet (GNP), [44, 45] and silicon carbide (SiC) [46, 47] etc.

Hydrocarbons are easy to break at high temperature and this thermal decomposition is called "pyrolysis". The growth of CNT will be achieved only when the pyrolysis occurs in the presence of catalyst nanoparticle. The mechanism of CNT's growth has been debatable for a long term and there are two general models which are widely accepted: tip-growth model and base-growth model [48, 49], respectively. The mechanism for practical growth cases usually depends on the interaction between catalyst and substrate.

In the case of tip-growth model which is illustrated in *Figure 1.17*, when the

catalyst-substrate interaction is weak (the metallic particle has an acute contact angle with the substrate), the hydrocarbon will decompose on the top surface of the metallic particles while the carbon will diffuse down through metallic particle's bottom which will push the whole metallic particle off the substrate. As long as the metallic particle's top is open for fresh hydrocarbon decomposition (a concentration gradient exists in the metallic particle which results in the carbon diffusion), CNT continues to grow longer and longer. Once the metallic particle is fully covered with excess carbon, its catalyst activity stops and CNT's growth is ceased.
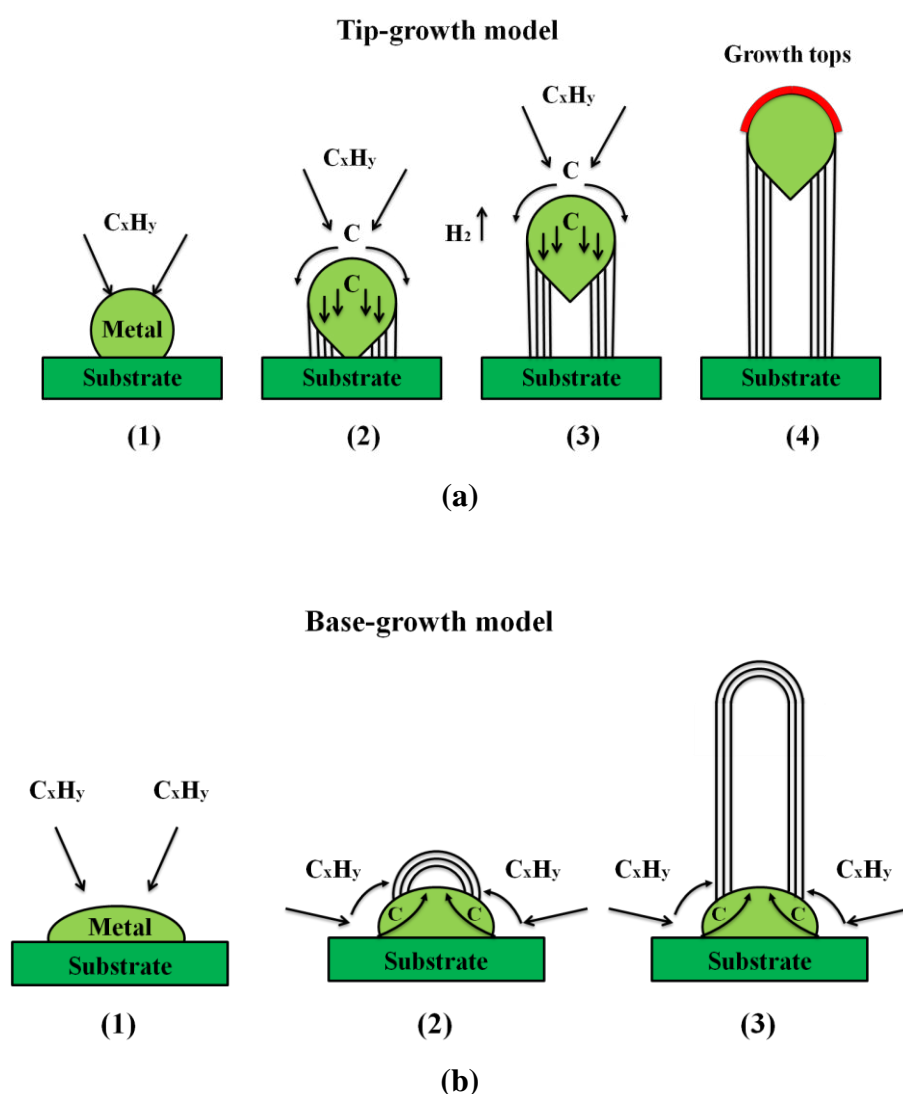

Figure 1.17 (a) for tip-growth model and **(b)** for base-growth model [34]

In the case of base-growth model which is shown in Figure *1.17 (b)*, it is for the

strong interaction between metallic particle and substrate where an obtuse contact angle is formed between the two. The initial hydrocarbon decomposition and carbon diffusion occur which is as similar as the case of tip-growth model, but differently, CNT does not push the catalyst up from the substrate. The growth is compelled to emerge out from the top of metallic particle (farthest from the substrate that has minimum interaction with the substrate). At the beginning, carbon crystallizes out as a hemispherical dome (the most favorable closed-carbon network on a spherical nanoparticle) and then extends up in the form of seamless graphitic cylinder. Subsequent the hydrocarbon deposition happens on the lower peripheral surface of metallic particle and then as-dissolved carbon diffuses upwards. Thus CNT grows up with the metallic particle rooted on its bases.

Additionally, besides the interaction between catalyst and substrate, CNT's growth is also governed by the size of catalyst particle. Generally speaking, smaller particles (a few nanometers) favor SWNT's formation while bigger particles (tens nanometers) favor MWNT's formation. Furthermore, higher temperature ($900-1200^oC$) yields SWNT which needs higher energy while lower temperature ($600-900^oC$) favors MWNT's growth. [34]

1.4.2 Improving the dispersibility of carbon nanotubes in composites

Due to the substantial van de waals attraction, a homogeneous dispersion of CNT is really hard to realize which usually causes composites' properties far away from the expectation. Thus, a good dispersion of CNT in the polymer matrix is essential for achieving high property. Moreover, the interface between CNT and polymer should also be well and carefully designed. Otherwise, interfacial slippage by poor adhesion and less interaction may happen which influences the property negatively.

In order to improve the dispersibility of CNT, lots of efforts have been invested which can be roughly divided into four strategies: (1) Surface modification of CNT; (2) Functionalization of polymer matrix; (3) Adding compatibilizers and (4) Preparing polymer composites via suitable process ways. We will introduce recent studies on the surface modification of CNT and the processing ways for composites in this part.

There are two main approaches for CNT's functionalization: the covalent functionalization and the non-covalent one. For the part of covalent functionalization, it is achieved by either direct addition reactions to CNT's sidewalls or modifications of some surface bound functional groups such as carboxylic acid on the CNT. The functionalized CNT can be much more stable in polar solvents. Furthermore, they can reinforce the strength of interfacial bonding between CNT and polymer matrix by functional groups. However, functionalization will damage sp^2 conformation of carbon atoms and influence electrical and mechanical properties negatively. Some brief functionalized ways of CNT are shown in *Figure 1.18*.
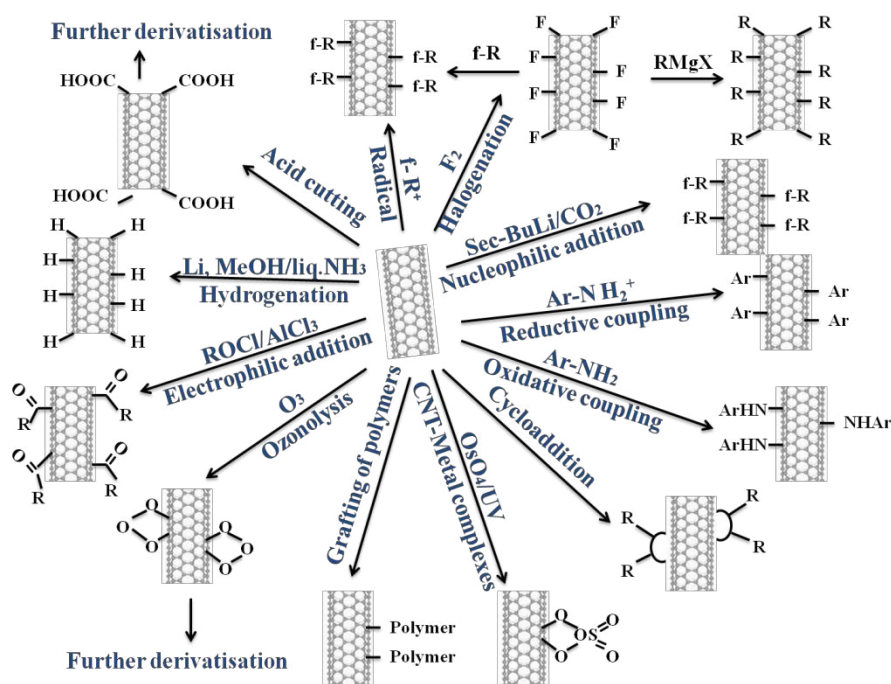
Figure 1.18 Surface functionalization of CNT [50]

For the part of CNT's non-covalent functionalization, it depends on van der waals force, π-π, CH-π and electrostatic interactions. The advantage of non-covalent functionalization is remaining the original structure of CNT as well as its excellent electrical and mechanical properties. But the interaction between CNT and wrapping molecules is much weaker than the covalent one. Generally, polymers with conjugated and aromatic groups are widely used for polymer wrapping though π-π

stacking and van der waals interactions (e.g. polyvinyl pyrrolidone (PVP) [51], poly(phenylenevinylene), pyrene-poly(ethylene glycol)). However, the efficiency of load transfer might decrease since forces between wrapping molecules and CNT surface might be relative weak. [33]

For a semicrystalline polymer matrix, interfacial crystallization offers another possible method to enhance CNT/polymer interfacial interaction. This interaction between polymer and CNT is attributed to the crystallization at the interface where CNT acts as nuclei that induces the polymer lamellae growing on its surfaces. These as-formed crystalline structures are generally denoted as hybrid crystalline structure, in contrast to conventional crystalline structures consisting of only polymer species.

Generally, there are two factors resulting in the interfacial crystallization: (1). Electrostatic and van der waals's interactions. (2) Mismatch in the coefficient of thermal expansion (CTE) between CNT and polymer. [52] For the former one, an interfacial crystalline layer yielded on the graphite surface of CNT can enhance the electrostatic matching between graphite crystallites and segments in a special crystalline-chain conformation. For example, the interfacial crystalline layer of PVDF coating on CNT is β polymorph with the zigzag all-trans conformation.

For the difference in CTE, polymer crystalline polymorph's CTE is smaller than its amorphous counterpart, the mismatch in CTEs between CNT and polymer may be increased with the appearance of crystalline interface layer. This may lead to higher compressive thermal residual stress and a stronger mechanical interlocking effect, compared with the case of amorphous polymer on the CNT surface. Hence, it probably causes the property change after thermal treatment.

1.4.3 Processing for CNT/polymer matrix composites

All the processing routes normally aim at dispersing CNT in the polymers matrices with a desired manner. Common traditional approaches for fabricating CNT reinforced polymer composites include: solution casting, melt processing, in situ polymerization, processing of composites based on thermosets, and electro /coagulation spinning for composite fibers or yarn production. [5, 53, 54] These methods

have been well discussed and included in recent reviews. *Figure 1.19* provides a scheme of the general processing procedures for CNT/polymer matrices composites. In the following paragraphs, we introduce some common routes as well as novel approaches for CNT reinforced polymer composites.
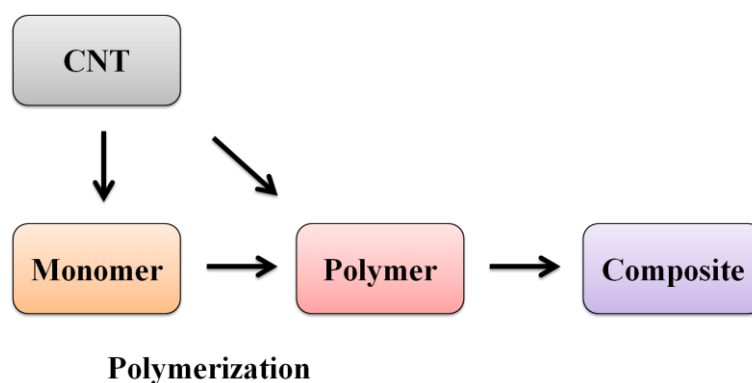
Figure 1.19 Processing routes for CNT reinforced polymer matrix composites

(1) Solution casting

In this route, a dispersion of CNT and polymer matrix in a suitable solvent is required in the first step. And then the composite film is formed by precipitating or evaporating the solvent. The solvent can be either polar or non polar in light of the polymer's chemical property. An advantage of this route is the possibility to achieve debundling and good dispersion of CNT in composite. Many polymers can be solved in common solvents such as toluene, chloroform, tetrahydrofurance (THF), dimethylacetamide (DMAc) or dimethylformamide (DMF). [55-57] For example, DMF is a good solvent for efficiently dissolving PVDF and disposing CNT. [21, 58] Ultrasonic wave is the most efficient tool to release the aggregation of CNT because it reinforces the interaction between CNT and polymer which may cause the crystalline transformation of PVDF. [59] Yu et al. have reported that both α and β polymorphs of PVDF are found in ultrasonicated MWNT/PVDF mixtures while only α polymorph of PVDF is existed in the mixture without ultrasonicated processing.[60] However, there is an unavoidable requirement is that polymer matrix must be soluble in certain solvent. This is one of limitations for its widely application in industry. Furthermore,

it is less environmental friendly and economical due to the consuming of the solvents.

(2) Melt processing

Compared with the solution casting, melt processing is a more common and simpler route from the perspective of commercial applications, particularly for thermoplastic polymers which are stable under their process temperature, e.g. polypropylene/CNT, [61] high density PE/CNT, [62] polycarbonate/CNT, [63] PMMA/CNT, [64] polyoxymethylene/CNT, [65] polyamide 6 (PA6)/CNT, [66] etc. Melt processing usually mixes CNT with the molten polymer by shear of screws and afterward shaping by compression molding, extrusion or injection molding. Advantages of this route are its high speed, simplicity and easy integration into standard industrial facilities. But the disadvantage is still on the dispersion of CNT in polymer. A high increment of viscosity is observed even at low amount of CNT due to a high interfacial surface energy between entanglement of CNT and polymer chains. Consequently, the bubbles introduced during the process are extremely hard to remove which is even worse in the case of CNT with long aspect ratio. These defects in the composites usually lead to a poor quality. Thus, some additives are introduced (e.g. processing acids and plasticizers) into system or much stronger mechanical shearing has to be applied which may destroy the structure of CNT. [53, 54] Another disadvantage of the melt processing is the migration and orientation of CNT under flow especially during injection molding procedure. [67, 68] T. Villmow et al have studied CNT reinforced PC composites by extrusion-injection route. The morphology of the sample in different thickness has been carefully observed by transmission electron microscopy. [69] They have found that the more closes to the core part, the more random of CNT's dispersion will be in the composite.

(3) In-situ polymerization

CNT are disposed in the monomer followed by polymerization via this route. A higher percentage of CNT may be facially dispersed by a strong mechanical stirring during the reaction. It is suitable for preparing a composite whose polymer matrix fails to be processed by neither the solution casting (insoluble ones) nor the melt processing (thermally unstable polymers or those with low melt flow index). [23, 70-71]

Cochet et al have reported the improved electrical properties of MWNT/polyaniline (PANI) composite by in situ polymerization due to the site-selective interaction between the quinoid ring of PANI and MWNT. [73] Cho and co-workers have reported a simple approach to synthesizing MWNT/polypyrrole composite with high conductivity by in situ polymerization of pyrrole on CNT with the addition of ferric chloride as an oxidant. [74]

(4) Layer-by-layer (LBL) technique

The LBL route involves fabricating a layered structural composite by alternate dipping of a substrate into CNT/polyelectrolyte dispersions. [75-77] Meanwhile, in order to enhance the film's structural integrity, the crosslink is usually introduced to reinforce the adhesions of films. As a versatile and relatively low-costly route, it provides multifunctional molecular assemblies of tailed structures so that various properties of the composite will be achieved in order to meet different requirements of materials with nanometer thickness. Moreover, large-scale and reproducible production of membrane-based, highly integrated microsensors will also be achieved due to the simple processing of LBL. [78]

(5) Buckypaper

Buckypaper is a thin porous assembly of CNT and in the last few years, its electrical mechanical properties have attracted much attention. The common preparation of buckypaper usually requires CNT being well-dispersed in a certain solvent such as DMF or N-Methyl-2-pyrrolidone and then removing the solvent by Buchner filtration. [79, 80] Recently, a novel preparation without the dispersion and filtration process has been formed by Ding and his co-workers. [81] CNT arrays have been used, rather than the mixture of CNT and solvent, for achieving the "domino pushing effect" so that most of CNT are well aligned tightly in the buckypaper. Thus, better properties have been achieved in thermal or electrical conductivity due to the regularity in structure.

In summary, with these different processing techniques, numbers of polymers can be processed to CNT reinforced composites no matter thermoplastic or thermoset, and amorphous or semi-crystalline. An optimized process is the priori of good CNT's

dispersion in the polymers matrices. Meanwhile, a careful investigation on the state of CNT's aggregation and the orientation in the composite is also necessary and crucial for the final property.

1.5 Property of polyvinylidene fluoride

PVDF is synthesized by addition polymerization of $CH_2=CF_2$ monomers. The polymer chains are composed by an alternating CH_2 and CF_2 groups as shown in *Figure 1.20 (a)*. [82] Due to highly regular chain structure, PVDF is semi-crystalline polymer with the typical crystallinity of 50%. Meanwhile, its glass transition temperature (Tg) and melting point are around -40°C and 170°C, respectively. As a thermoplastic polymer, a reasonable melting viscosity lets PVDF have good processing ability without adding stabilizers. [83, 84] The pressure-volume-temperature (PVT) curve of PVDF is also provided in *Figure 1.20 (b)*, the volume expansion of PVDF occurs at the melting point since crystalline part gradually changes into amorphous part at this stage.

A high dielectric property makes PVDF distinguished from other polymers in the application of dielectric materials. [86] PVDF's high dielectric property is attributed to its piezoelectricity and the polarization. As a semi-crystalline polymer, PVDF has at least five crystalline polymorphs. [87-90] However, not all crystalline polymorphs have high piezoelectric property because piezoelectricity depends on polar crystal structure. Although piezoelectricity of PVDF is still low compared to piezoelectric ceramic materials such as BT and lead zirconate titanate, easy processing makes PVDF becomes very popular for piezoelectric materials. [91]
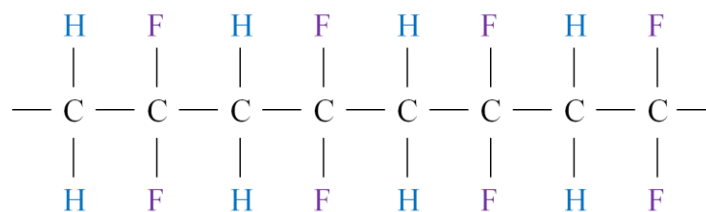
(a)
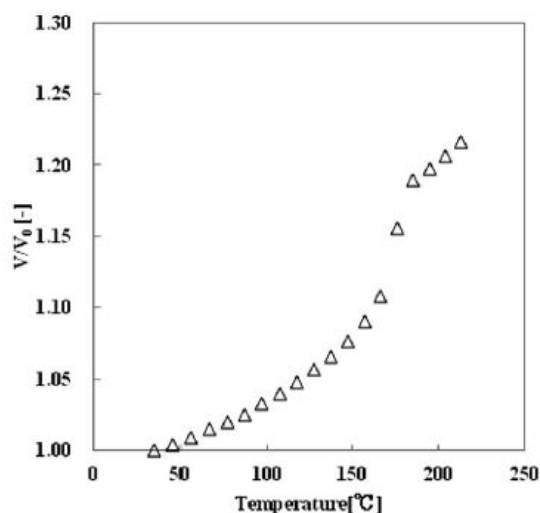
(b)

Figure 1.20 Scheme of PVDF chains **(a)** [81] and its PVT curves **(b)** [85]

1.5.1 Crystalline polymorphs of polyvinylidene fluoride

Concretely, five distinct crystalline polymorphs of PVDF are α, β, γ, δ and ε, respectively which can be characterized by X-ray diffraction (XRD) and fourier transform infrared spectrometer (FTIR). The most common crystalline polymorph is α crystallized from melt or solution. [88, 92-94] It consists of chains with trans-gauche-trans-gauche' (TGTG') torsion conformations arranging in an anti-parallel form. In TGTG' conformation, dipoles are inclined relative to the normal axis so that the average dipole moment for each monomer is largely reduced. Meanwhile, the unit cell of α phase lattice has two chains in a TGTG' conformation and dipoles normal to the chain axis are anti-parallel, thus neutralizing each other. Thus, this conformation results in non-polarity which causes limited piezoelectricity and low dielectric property.

The second crystalline polymorph is β whose polymer chains have an all-trans

distribution (TTTT) in a distorted, planar zigzag conformation. This all-trans conformation has all of its dipoles aligned to the chain axis. Its unit cell has two all-trans chains packed with their dipoles pointing in the same direction. [88, 91, 93, 94] Molecular dipoles in the β polymorph are thus entirely aligned in one direction which have spontaneous polarization and substantial piezoelectricity. The structures of α and β polymorphs are shown in *Figure 1.21 (a), (b)*, respectively

α polymorph: trans-gauche molecules stack with a centre of symmetry, and form a non-polar unit cell

F   C   H

(a)

β polymorph: all trans molecules stack without the centre of symmetry, and so form a polar, piezoelectric unit cell
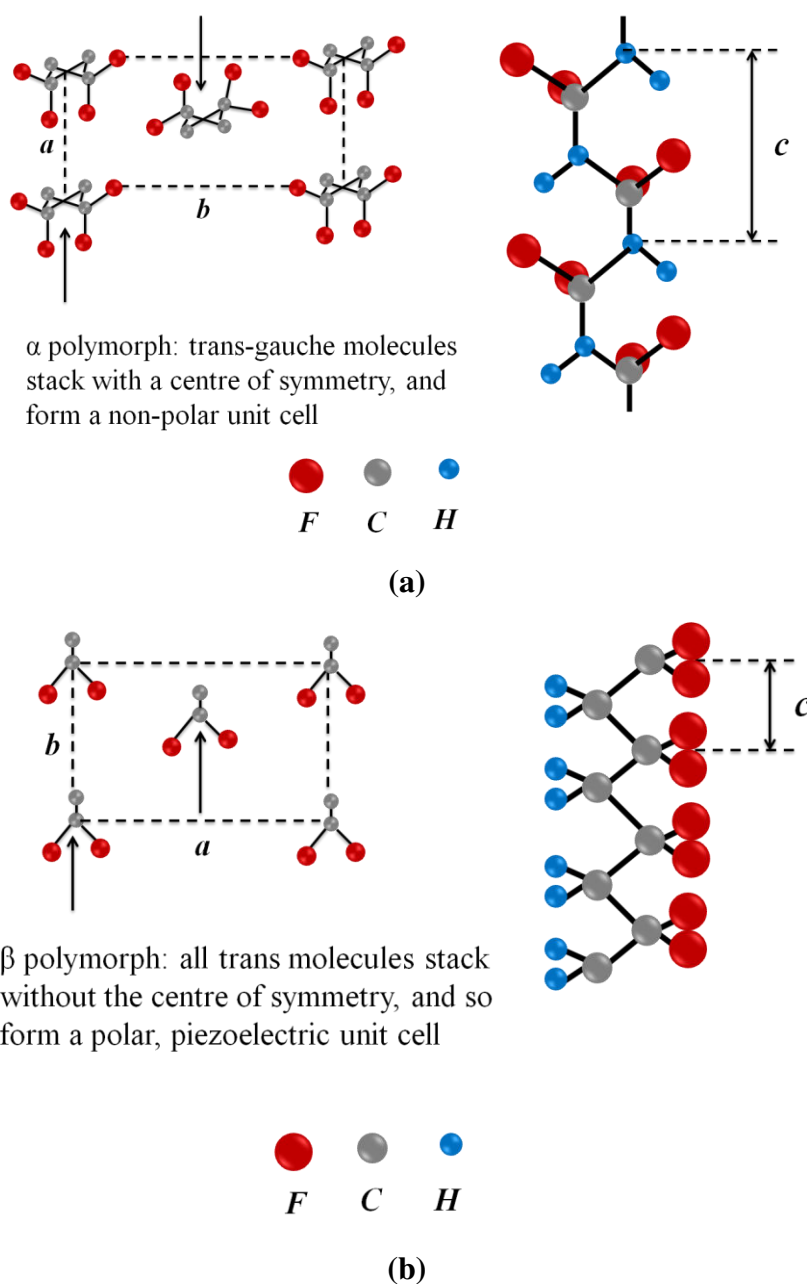
F   C   H

(b)

Figure 1.21 The structural schemes of PVDF's crystal phases: **(a)** for α and **(b)** for β phases, respectively [92]

Table 2 provides the crystalline parameters of α and β polymorphs.

Table 2 Parameters for two crystalline polymorphs of PVDF [95]

Crystalline polymorph	a (Å)	b (Å)	c (Å)
α	4.96	9.64	4.62
β	8.58	4.91	2.56

γ polymorph has chains with T3GT3G' torsion distributions and its conformation of chains are similar with α polymorph. δ and ε polymorphs are the polar and anti-polar of α and γ polymorphs, respectively. For δ polymorph, chains are arranged in a parallel fashion which is also able to yield a polar structure, but due to smaller dipole moment of each chain, δ polymorph is less polar than β phase. [88, 91]

1.5.2 Inducing β crystalline polymorph

Due to its high dielectric property, researches of inducing β polymorph in PVDF and its composites have been very attractive. However, it is not easy to obtain the entirely β polymorph PVDF by common processing ways. In all-trans PVDF, neighboring fluorine (F) atoms has to overlap because the diameter of F atom ($0.27nm$) is slightly larger than the space provided by all-trans carbon chain ($0.256nm$). This process needs more energy to achieve, but in order to diminish the overlapping CF_2 groups are tilted to the right and left to their original conformation. This deflection of CF_2 groups converts from TTTT (β polymorph) conformation into TGTG' (α polymorph) or TTTG' (γ polymorph). [91] Hence, it is much easier to obtain α polymorph than β polymorph in normal circumstances. Nevertheless, there are still some methods to induce β polymorph which can be divided into four points: (1) drawing-poling of PVDF films and fibers [93, 96-99] (2) optimization processing conditions [96, 100, 101] (3) copolymerization with trifluoroethylene [102-107] and (4) addition of CNT. [60, 108-110]

(1) Drawing-poling

Drawing generally orientates molecular chains (even for some crystallites)

towards the drawing direction which will promote the transition from α to β polymorph especially during the crystallization process. It can be explained from the structural difference between the two polymorphs. As the parameters shown in the *table 2*, the unit cell of β polymorph is longer in the chain direction while shorter in other two directions than α polymorph. Thus, drawing in the chain direction may provide the possibility for the transition from α to β polymorph. However, drawing's temperature is a key factor. Sajkiewicz et al. have showed that PVDF film or fiber must be drawn at temperature below the range from 130 to 140^oC so that the transition from α to β polymorph could be induced. Afterwards, the maximum of transition may happen from 70 to 87^oC. [111] If the temperature is too low, the viscosity of PVDF is too high for chains' mobility under the stress. Reversely, if the temperature is too high, the low viscosity may decrease the strength of crystalline which causes a deformation under stress. [91]

However, obtained all-trans conformation by merely drawing still cannot achieve high dielectric property since simply drawing just yields the orientation of crystallites. Dipoles are still in an irregular alignment in these β crystalline grains and thus permanent dipoles' polarization is absent. The experimental works by Nilsson et al. [112] and molecular dynamics (MD) simulation by Satyanarayana and Bolton [113] have proved that merely drawing cannot achieve the piezoelectricity. A strong external electric field (at least 80M*V/m*) is necessary for the alignment of dipoles and this process is called poling. Poling is divided into two kinds: contact poling and non-contact poling. Both of them are shown in *Figure 1.22*. In the case of contact poling, electrodes are required for contacting PVDF film or fiber directly. While in the case of non-contact poling, poling can be realized by a corona discharge which provides a higher electric field before PVDF's electrical breakdown occurs.
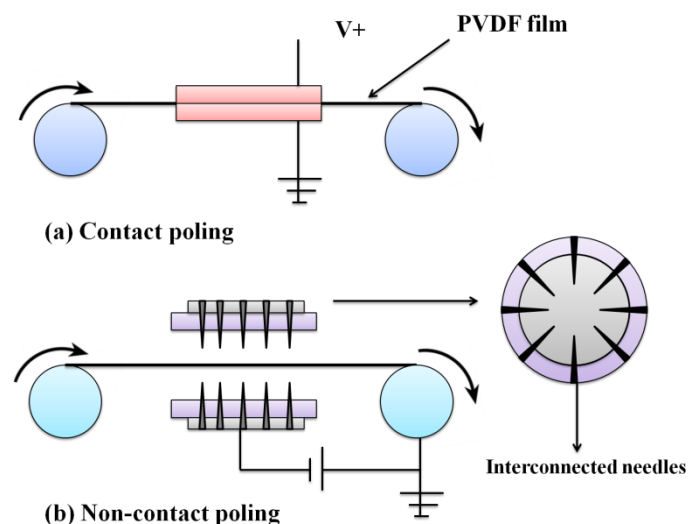
Figure 1.22 Contact poling for **(a)** and non-contact poling for **(b)** [112]

(2) Optimization processing conditions

Process factors, such as pressure, [96] temperature and rate of cooling after the melt or cold drawing, [88, 114] also largely affect the transition of β polymorph and its amount in PVDF. For the effect of pressure, according to Bohlen's study [100] it possibly influences on crystallites from two aspects: one is the intermolecular distances between polymer chains in the crystalline polymorph and the other is the conformation of individual chain in the crystal lattice. Since β polymorph is more compact in the direction perpendicular to the chain, high pressure may promote the transition into more effectively packed β polymorph during the crystallization process.

Secondly, temperature and cooling rate are also essential which affect the content of β polymorphs. Cestari et al. have concluded that α crystallization rate is very high near 130^oC. [114] When a temperature is lower than 100^oC, the rate of β is higher than that of α and the maximum rate of β happens at 60^oC. Additionally, a slow cooling promotes α polymorph while a rapid cooling promotes β polymorph because slow cooling may provide enough time for PVDF chains to adopt its thermodynamically stable structure (α phase). Satyanarayana et al. have also had the similar conclusion via the computational simulation (first principles and MD) and FTIR characterization. [99] Therefore, the content of β polymorph may be improved when a rapid cooling and

high pressure are conducted under crystallization.

(3) Copolymerization with trifluoroethylene

The addition of trifluoroethylene (TrFE) units to PVDF chains induces a structure which is similar as β polymorph and yields high piezoelectric effect. According to MD simulations by Holman et al. [106], in the case of pure PVDF the gauche character increases if cooling from a high temperature. While in the case of PVDF-TrFE the all-trans character increases. It infers that activation's barrier of crystallization into β is hard for pure PVDF to overcome but easy for PVDF-TrFE. Thus PVDF-TrFE may obtain all-trans conformation without drawing or poling. Density functional theory (DFT) and MD calculation carried out by Su et al. also gives similar results that inclusion of TrFE units (50%) has stabilized some all-trans structures. [94]

(4) Addition of CNT

The addition of CNT will also help to induce β polymorph. In the case of CNT reinforced PVDF composites processed by blending, the interactions between CNT and PVDF will promote the amount of β polymorph. Guo et al. have proposed that the fluorine atoms in PVDF chains are attracted to the delocalized π electrons of CNT which makes PVDF chains wrapped around CNT during the melting. [115] A strong π-π interaction at interface of CNT-PVDF may hinder the transition from β polymorph to α phase during crystallization.

The discussions about inducing β polymorph in PVDF by adding CNT can be divided into two scenarios from the view of thermodynamics: [91]

1. The interactions between PVDF and CNT may yield in the interfaces where Gibbs free energy might be lower if PVDF is in β polymorph. In other word, β polymorph may be thermodynamically stable polymorph based on the presence of CNT.

2. α polymorph is still thermodynamically, but β polymorph may appear in the melting or solution stable in the presence of CNT. The interaction of PVDF-CNT might increase barrier of transition from β to α polymorph.

Thus, the difference between these two scenarios is that in the first one, β polymorph is thermodynamically stable while in the second one, β polymorph is

kinetically stable. If the second scenario is valid, the transition from α to β must occur in the melting or solution because the energy barrier of transition from α to β may be overcome if PVDF chains obtain enough energy. In fact, many experimental results have provided the evidence that long term sonication for CNT/PVDF composite promotes β polymorph. Yu et al. have reported that both α and β polymorphs are found in sonicated MWNT/PVDF mixture while only α polymorph exists in unsonication mixtures. [60] Levi et al. have reported that the function of CNT (no matter SWNT or MWNT) may be viewed as the nuclei for rapid crystallization which yields much more β polymorph.[116] Meanwhile, increasing amount of MWNT will also enhance the amount of β polymorph. Moreover, the increment of β polymorph depends on CNT's exfoliating and dispersing in the composite. [91]

Other studies have reported that for MWNT/PVDF composite, if MWNT is modified by ester functionalization [117] or grafted by PVP [118], more amounts of β polymorph may be induced compared with MWNT without surface modification.

About the interactions between CNT and PVDF, there is a disagreement between the experimental results and computational modeling. [91] For experimental results, authors propose that the epitaxial matching between β polymorph of PVDF and hexagonal carbon network of CNT's wall is really important. [115, 117] The strong interactions result from the fluorine atoms of all-trans PVDF chain and π electrons of CNT. Namely, F-π interaction is the key factor for increment of β polymorph. In contrast, computational modeling results by Yu et al. conclude that it is the positively charged hydrogen atoms of β polymorph that interact more strongly with π electrons of CNT (H-π interaction) instead of fluorine atoms. [60] It is hard to judge whether the interaction is F-π or H-π, but the interaction happening on the interface of CNT and PVDF will largely affect dielectric property of the composite which is important for practical application of CNT reinforced PVDF composites.

1.6 Conclusion

In this chapter, we have reviewed basic knowledge of dielectric theory and recent

researches on polymer matrix composites with high dielectric performance. Compared with properties of ceramics and commercial polymers, nanocomposites are widely accepted to be one of the most promising materials for embedded capacitors. Large numbers of researches have shown that nanofiller's dispersibility, interfacial interaction between nanofillers and matrix, suitable processing for nanocomposites and applied polymer matrix's nature are the four key factors for achieving high dielectric property and these four factors always affect mutually with each other.

Firstly, the dispersion of nanofillers will largely determine composite's property. A good dispersion not only reinforces the adhesion between nanofillers and matrix, but also lowers f_c and consequently enhances the dielectric strength of composite. Secondly, interactions between nanofillers and matrix are various including the chemical bonding, van der waals force, π-π interaction and interfacial crystallization, etc. They will largely influence nanofillers' dispersion in polymer matrix which needs to be well studied. Thirdly, processing's method is the base of nanocomposite with high dielectric property. Defects in nanocomposites and the inhomogeneous dispersion of nanofillers need to be avoided as much as possible. Fourthly, the nature of polymer matrix influences dielectric property directly. The original dielectric property, polarity, crystallinity and processing property of polymer matrix are doubtlessly crucial for its nanocomposite's dielectric property.

Hence, in the following parts, we will attempt to prepare nanofillers with novel structures in order to achieve high dielectric property. Meanwhile, the dispersion of nanofillers and the effect of interfaces will also be well analyzed via designing and comparing properties of samples with same two-phase nanofillers but different structures. Additionally, besides experimental works, calculating works will also be conducted to understand further about f_c and conductive network's formation. In this thesis, we aim at achieving composites with high dielectric property by optimizing nanofiller's dispersion and strengthening their interfacial interaction with polymer matrix.

Chapter 2 Synthesis of hybrids with different structures and

polyvinylidene fluoride matrix composites

_____

Introduction

In this chapter, we introduce works for experiments and methods for characterizations. The detail information of BT and CNT hybrids with different structures are provided in this chapter. One is BT particles as cores and CNT growing outside as shells by CVD. The other is BT particles coating on the CNT surface by hydrothermal reaction. Meanwhile, these hybrids' properties including morphology, crystalline phases and component's content are all characterized and discussed in the related parts. Additionally, processing way for PVDF matrix composites is also mentioned in this chapter.

2.1 Materials for the experiments

All the information of materials used for experiments is listed in *table 2.1* including their names, molecular formula, physical states, purity and providers.

Table 2.1 Materials for the experiments

Materials	Molecular formula	Physical states	Purity	Notes
Iron (III) nitrate nonahydrate	$Fe(NO_3)_3 \cdot 9H_2O$	s*	98%	Sigma Aldrich
Barium titanate	$BaTiO_3$	s, (<2μm)	99.9%	Sigma Aldrich
Barium hydroxide octahydrate	$Ba(OH)_2 \cdot 8H_2O$	s	99.9%	Sigma Aldrich
Titanium (IV) butoxide	$TiC_4H_9O_4$	l*	97.0%	Sigma Aldrich
Ethanol	C_2H_5OH	l	96%	
Dimethylformamide	$HCON(CH_3)_2$	l	99.8%	Sigma Aldrich
Argon	Ar	g*		Carrier gas
Hydrogen	H_2	g		Carrier gas
Acetylene	C_2H_2	g		Carbon source

* s, l and g stand for solid, liquid and gas, respectively

PVDF powder is provided from Arkema Group and main physical properties are listed in *table 2.2*.

Table 2.2 The specification of Arkema Group Kynar 720 PVDF

Physical property	Index	Physical property	Index
Density (g/cm^3)	1.78	Volume resistivity (*ohm.cm*)	1.5×10^{14}
Melting point (^oC)	171	Thermal conductivity (*W/(mK)*)	0.19
Thermal decomposition (^oC)	375	Heat capacity (*J/(g^oC)*)	1.17-1.51

2.2 Characterization's methods

The as-prepared samples are characterized by following techniques:

Morphology characterization for hybrids and fractures surfaces of composites is conducted by scanning electron microscope (SEM) (LEO Gemini 530). Composites are broken by impregnated in the liquid nitrogen for five minutes. The energy-dispersive X-ray spectroscopy (EDS) and scanning transmission electron microscope (STEM) are conducted by Titan^3 G2.

Thermal gravimetric analysis (TGA) is conducted by thermo gravimetric analysis (NETZSCH STA 449F3).

Differential scanning calorimetry (DSC) is conducted by thermo gravimetric analysis (NETZSCH STA 449F3). The temperature range is from 25 to 200^oC with the rate of $10^oC/min$. The DSC program includes two heating–cooling cycles. Melting and crystallization temperatures are determined from the second heating–cooling cycle.

X-ray diffraction (XRD) of hybrids is measured by the D2 Phaser X-ray Powder Diffraction, Bruker.

Dielectric properties of composites are characterized as a function of frequency by the impedance analyzer (Solatron 1260). Before measurement, silver layer is applied on the sample's two sides for increasing contacting. The measurement of dielectric property after thermal treatment is as follows: The sample is annealed at a set temperature for 30min and then cooled down to room temperature. The dielectric property is measured after the sample is cooled down to room temperature.

The synchrotron X-ray measurements are conducted under synchrotron sources at Advanced Photon Source at Argonne national laboratory (USA) on 5-ID-D beam-line. Medium angle detector is used with range of $0.12 \leqslant q \leqslant 0.70 \mathring{A}^{-1}$. The sample is put in the Al_2O_3 crucible and well packed by the press tablet machine. The measurement procedure is corresponding to thermal treatment. Namely, the sample is

firstly heated from 30 to 150^oC with the rate of $10^oC/min$. And then the temperature maintains at 150^oC for $30min$ and afterward it is cooled down to 30^oC with the same rate. One thing should be mentioned is that although in the X-ray measurement, the temperature is set at 150^oC for the measurement but actually it is at 143^oC. This difference between set annealing temperature and actually tested temperature for thermal treatment is also existed in the dielectric measurement. The heater is set at 150^oC but the measured temperature is at 138^oC by the thermocouple. The exposure time of beam is $0.1s$ which depends on sample's properties. The time between each frame is $6s$. Generally the smaller value is used, the more scanning information will be detected but more time is needed too. In our case, we use normal mode for the measurement. The number of frames is largely dependent on the procedure of DSC thermal process and it needs a simple calculation.

2.3 Synthesis of carbon nanotube-BaTiO₃ hybrids

2.3.1 Method of synthesis

Carbon nanotube-BaTiO₃ hybrids (H-CNT-BT) are produced via the floating catalytic CVD process. Acetylene (C_2H_2) is used as carbon source and iron (III) nitrate nonahydrate ($Fe(NO_3)_3 \cdot 9H_2O$) as the catalyst precursor. The preparation procedure can be divided into two steps: (1) preparation of catalyst nanoparticles on BT by the impregnation way and (2) CVD reaction. The procedure is described as follows:

Firstly, for impregnation: BT with $Fe(NO_3)_3 \cdot 9H_2O$ are dissolved in ethanol by magnetic stirring for $1h$ at room temperature and heated at 70^oC to evaporate the solvent. Afterward, the mixture is calcined at $450°C$ in a tube furnace for $1h$ in order to oxidize $Fe(NO_3)_3$ to Fe_2O_3.

Secondly, for CVD, the prepared BT-Fe_2O_3 mixture is homogeneously dispersed on the surface of a quartz plate ($3 \times 50cm^2$). Afterwards the quartz with powders is put into the middle of a furnace for the reaction ($60cm$ in length). The temperature of CVD is between 600 to 800^oC under argon and hydrogen atmosphere. Herein, gas

flows are accurately controlled by electronic mass flow meters (Bronkhorst, France). After heating to the set temperature and becoming stably, acetylene as the carbon source is introduced into the reactor. After 30*min*, the furnace is cooled down naturally under the argon atmosphere.

In the process of synthesizing H-CNT-BT, there are two main aspects involved: one is the impregnation of BT particles in $Fe(NO_3)_3 \cdot 9H_2O$ solvent and the other is the growth of CNT on BT particles. Both of them are greatly affected by experimental conditions (e.g., chemical agencies' ratio, gas flow rate and reaction temperatures, etc.) as well as the nature of substrate particles (e.g., size, shape and surface chemical properties, etc.). Hence, in this part, we focus on three experimental parameters: the weight ratio between BT and $Fe(NO_3)_3 \cdot 9H_2O$, the reaction temperature, and the flow rate of H_2, respectively, in order to study their effects on CNT's morphology and quantity in H-CNT-BT hybrids.

2.3.2 Effect of the weight ratio between BaTiO$_3$ and Fe(NO$_3$)$_3$•9H$_2$O

(a)   **(b)**

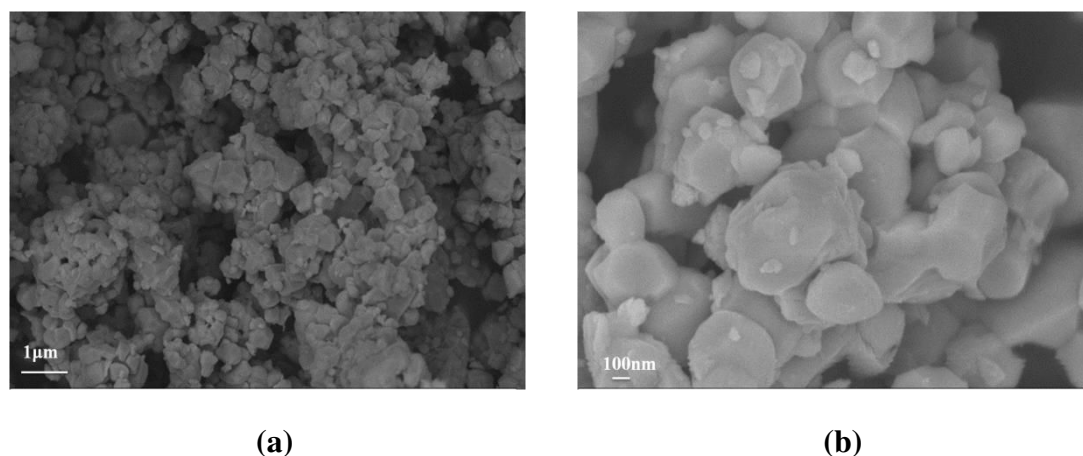**Figure 2.1** SEM images of the pure BaTiO$_3$ (BT) observed under different magnifications. **(a)** is the 10*k* and **(b)** is 50*k*, respectively.

Before impregnated in $Fe(NO_3)_3 \cdot 9H_2O$ solvent, pure BT particles are characterized by SEM in order to have a comparison in morphology with ones after impregnated Fe_2O_3. As shown in *Figure 2.1*, pure BT particles are not homogeneous

in diameter and their size range is from 100nm to 1μm. Shapes of particles are not regular and most of them are mixed with sphere and cubic. Meanwhile, observing the enlarged image in *Figure 2.1 (b)*, we find that some particles' surfaces are smooth and others are covered by fragments of particles with the size around 100nm. Most particles are agglomerated with each other which increase the average size of clusters and consequently may provide more surface area for CNT's growth.
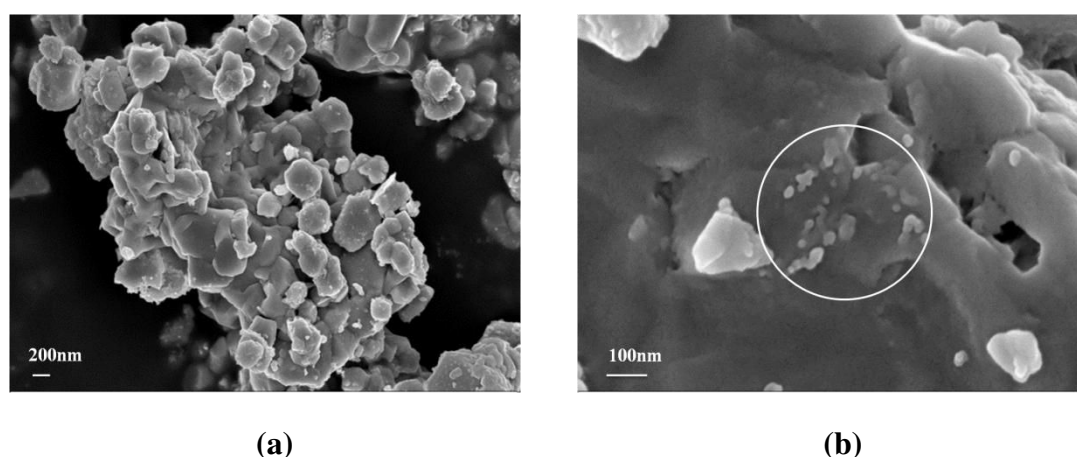

(a)   **(b)**

Figure 2.2 SEM images of BT-Fe$_2$O$_3$ mixture with weight ratio of 85:15. **(a)** is 20k and **(b)** is 100k, respectively.

After the impregnation, in *Figure 2.2* we find that there are some small and round nanoparticles (Fe$_2$O$_3$) with the size from 15 to 30nm dispersed on the surface of BT. These Fe$_2$O$_3$ particles trend to stick on BT particles with larger size and coarser surface. A possible reason may be attributed to the impregnation of BT/Fe$_2$O$_3$. Due to the poor solubility of BT in ethanol, a few BT particles can be impregnated by Fe(NO$_3$)$_3$ solution while others sink in the bottom and have less incubation. Furthermore, during ethanol's evaporation process, BT particles are also unavoidably precipitated in the bottom owning to its high density that intensifies the inhomogeneous impregnation of the whole BT particles in Fe(NO$_3$)$_3$•9H$_2$O solvent. Additionally, during calcinations, the agglomeration of Fe$_2$O$_3$ may be caused by thermal movement agitated at high temperature. Although the inhomogeneous dispersion of catalyst on BT particles, impregnation way is still applied for catalyst's

preparation because of its easy process and efficiency for the afterwards CVD reaction.

After describing BT and BT/Fe_2O_3's morphologies, we start the discussion on CNT's growth by CVD. The weight ratio between BT and $Fe(NO_3)_3$ is investigated and we choose four weight ratios (80:20, 85:15, 90:10 and 95:5, respectively) for the study. CVD conditions for the four samples are the same: before CVD's reaction, the mixture of BT/Fe_2O_3 is under H_2 reduction for 10*min* in advance for reducing Fe_2O_3 into Fe nanoparticles. And then CVD reaction is conducted at 750^oC for 30*min* with a mixture of gas flows: Ar=1*l/min*, H_2=0.1*l/min* and C_2H_2=0.05*l/min*, respectively.

Comparing with SEM images shown in *Figure 2.3*, we find that the weight ratio of BT and $Fe(NO_3)_3 \bullet 9H_2O$ has largely influences the growth of CNT. Firstly, comparing with the morphology of CNT in *Figure 2.3 (a)* and *(b)*, we find that the diameter of CNT in *(a)* is less homogeneous than that in *(b)*. In *Figure 2.3 (b)*, the diameter of CNT is around 25*nm* and the length is longer than 2*μm*. Whereas, in *Figure 2.3 (a)* marked by white circles, we can find that some CNTs grow very gross (the diameter is larger than 40*nm*) while others grow slim (the diameter is less than 15*nm*). A possible reason is the over dose of Fe_2O_3 incubated on BT particles may intensify the agglomerations of iron nanoparticles in the reduction process. According to the reference [34], a general experience shows that the catalyst particles size dictates the diameter of CNT. Although, the growth of CNTs in H-CNT-BT by CVD runs in a not well-defined mechanism, it is mostly assumed to involve three procedures: (1) the adsorption and decomposition of the acetylene on active points of the iron catalyst, (2) the formation of iron-carbon intermediate species, and (3) finally the growth of CNTs. This mechanism infers the importance of metallic particle's size for the morphology of obtained CNT. Given that the catalyst impregnated on BT surface is over dosed, the size of catalyst is prone to be inhomogeneous. This difference in the size of catalytic nanoparticles probably leads to various diameters in CNT. Moreover, a negative result which even influences the quality of CNT is that when the size of metallic particles increase, the formation of nonselective forms of carbon (carbon nanofibers, amorphous carbon, etc.) are favored rather than CNT. This can also be found and
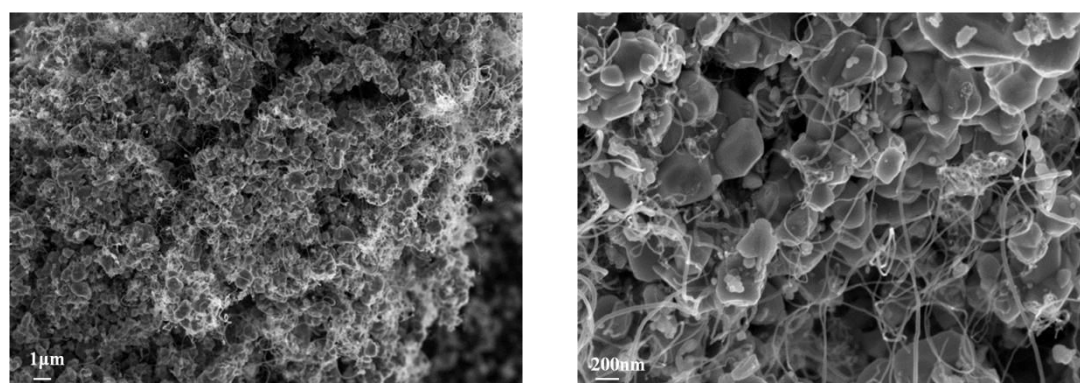
marked in white cycles of *Figure 2.3 (a).* Hence, if the weight ratio of $Fe(NO_3)_3$ and BT is over dosed and the agglomeration of catalyst nanoparticles on BT is obvious which affects negatively not only on CNT's morphology but also on its quality and property.
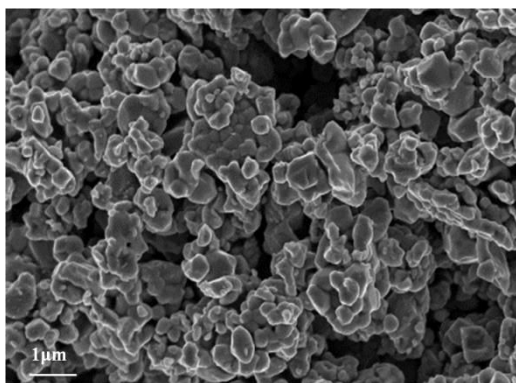

(a)

(b)

(c)
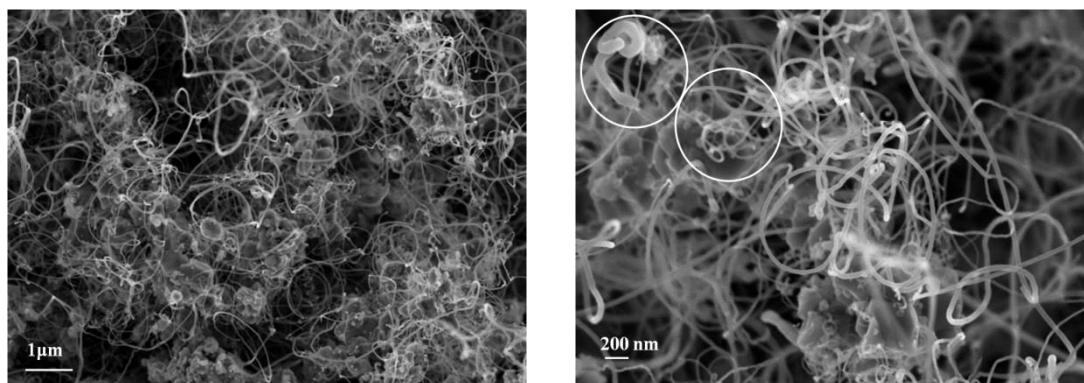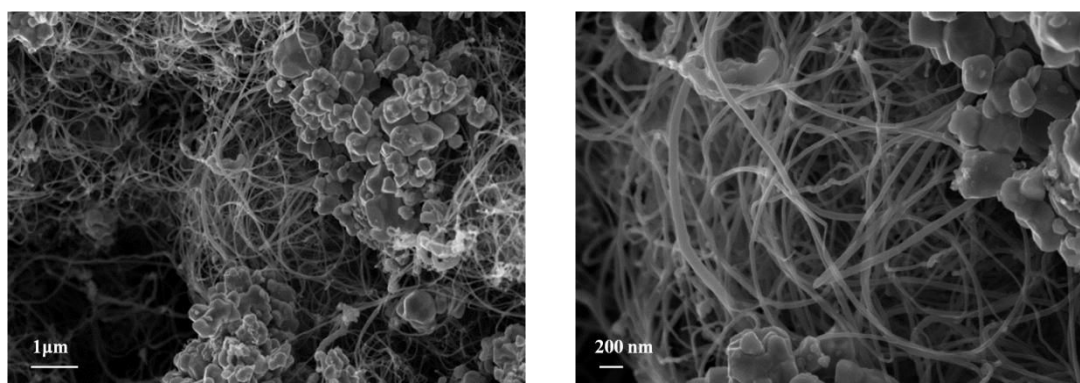
Figure 2.3 SEM images of H-CNT-BT with different weight ratios of BT and Fe(NO₃)₃•9H₂O: **(a)**: 80:20, **(b)**: 85:15, **(c)**: 90:10 and **(d)**: 95:5, respectively. The left ones are with small magnitude and the right ones are with large magnitude.

(d)

On the contrary, if the ratio of $Fe(NO_3)_3$ and BT is not enough, there will be less CNT grown on the BT as shown in *Figure 2.3 (c)*. Moreover, if the ratio is smaller, as shown in *(d)*, nearly no CNT will grow on BT due to lacking catalyst. It is known that the key factor for CNT's growth is to achieve acetylene decomposition on the iron catalyst surface rather than aerial pyrolysis. The smaller amount of catalyst has on BT, the less possibility of contact between hydrocarbon and catalyst will be so that CNT growth will be limited. This infers that a very small amount of catalyst in hybrids is not able to induce the growth of CNT. Similar result has also concluded by Perez-Cabero et.al's studies on the synthesis of MWNT by CVD. [119] These SEM images in *Figure 2.3* show us that the property of CNT strongly depends on the iron content. If the ratio of BT and $Fe(NO_3)_3$ is too small, less or even no CNT will grow on BT. Conversely, if the ratio is excessive, the amorphous carbon will be formed around CNT which is harmful for the quality of CNT and moreover the morphology is also negatively influenced.

Therefore, the ratio of 85:15 is chosen for the rest of experiments due to the relatively homogeneous morphology of CNT. However, there is still a problem shown in *Figure 2.3 (b)*: not all BT particles have been covered by CNT. Besides the inhomogeneous disposal of iron catalyst on BT's surfaces mentioned before, another possible reason may be caused by the procedure of H_2 reduction before CVD. Because there is no chemical bonding between BT and Fe_2O_3, the interaction between Fe_2O_3 and BT particles is weak. According to the reference, [34] it is known that the

physical state of catalyst may change during CVD process: in the case of acetylene decomposition on nickel catalyst supported on silica and graphite substrates at 600^oC, metallic particles change the shape and move up with a trail of carbon deposit. In our case, the temperature used for H-CVD-BT is 750^oC. It is highly possible that the movement and agglomeration of the iron nanoparticles may occur in the process of pre-reduction before CVD, and finally result in the partial growth of CNTs on BT. In order to reduce this negative effect, a shorter induced reaction time may be better for the homogeneous growth on BT. Thus, the step of pre-reduction of H_2 will be deleted in the following experiments and CVD will start directly as soon as the temperature is stabilized to the set value.

2.3.3 Effect of the reaction temperature

The CVD conditions for this part are as follows: the mixture of BT/Fe_2O_3 (85:15) is used for the reaction without H_2 reduction in advanced. Different temperatures (600, 650,700, 750 and 800^oC) are set and the reaction time is 30*min*. The gas flows are: Ar=1*l/min*, H_2=0.1*l/min* and C_2H_2=0.05*l/min*. The morphologies of H-CNT-BT at five reaction temperatures are shown in *Figure 2.4* from *(a)* to *(e)*, respectively.

(a)

(b)

(c)

(d)

(e)
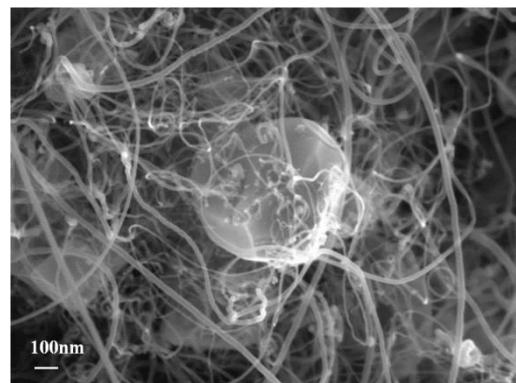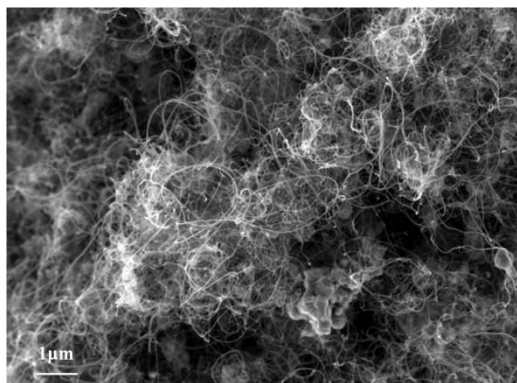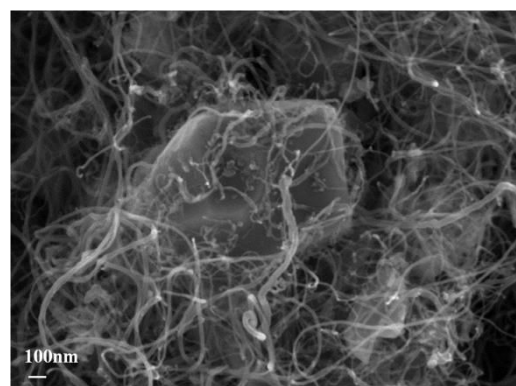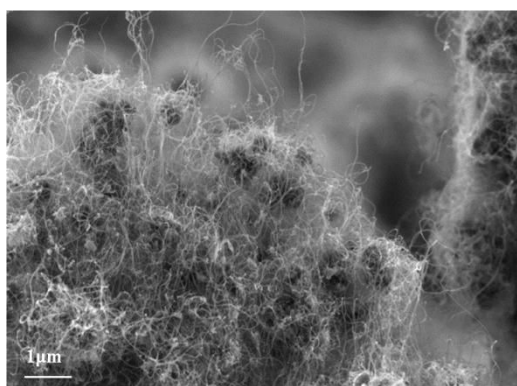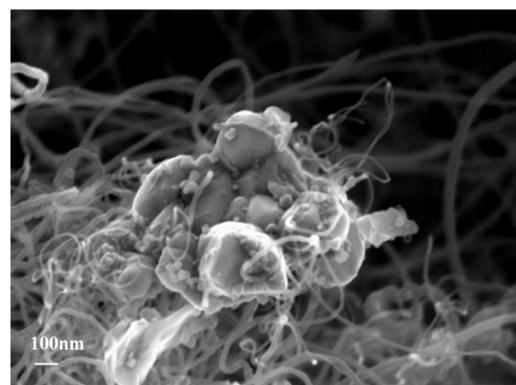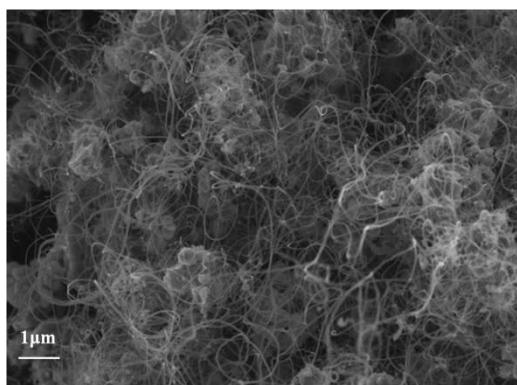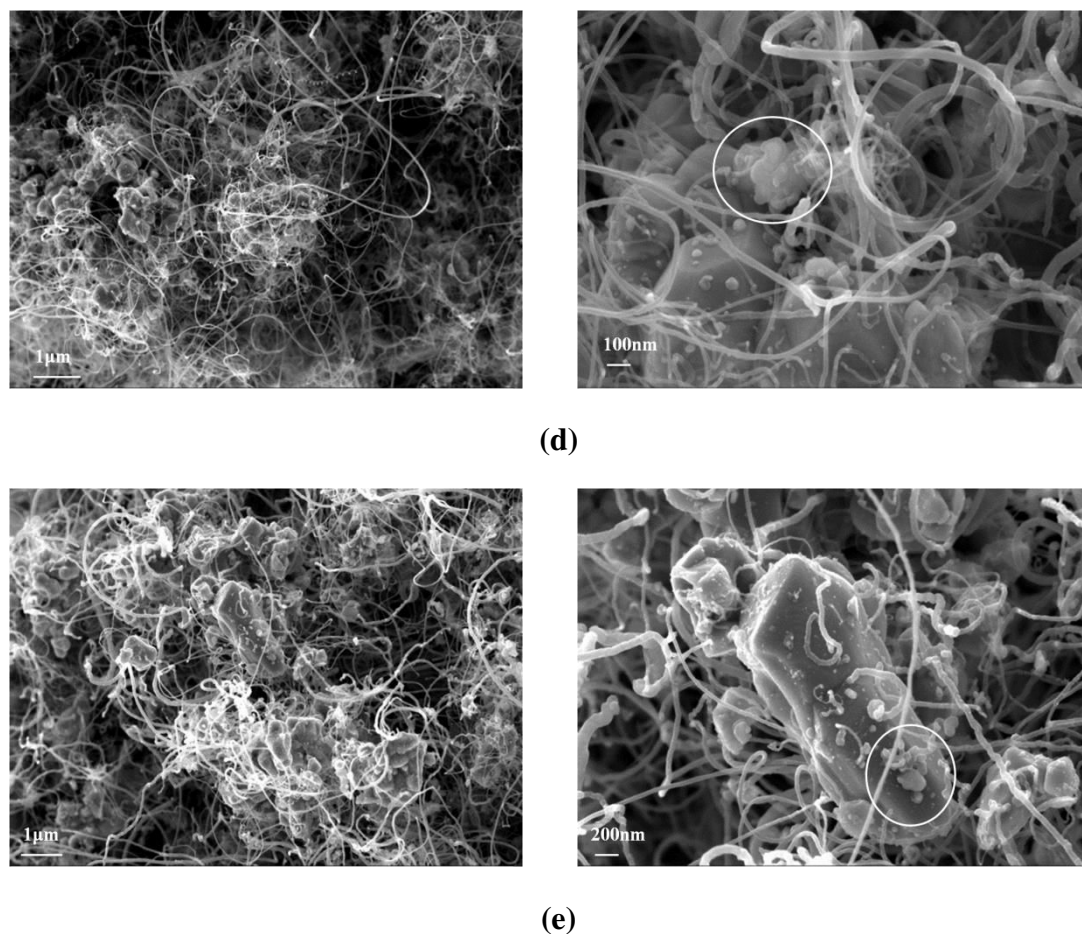
Figure 2.4 SEM images of H-CNT-BT at different temperatures: **(a)** 600^oC, **(b)** 650^oC, **(c)** 700^oC, **(d)** 750^oC and **(e)** 800^oC, respectively. The right images are the enlarged ones for the left.

Firstly, comparing with five series of SEM images in *Figure 2.4*, we find that the general shape of CNT obtained is a bit straight without too many curves. It is because the acetylene is used for hydrocarbon source. In general, the molecular structure of precursor has the detrimental effect on the morphology of CNT's growth. Linear hydrocarbons usually decompose thermally into atomic carbon or linear/dimmers/trimers of carbon which promote to the straight and hollow CNT's production. [120,121] Acetylene is a kind of linear hydrocarbons and thus CNTs in H-CNT-BT is nearly straight without many curves. Secondly, we can find that as the temperature increasing, the amount of CNTs grown on BT reduces and moreover, the diameter becomes inhomogeneous. From SEM images, we find that morphologies of

CNT in H-CNT-BT are more uniform at lower temperatures (600 and 650°C). When the temperature increases to 750 or 800°C, more amorphous carbon appears in the system which is marked in *Figure 2.4 (d)* and *(e)* by white cycles. Two reasons may cause this negative effect from higher temperature. On the one hand, CNT nucleation and growth are usually dominated by two factors. One is the diffusion of catalyst nanoparticles on BT's surfaces and the other is carbon pyrolytic reactions in the gas phase. Considering Oswald ripening mechanism [122], a high temperature usually causes small particles coalescing into big ones and thus reduced iron nanoparticles are easy to move and agglomerate which affects the homogeneous morphology of the CNT on BT particles.

On the other hand, the carbon resource used for H-CNT-BT is acetylene, a kind of hydrocarbons whose pyrolysis temperature is ranging from 450 to 600°C. Except for methane and other light paraffins, most hydrocarbons (C_nH_m) usually have a positive value of Gibbs function of formation Δ_fG^o (variation of the Gibbs free energy of the system that occurs during the formation reaction from graphite and hydrogen) at all temperatures under standard state conditions. This is a criterion of how far the standard-state is from equilibrium according to the following reaction:

$$C_nH_m \rightleftarrows nC_{graphite} + \frac{m}{2}H_2$$

The relationship between Gibbs function of reaction at any moment on time (Δ_rG) and the standard-state Gibbs function of reaction (Δ_rG^o) is described by the following equation:

$$\Delta_rG = \Delta_rG^° + RTlnQ$$

where *R* is the ideal gas constant and *Q* is the reaction quotient at that moment in time. At the equilibrium, *$\Delta_rG=0$* and *Q=K*, where *K* is the equilibrium constant. Partial pressures of H_2 and of C_nH_m, *P_{H2}* and *P_{CnHm}* (in bars), verify $K=P_{H2}^{m/2}/P_{CnHm}$ and *RTlnK=-Δ_rG^o=$\Delta_fG^o(C_nH_m$)*. *K* and *Δ_fG^o* $_{CnHm}$ both are determined by the reaction temperature. [122]

Thus, in the case of acetylene used in H-CNT-BT system, *$\Delta_fG^o_{C2H2}$=225.31-0.054T (kJ/mol)* and *K=P_{H2}/P_{C2H2}=exp(27098/T-6.5)* are reducing

when the temperature increases from 600 to 800^oC. The calculation results for five temperatures are available in *table 2.3* as follows.

Table 2.3 Gibbs function of formation and equilibrium constant for the decomposition reaction of acetylene

T (^oC)	600	650	700	750	800
$\Delta_f G^o_{C2H2}$ (*kJ/mol*)	178.2	175.5	172.8	170.1	167.4
K	4.55×10^{10}	8.46×10^9	1.87×10^9	4.8×10^9	1.4×10^8

From the calculation in *table 2.3*, we can find that the decomposition of acetylene is thermodynamically and controlled by kinetics. The equilibrium constant of reaction, *K*, is much higher at lower reaction temperature which demonstrates that lower reaction temperature (from 600 to 700^oC) promotes the CVD reaction to the equilibrium state. Furthermore, if reaction's temperature is high, the movement of gas molecules are intensified which may cause the amorphous carbon appearing on BT surface so that affects the quality of CNTs. Hence, a higher temperature (over 700^oC) is not favor to CNT's growth in H-CNT-BT system. In addition, if comparing with these enlarged SEM images in the right columns of *Figure 2.4* from *(a)* to *(e)*, we observe that some small catalyst nanoparticles are not only remained on BT surfaces but also in the inner of CNTs or on the top of them. This phenomenon may suggest that CNT in H-CNT-BT grows via base-growth coexisting with tip-growth model.

In *Figure 2.5*, the pink region of mass loss from 500 to 600^oC is CNT's thermal decomposition temperature range. We find the amount of CNT in H-CNT-BT also depends on the reaction temperature. When the reaction temperature increases from 600 to 650^oC, the amount of CNTs will increase from 7.88% to 9.36%. Meanwhile, the maximum appears at 650^oC. Afterward, as the reaction temperature further increases, CNT's content decreases gradually. This is also observed in the SEM images of *Figure 2.4*. Therefore, the amount of CNT measured by TGA also supports that 650^oC is the suitable temperature for CNTs growth on BT particles.
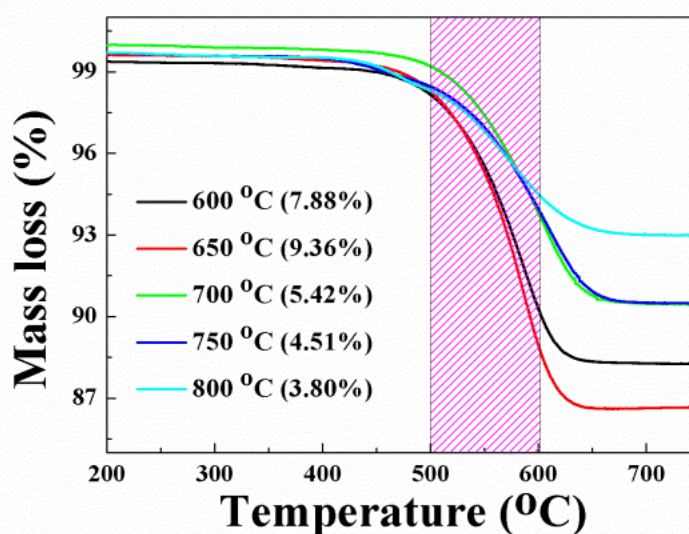
Figure 2.5 TGA for H-CNT-BT synthesized at different temperatures

2.3.4 Effect of hydrogen flow rate

The CVD conditions for this part are as follows: the mixture of BT/Fe_2O_3 (85:15) is used for CVD reaction without H_2 reduction in advanced. The reaction is conducted at 650^oC for 30*min* under the gas flows: Ar=1*l/min* and C_2H_2=0.05*l/min*, respectively. We choose three flow values of H_2: 0.05, 0.1 and 0.2*l/min*, respectively, for experiments.

By calculating the mass loss values from 500 to 600^oC in the pink region of *Figure 2.6*, we find that when *H_2=0.1l/min*, the amount of CNTs will reach the maximum. Usually, there are two different influences brought by H_2 during CVD reaction: the positive one for CNT's growth is to reduce Fe_2O_3 into Fe nanoparticles effectively which is able to catalyze CNT growth. While the negative one is to slow down dehydrogenation's rate of acetylene and impede the formation of sp^2-like carbon structures. [123] These two points affect mutually and an optimized value is needed by balancing both of them. Thus, we will also investigate the effect of hydrogen flow rate on CNT's morphology in H-CNT-BT.
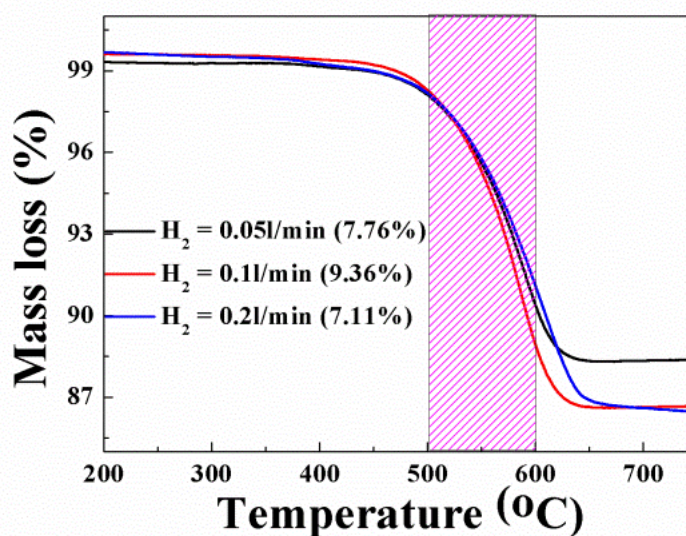
Figure 2.6 TGA for H-CNT-BT synthesized with different H_2 flow rates

Compared with SEM images of different H_2 flow rates shown in *Figure 2.7* from *(a)* to *(c)*, we find that increasing H_2 flow rate affects not only the amount but also the diameter of CNT. Meanwhile as H_2 rate increasing, the distribution of CNT's diameter is also les homogeneous. It is still attributed to the agglomeration of Fe nanoparticles since more Fe_2O_3 are reduced under more H_2, the possibility of inhomogeneous distribution of iron catalysts on BT particles also increases which affects negatively on CNTs' morphology. That less amount of CNTs on BT particles shown in *Figure 2.7 (c)* proves again the negative role of hydrogen in the dehydrogenization of acetylene on catalyst particles. Thus H_2 flow ratio in the carrier gases plays an essential role on CNTs' growth in H-CNT-BT. In our system, the H_2 flow rate of 0.1*l/min* will be the appropriate one according to the result of TGA and SEM images of obtained CNT.

(a)

(b)

(c)
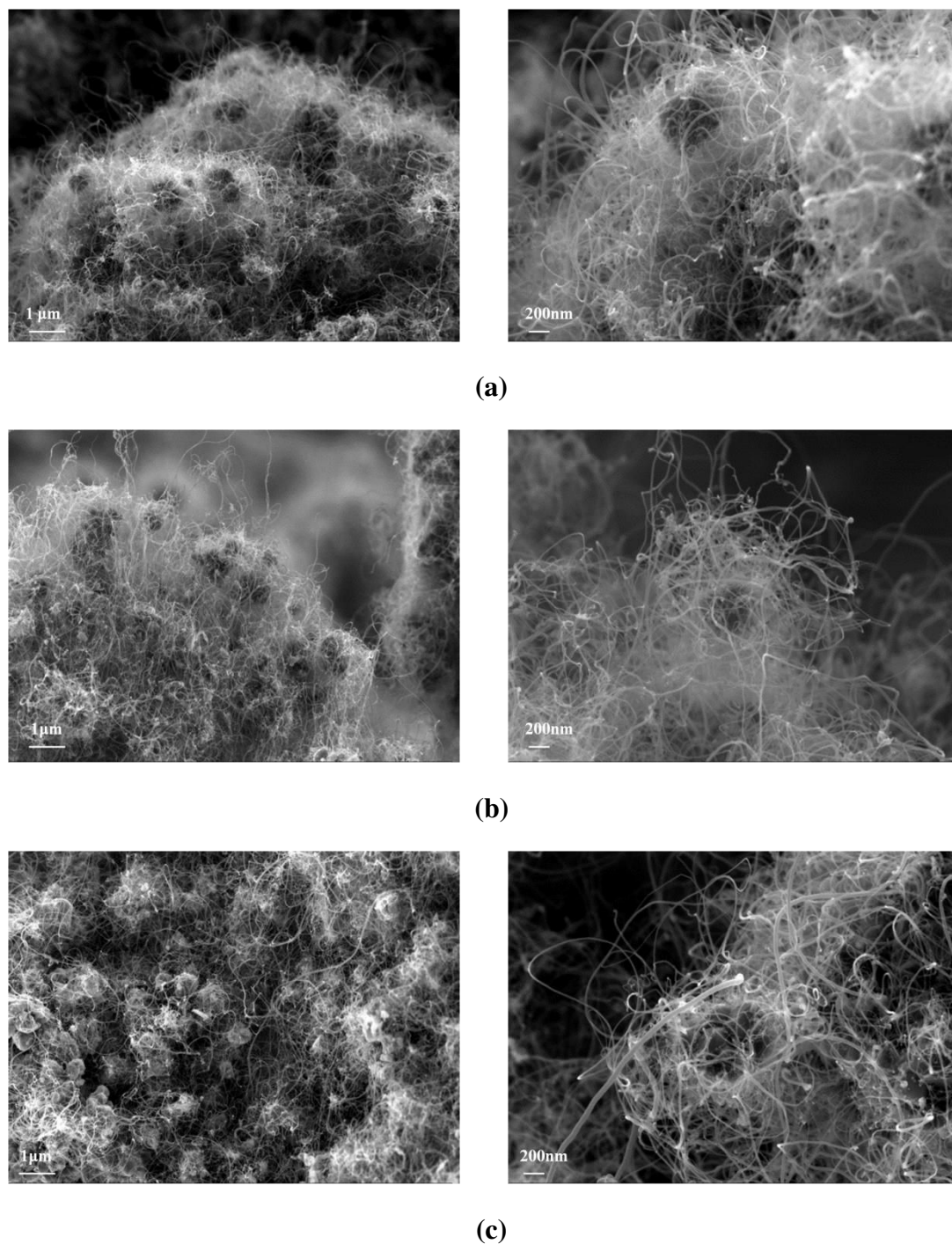
Figure 2.7 SEM images of H-CNT-BT synthesized with different H_2 flow rates: **(a)**: 0.05*l/min*, **(b)**: 0.1*l/min* and **(c)**: 0.2*l/min*, respectively. The right images are the enlarged ones for the left.

Therefore, for the summary of experimental data, we conclude that conditions for the synthesis of H-CNT-BT in following experiments are: the weight fraction of BT and $Fe(NO_3)_3 \cdot 9H_2O$ is 85:15. The reaction temperature is 650^oC and the H_2 flow

rate is $0.1 l/min$.

2.4 Synthesis of BaTiO$_3$-carbon nanotube hybrids

2.4.1 Method of synthesis

BaTiO$_3$-carbon nanotube hybrids (H-BT-CNT) with BT coating CNT are synthesized by two steps. The first step is coating titanium dioxide (TiO$_2$) on the surface of modified CNT. The second step is crystallizing BT by means of the hydrothermal reaction between TiO$_2$ (coated on the surface of CNT in the first step) and Ba(OH)$_2$•8H$_2$O. The whole experimental procedures can be divided into seven steps:

(1) CNT is modified by concentrated nitric acid (65%) at 110^oC for $2h$ with water refluxing. Afterward, the modified CNT is washed by pure water and dried in oven.

(2) Surface modified CNTs ($0.05g$), certain content of ammonia solution (25%) and absolute ethanol are mixed in a single flask by ultrasonic dispersion in ice bath for $30min$.

(3) The solution of tetrabutyl titanate (TBOT) and ethanol is droplet into the single flask with fiercely magnetic stirring.

(4) After the hydrolysis reaction, the product is heated at $70°C$ for removing solvent.

(5) Ba(OH)$_2$•8H$_2$O and obtained mixture (precursor of CNT-TiO$_2$) with certain ratio are magnetically stirred in a hydrothermal reactor for $1h$.

(6) Hydrothermal reaction is conducted in the oven at the set temperature.

(7) After the reactor cooled down, the product is washed by pure water and ethanol for three times and finally drying in the oven at 100^oC.
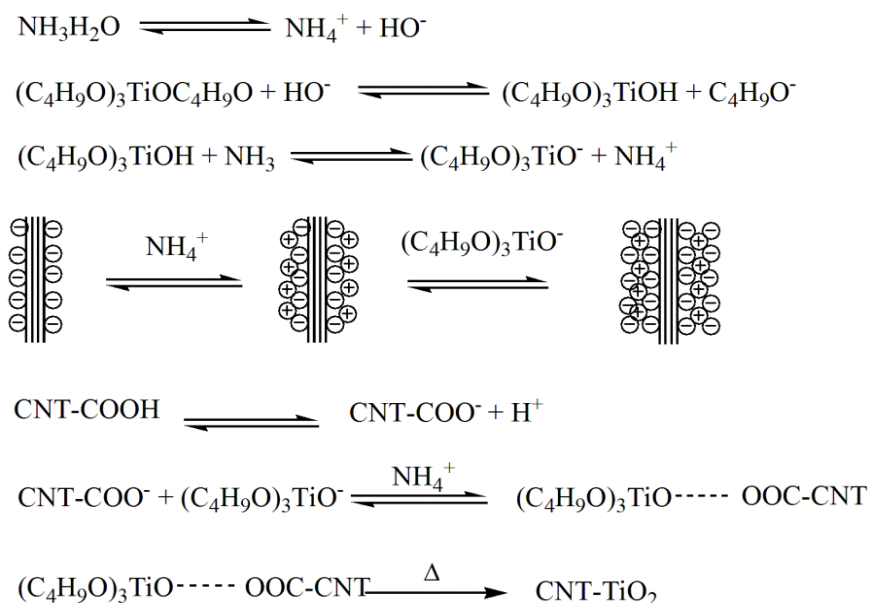
2.4.2 Coating TiO$_2$ on the modified carbon nanotubes

$$NH_3H_2O \rightleftharpoons NH_4^+ + HO^-$$

$$(C_4H_9O)_3TiOC_4H_9O + HO^- \rightleftharpoons (C_4H_9O)_3TiOH + C_4H_9O^-$$

$$(C_4H_9O)_3TiOH + NH_3 \rightleftharpoons (C_4H_9O)_3TiO^- + NH_4^+$$

$$CNT\text{-}COOH \rightleftharpoons CNT\text{-}COO^- + H^+$$

$$CNT\text{-}COO^- + (C_4H_9O)_3TiO^- \xrightarrow{NH_4^+} (C_4H_9O)_3TiO\text{-----}OOC\text{-}CNT$$

$$(C_4H_9O)_3TiO\text{-----}OOC\text{-}CNT \xrightarrow{\Delta} CNT\text{-}TiO_2$$

Figure 2.8 The chemical reactions for the hydrolysis of coating TiO$_2$ on CNT

Coating TiO$_2$ on modified CNT is the first step for synthesis. The main reaction in this step is TBOT's hydrolysis which is illustrated in *Figure 2.8*. The process is a dynamic equilibrium of condensation and dissolution which is greatly influenced by the reaction duration and content of ammonia solution. [124-126] A study of TiO$_2$ conversion on CNT will help us to find a suitable chemical reaction condition for hydrolysis. As illustrated in the chemical reaction of TBOT's hydrolysis in *Figure 2.8*, the addition of ammonia solution catalyses the TiO$_2$ precursor coating on the surface of CNT. Since the modified CNT and the product of TBOT hydrolysis are both with negative zeta potentials, they need positive zeta potential ions to bridge them. NH$_4^+$ in ammonia solution enables to provide the positive zeta potential and associate the modified CNT with the production of TBOT's hydrolysis. However, TBOT is really sensitive to water, even to water vapor in the air. The ammonia solution is a kind of an aquarium solution (25%) which affects TBOT's hydrolysis reaction negatively. Hence, the content of ammonia solution is a key factor for the conversation. By the

investigation for three contents of ammonia solution by TG analysis, we find that when the content is 0.2*ml*, the whole reaction is not stable with the time. When the content is 0.4*ml*, the conversation of TiO$_2$ becomes less. Thus, combining with the reaction's stability and TiO$_2$'s conversation, 0.3*ml* is a suitable content for the coating. The measurement of TGA is shown in *Figure 2.9*.
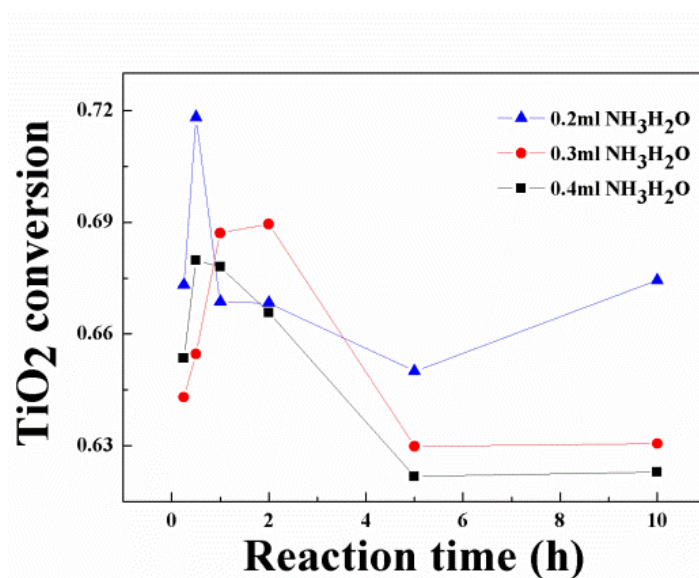
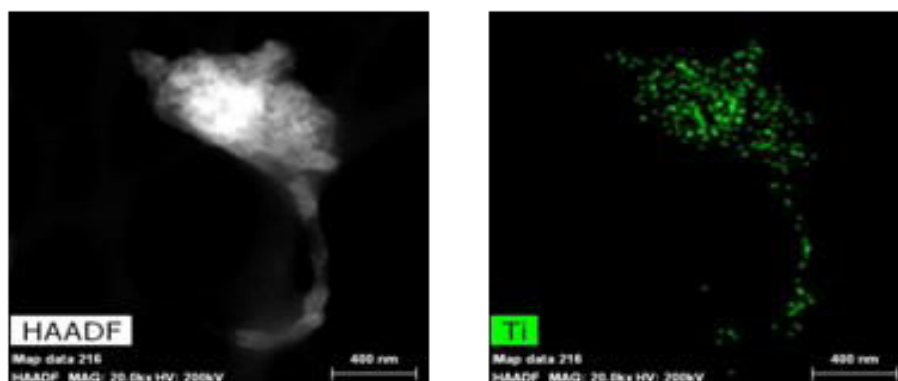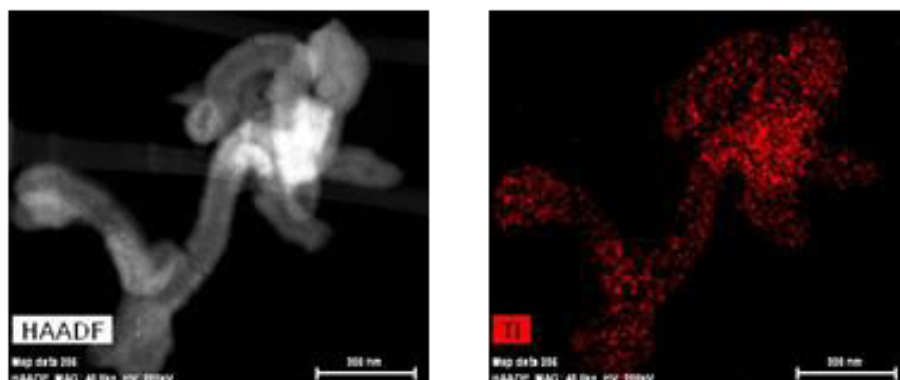**Figure 2.9** Influence of different NH$_3$H$_2$O contents on TiO$_2$ conversion measured by TGA

Meanwhile, we investigate the effect of reaction duration on the morphology of TiO$_2$ coating on CNT. The results of STEM and EDS are shown in *Figure 2.10*.

66

(a)

(b)
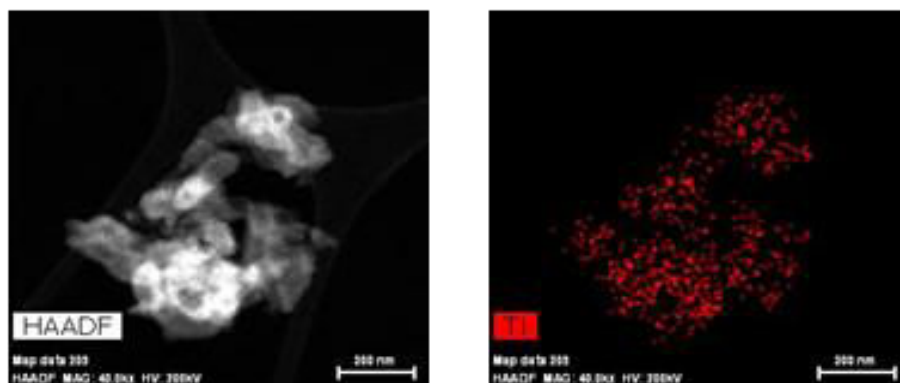
(c)
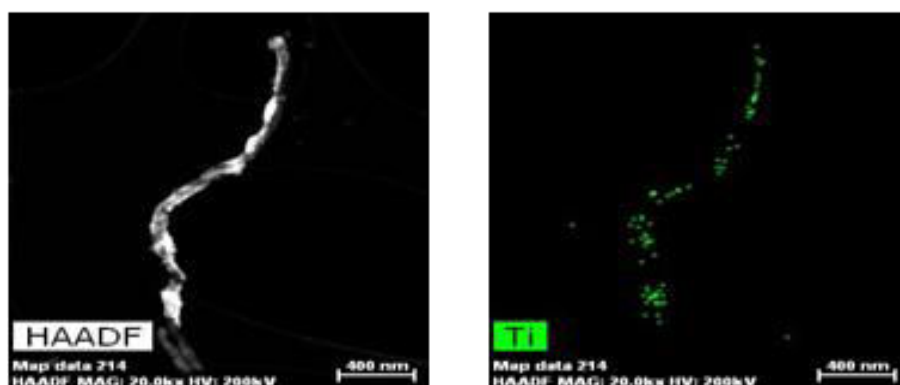
(d)
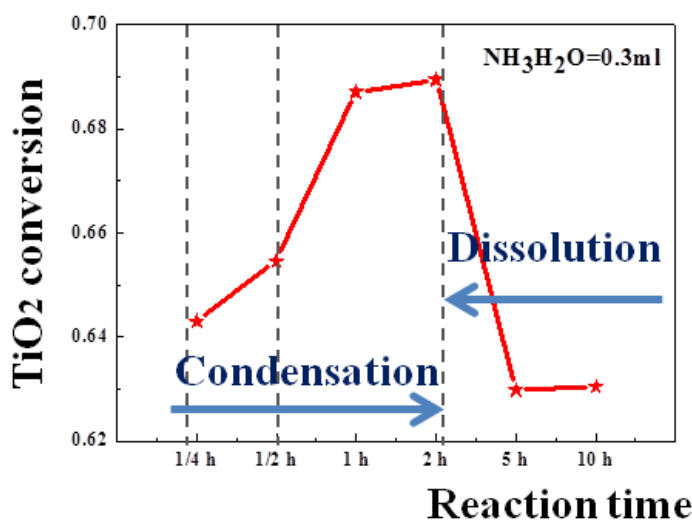
(e)

Figure 2.10 Influence of different reaction durations with NH_3H_2O (0.3*ml*) on morphology. The STEM images (left) and EDS for Ti (right) are shown in **(a)** for 15*min*, **(b)** for 30*min*, **(c)** for 2*h* and **(d)** for 5*h*, respectively. **(e)** is the TiO2 conversion at different reaction duration tested by TGA.

From *Figure 2.10*, we find that at the beginning of the hydrolysis, the precursors of TiO_2 start to accumulate on surfaces of modified CNTs. The agglomeration and inhomogeneous disposal of TiO_2 are obvious in the STEM of 15*min*. As the reaction duration prolonging, in the STEM of 30*min* and 2*h*, the agglomeration becomes less than before due to fiercely magnetic stirring. Especially for 2*h*, we can see TiO_2 almost coats on the whole surface of CNT. However, when the duration reaches 5*h*, the content of TiO_2 precursor decreases which can not only be seen on the morphology but also in the TGA of *Figure 2.10 (e)*. It results from the equilibrium between condensation and dissolution of TBOT's hydrolysis which we mentioned before.[127] Therefore, according to the results of characterization for TiO_2 content and morphology, a chosen condition of coating TiO_2 on surfaces of modified CNTs are 0.3*ml* ammonia solution and the reaction duration of 2*h*.

2.4.3 Crystallization of BaTiO$_3$ by hydrothermal reaction

The crystallization process of solid phases under hydrothermal conditions are usually conducted at autogenously pressure, achieved via particular saturated vapor pressure of the solution at specified temperature and the composition of hydrothermal solution. In this case, temperature, duration and pressure for hydrothermal reaction are three important factors which influence the crystallization process. Hence, for preparation of H-BT-CNT, we will also focus on these three factors and try to find a suitable experimental condition.

At first, we use two temperatures, 180 and 200°C, respectively as reaction temperatures and XRD is used for the analysis of BT's crystallization which is illustrated in *Figure 2.11*. It can be found that higher temperature helps to form better crystallization since crystallization of BT is endothermic. Relative references indicate that the activation energy for BT crystallization under hydrothermal condition varies in the range from 21 to 105kJ/mol for the chemical reaction that proceeds on the liquid stage. Temperature's range from 120 to 250°C is widely used for the preparation. [128-132] Generally, higher temperature provides enough energy to stimulate the reaction. However, considering safety, temperatures over 200°C will not be tested in the experiments. Comparing the data with BT's standard pattern, we find that there are some little peaks which do not belong to BT but BaCO$_3$. BaCO$_3$ comes from some CO$_2$ dissolved in the water which also crystallizes with Ba(OH)$_2$. Luckily, the amount of BaCO$_3$ is tiny. Meanwhile, in the inset figure, curves for both temperatures have only one peak in the range from 40 to 50 degree, it means that the crystal phase of BT we obtained in this condition is cubic rather than tetragonal which has two peaks in this range. Hence, according to the XRD pattern, 200°C will be used for the followed experiments.
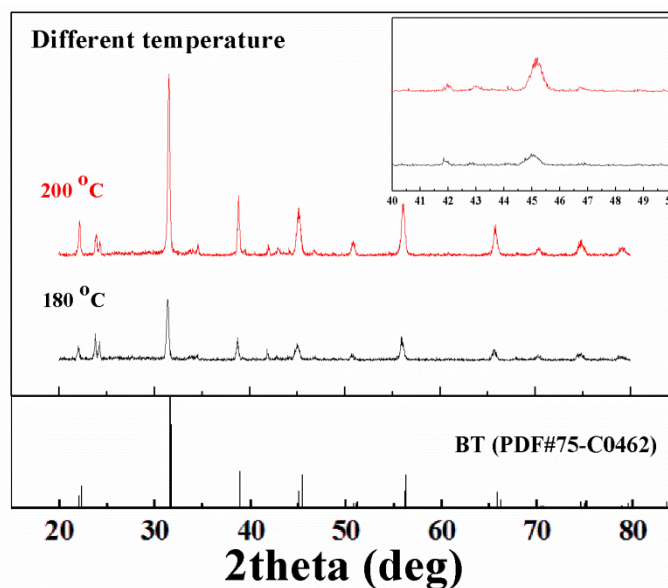
Figure 2.11 XRD of two temperatures for H-BT-CNT

Secondly, we will discuss the effect of reaction pressure. XRD results of three reaction pressures are shown in *Figure 2.12*. Hydrothermal reaction happens at $200^{o}C$ that is higher than water's boiling point under ambient condition ($100^{o}C$). Thus, water's volume in the reactors determines the pressure of reaction. It is easy to understand that when the volume of water is high, the large pressure will be achieved. Comparing three volumes of water in the XRD pattern shown in *Figure 2.11*, we find that in this system reaction pressure does not influence much on the crystallization and BT's crystal phase. The intensities of peaks are similar for three curves and all of them just have one peak in the inset graph. However, the volume of water is still important because more CO_2 will be brought in the system which influences negatively on BT's purity. Hence, 80% water content will be used for the following experiments.
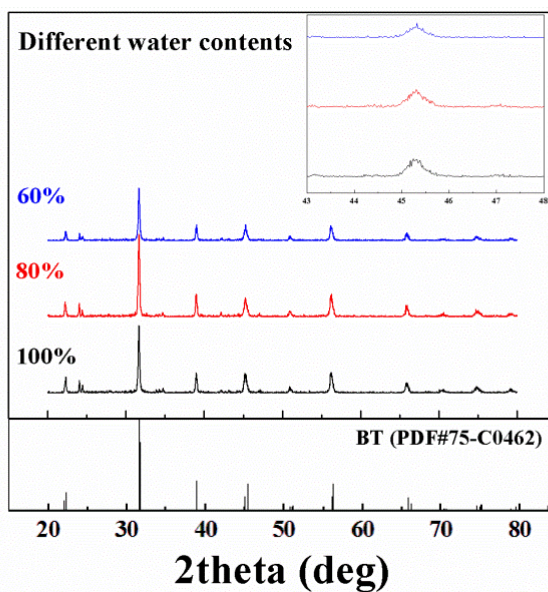
Figure 2.12 XRD for three water contents in hydrothermal reactor
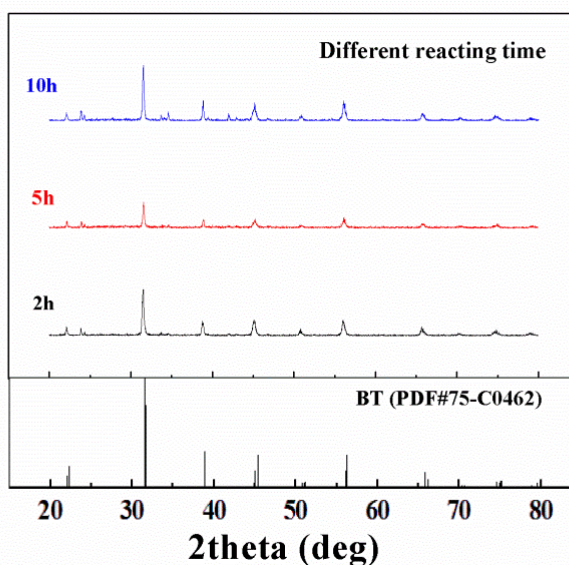
Figure 2.13 XRD of three reacting durations

Thirdly, reaction duration is also studied and we choose 2*h*, 5*h* and 10*h* for comparison. As XRD patterns illustrated in *Figure 2.13*, we find that reaction duration does not affect crystallization of BT much. As reaction duration prolonging, intensities of peaks in three curves do not change a lot. This means the process of BT's crystallization does not largely depend on reaction duration. Therefore, we will take BT's morphology at different reaction duration into consideration.

Before the discussion, it is necessary to study the chemical process of hydrothermal reaction. The crystallization via hydrothermal reaction obeys to dissolving-precipitation mechanism and it is mainly controlled by dissolving rate of reactant TiO_2. The presence of OH^- irons of Ba-OH bond is responsible for TiO_2's hydrolysis which acts as catalysts to accelerate the crystallization of BT via precipitation. [133]

$$BaOH^+(aq) + Ti(OH)_4^0(aq) \rightleftharpoons BaTiO_3(s) + 2H_2O + H^+(aq)$$
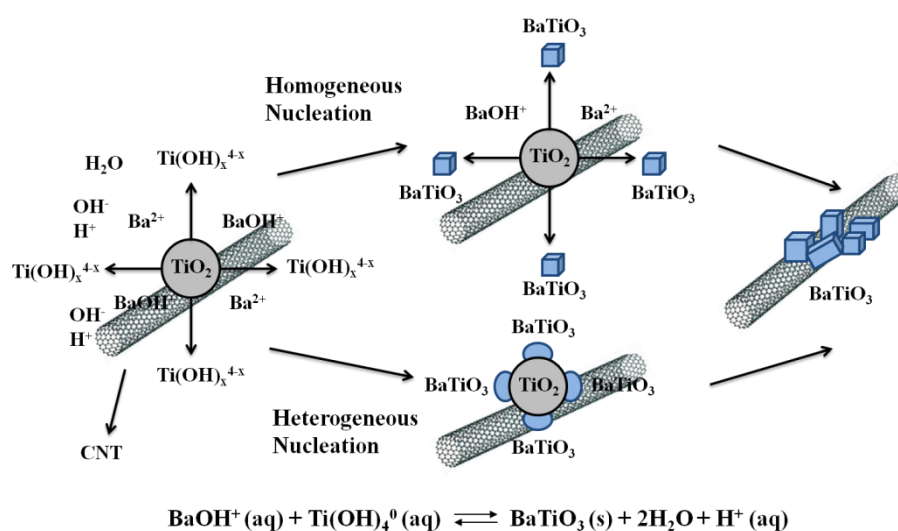
Figure 2.14 Schematic sketch of the dissolution/precipitation mechanism that conduces to the hydrothermal crystallization of BT coating on CNT

The whole crystallization process is illustrated in *Figure 2.14*. Firstly the solution is supersaturated due to dissolution of precursors. BT spontaneously starts to precipitate in this stage which yields an abundant numbers of nuclei for the crystallization. Thus, the dissolution of TiO_2 controls BT nucleation and growth in the early stage. The process of nucleation can be divided into homogeneous one and heterogeneous one. For the homogeneous nucleation shown in the upper part of scheme, Ti-O bonds of anhydrous TiO_2 precursor must be broken via hydrolytic attacking to hydroxyl-titanium complexes ($Ti(OH)_x^{4-x}$). Afterward, they are able to dissolute and react with barium ions or complexes (Ba^{2+} or $BaOH^+$) in the solution to precipitate BT. For the heterogeneous nucleation as shown in the beneath part of scheme, it often happens in the intermediate or final stage of reaction and largely

depends on the dissociation of remaining reactants. Differently with the homogeneous nucleation, in heterogeneous nucleation, TiO_2 particles act as precipitation sites of BT nuclei during their dissolving process. The aggregation and coarsening of BT usually happens in hydrothermal reaction due to Ostwald re-crystallization mechanism. Thus, both homogeneous and heterogeneous nucleations show that the reaction duration is responsible for BT's morphology. This process can be studied by STEM and EDS. Results of different reaction durations are shown in *Figure 2.15 (a)*, *(b)*, *(c)* respectively.

As illustrated in *Figure 2.15 (a)*, it is found that in the first 2*h*, BT particles have already formed and started to accumulate on CNT's surfaces. As reaction duration increasing, the accumulation of BT particles keeps increasing shown in *Figure 2.15 (b)*. Meanwhile, intensities of Ba and Ti's peaks of EDS in the right are sharper and higher compared with those for 2*h*. Furthermore, from STEM images of *Figure 2.15 (b)*, we find that BT particles not only accumulate on CNT's surface, but also agglomerate individually which means coarsening of BT particles has already started in the this stage. When reaction duration reaches 10*h* as the image shown in *Figure 2.15 (c)*, we observe agglomeration of BT particles is much more obvious. Thus, in order to have homogeneous BT's coating on CNT, coarsening process should be avoided as much as possible and 5*h* will be chosen for the experimental condition.

(a)

(b)

(c)
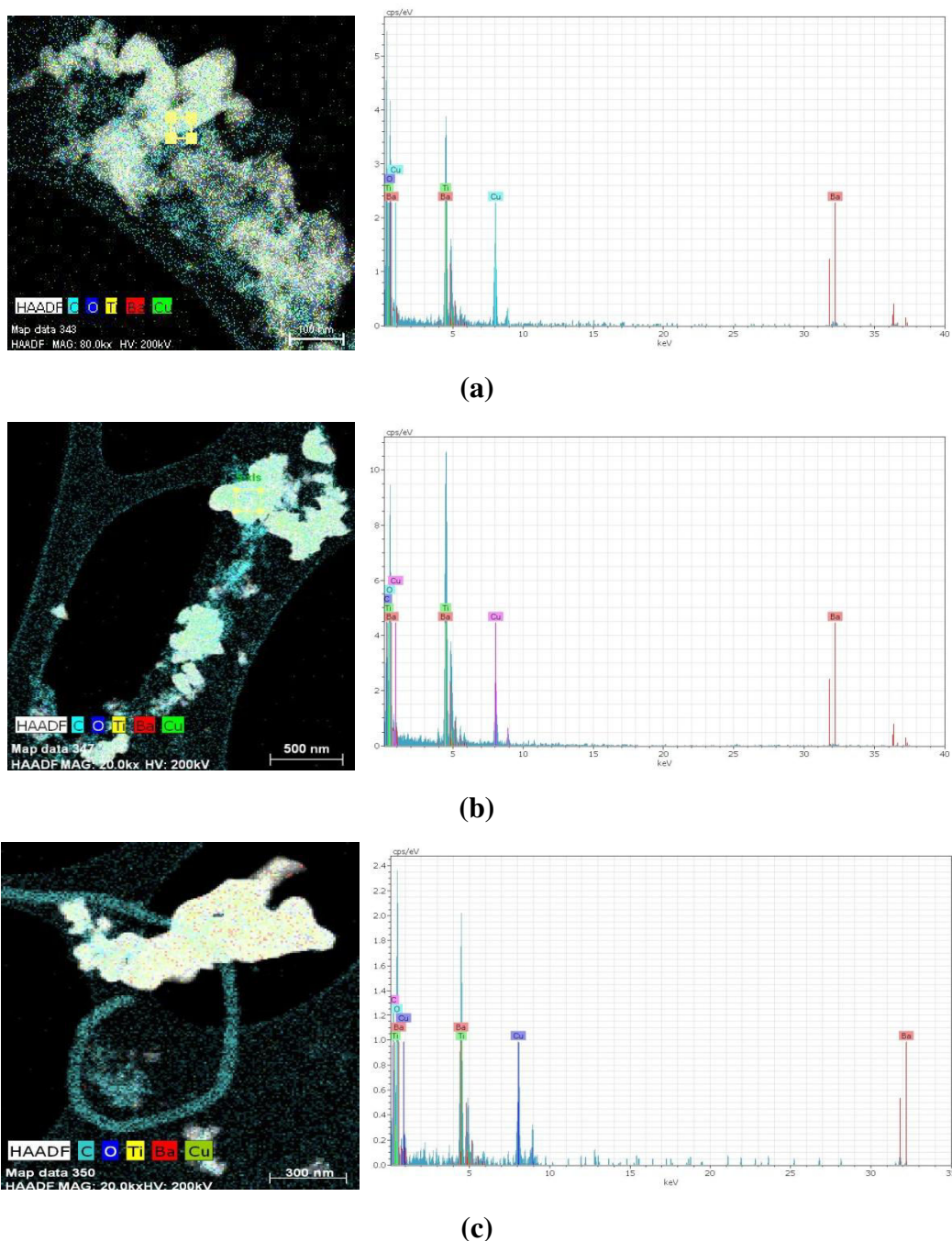
Figure 2.15 STEM and EDS for H-BT-CNT with different reaction times. **(a)** for 2*h*, **(b)** for 5*h* and **(c)** for 10*h*, respectively

2.5 Fabrication of polyvinylidene fluoride matrix composites

Composites are all fabricated by the combination of solution casting and extrusion-injection processing. Firstly, pre-calculated amount of fillers is disposed into DMF solvent by 30*min*'s ultrasonic dispersion. And then PVDF powder is added

into the mixture and stirring magnetically for $2h$ at 70^oC. The mixed fillers/PVDF solution is coated on a glass substrate by thermally treating at 70^oC for $2h$ in order to evaporate DMF. Afterwards, for further processing, the film of filler/PVDF is put into a co-rotating, conical, two-screw micro-extruder/compounder (Micro 5cc Twin Screw Compounder, DSM) and blends at 230^oC for $1h$ with the speed of $60rpm$ in Ar protection atmosphere. Slabs with the thickness of $1.45mm$ are fabricated via extrusion-injection (Micro 5cc Injection Molder, DSM, at $1.3MPa$ for $1min$). The temperatures of injection nozzle and mould holder are set at 240^oC and 60^oC, respectively. The scheme of extrusion-injection process is shown in *Figure 2.16*.
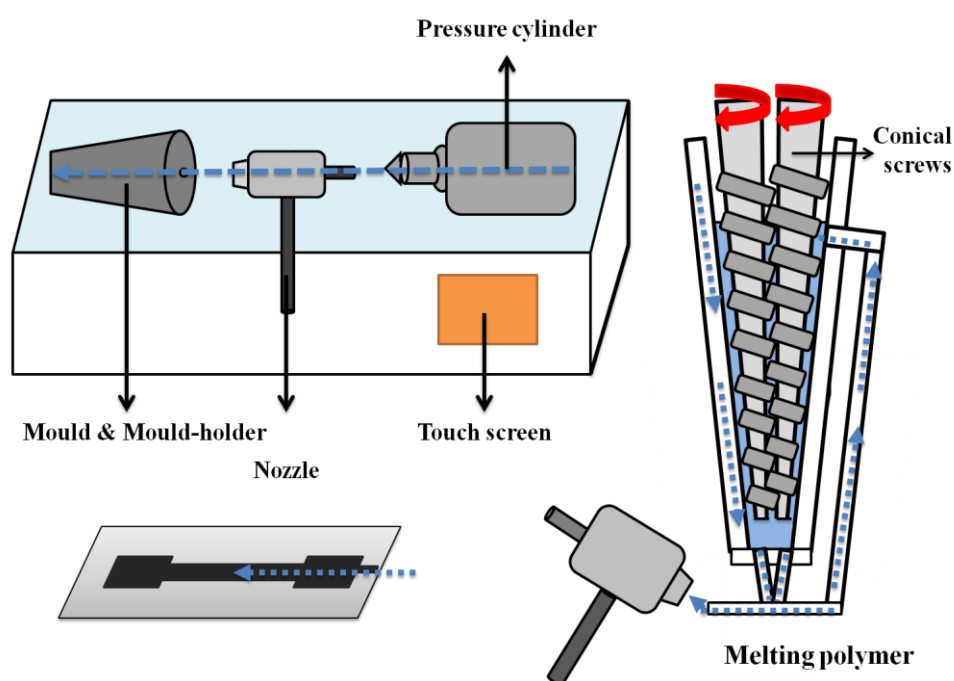
Figure 2.16 Scheme of the process for the H-CNT-BT/PVDF nanocomposite by extrusion-injection way

2.6 Partial conclusion

This chapter contains experimental and characterization works for the thesis. Firstly, H-CNT-BT has been produced with in situ grafting CNTs on the surface of BT by CVD. It is found that CNT's weight fraction and morphology are strongly

influenced by experimental conditions. According to the study, the weight ratio between BT particles and $Fe(NO_3)_3 \cdot 9H_2O$ are dominant to the growth of CNTs on BT particles and the ratio of 85:15 is the effective for synthesis. Then CVD reaction temperature also plays an important role on the morphology of H-CNT-BT. Over high temperature may impede CNT's growth due to thermal decomposition's property of acetylene. By comparing with morphologies of H-CNT-BT synthesized at different temperatures, we find 650^oC is a suitable temperature for CVD reaction in H-CNT-BT's system. Additionally, hydrogen flow rate in carrier gas is also studied for further improvement of CNT's quantity and we find that hydrogen flow rate of 0.1*l/min* is favorite for CNT's growth in this system.

Secondly, H-BT-CNT is prepared by two steps. In the case of coating TiO_2 on CNT by TBOT's hydrolysis, ammonia solution content and reaction duration affect TiO_2's conversion and morphology. A proper ammonia solution increases the conversion of TiO_2. Reasonable reaction duration is the key factor for controlling coating morphology in this step. We find that ammonia solution content of 0.3*ml* and reaction duration of 2*h* are favorable for TiO_2 coating. In the case of BT hydrothermal reaction, we find temperature is the key factor for BT's crystallization. Meanwhile, reaction duration is also important for final morphology of BT coating on CNT's surface. By the analysis of obtained experimental data, 200^oC and 5*h* are suitable for the hydrothermal reaction's condition. Additionally, obtained BT particles are cubic phase in H-BT-CNT system.

The processing of PVDF matrix composites and relative characterizations are also provided in this chapter. About dielectric property of composites, we will discuss in the next two chapters.

Chapter 3 Dielectric property of carbon nanotube-BaTiO₃

hybrids/polyvinylidene fluoride

_____

Introduction

In this chapter, we study performances of H-CNT-BT/PVDF composites with different volume fractions including morphology, thermal, dielectric and crystallization property. Meanwhile, a thermal treatment is conducted for comparing the change of dielectric behaviors. A significant increment in dielectric permittivity is observed after thermal treatment. Moreover, we find that the increment of dielectric permittivity after thermal treatment depends on filler's volume fraction and thermal treatment's parameters including annealing temperature, annealing duration, multi-cycle annealing and cooling rate. In order to study thermal treatment's effect on the dielectric property and understand comprehensively for the interfacial interaction between CNT in H-CNT-BT and PVDF, in-situ synchrotron X-ray is applied to detect the re-crystallization behavior of PVDF including crystalline polymorphs' transition and thickness's change of long period.

3.1 Dielectric property of composites before thermal treatment

3.1.1 Morphology analysis

(a)   (b)

(c)   (d)
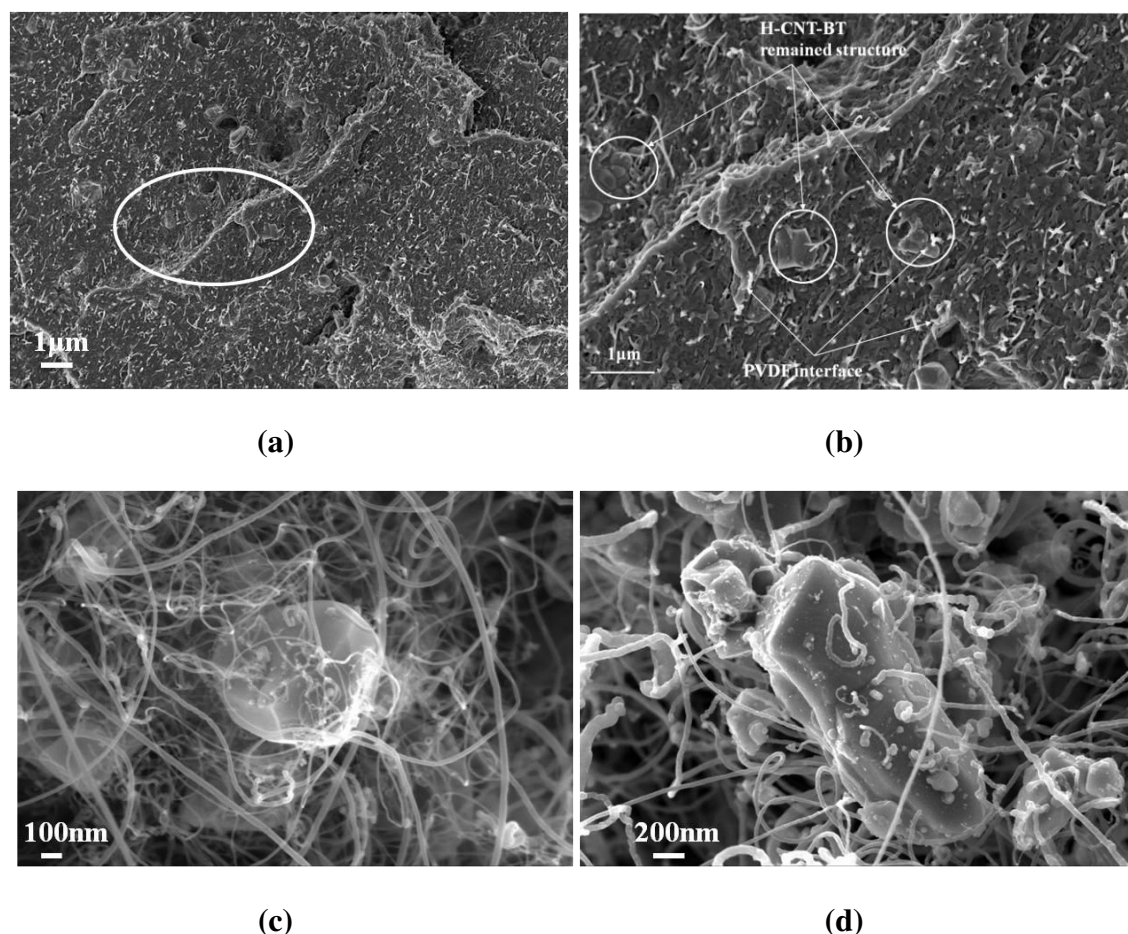
Figure 3.1 (a) SEM image of the fracture surface of H-CNT-BT/PVDF-10% (vol%) composite, **(b)** is an enlarging part of white circle shown in **(a)**. **(c)** and **(d)** are morphologies of H-CNT-BT before incorporated into PVDF

The SEM images of H-BT-CNT/PVDF-10%'s fracture surface (10% means the volume fraction of H-CNT-BT) is presented in *Figure 3.1(a)* and *(b)* is an enlarge one. We find that original structures of H-CNT-BT are partly destroyed compared with the images shown in *Figure 3.1 (c)* and *(d)*, respectively, but fortunately, there are still

some remained structures. Meanwhile, CNT and BT are dispersed in a relative homogeneous mode. This good dispersion may be attributed to H-CNT-BT's structure which arrays CNT in a special way before incorporated into PVDF rather than in an initial entangled state. The scheme in *Figure 3.2* helps us to understand this double dispersion of CNT in PVDF matrix.
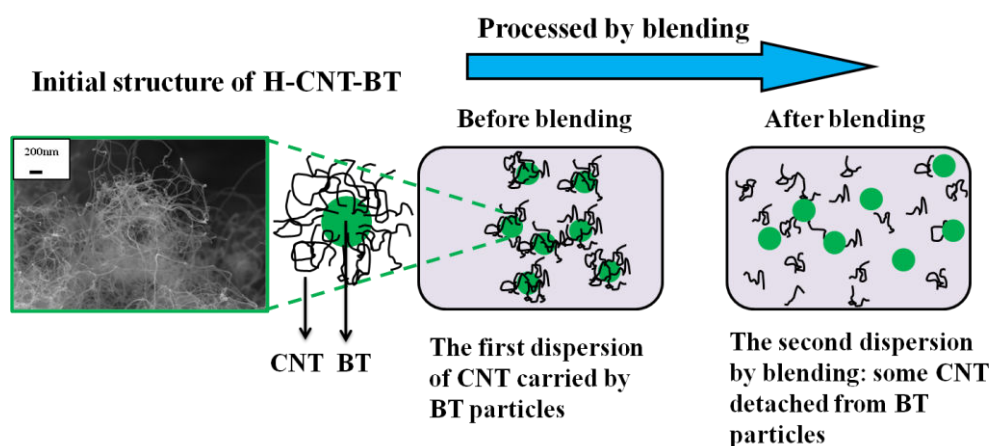
Figure 3.2 Scheme of double dispersion of H-CNT-BT in PVDF

Although original H-CNT-BT hybrid's structure is partly destroyed due to blending, the linkage between BT and CNT is not totally absent. Observing in *Figure 3.1 (b)*, we find that BTs and CNTs do not depart from each other by their individual agglomerations. Instead, they stay with each other in a compatible state. This compatible dispersal in PVDF provides more possibilities for potential collaborative effects between H-CNT-BT and PVDF. Furthermore, the addition of H-CNT-BT does not destroy PVDF matrix because no obvious voids and defects are observed in *Figure 3.1 (a)* and *(b)*. If comparing CNT's diameter in *Figure 3.1 (b)*, with *Figure 3.1 (c)* and *(d)*, it is easy to find that CNT's diameter of composite in *Figure 3.1 (b)* marked by white arrow is a bit bigger than that of H-CNT-BT in *Figure 3.1 (c)* and *(d)*. This indicates that blending way is able to create a PVDF interfacial layer wrapping around CNT. This polymer adhesion on CNT's surface provides the support for existence of micro-capacitor. The formation of micro-capacitor in the composite may induce a strong interfacial polarization under the applied field and consequently

greatly influences the dielectric property. This part we will discuss further in the following study.

3.1.2 Thermal analysis
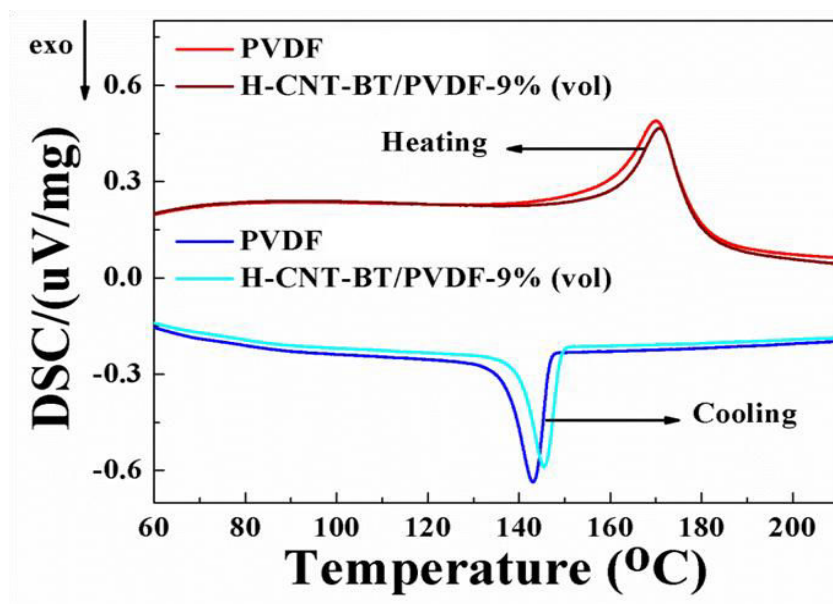
Figure 3.3 DSC for pure PVDF and H-CNT-BT/PVDF-9%

In order to study thermal properties of PVDF and H-CNT-BT/PVDF composite, DSC is conducted for them and results are shown in *Figure 3.3*. Firstly during the heating stage, melting points of PVDF and H-CNT-BT/PVDF-9% are 170.2^oC and 170.7^oC, respectively. During the cooling stage, crystallization's temperatures of PVDF and H-CNT-BT/PVDF-9% are 143^oC and 145^oC, respectively. It can be found that crystallization's temperature for H-CNT-BT/PVDF-9% is a bit higher than pure PVDF. It is caused by the addition of CNT that acts as nuclei for the rapid crystallization and promotes PVDF's crystallization. According to the reference, [116] it is generally believed that CNT in semi-crystalline polymers leads to a heterogeneous nucleation which is typically much faster than pure polymers. This effect on polymer crystallization will increase crystallization's temperature and nucleation's density while decrease crystallization's time. Therefore, crystallization's temperature of H-CNT-BT/PVDF-9% is a bit higher than pure PVDF due to the presence of CNT.

3.1.3 Dielectric property of composites with different volume fractions

Before analyzing dielectric properties of H-CNT-BT/PVDF composites, we provide concrete concentrations of each component including weight fractions and volume fractions for H-CNT-BT, CNT and BT, respectively in composites. They are shown in *table 3.1*. Herein, densities for BT, CNTs and PVDF used in the calculation are 6.02, 2.00 and 1.79 *g/cm³*, respectively.

Table 3.1 Concentrations of each component for H-BT-CNT/PVDF composite

H-CNT-BT (wt%)	*f_{H-CNT-BT} (vol%)*	*f_{BT} (vol%)*	*f_{CNT} (vol%)*
2.69	1	0.724	0.276
5.29	2	1.45	0.551
7.81	3	2.17	0.827
10.2	4	2.90	1.10
12.6	5	3.62	1.38
14.9	6	4.35	1.65
17.1	7	5.07	1.93
19.2	8	5.80	2.20
21.3	9	6.52	2.48
21.8	9.25	6.70	2.55
22.3	9.5	6.88	2.62
22.8	9.75	7.06	2.69
23.3	10	7.24	2.76
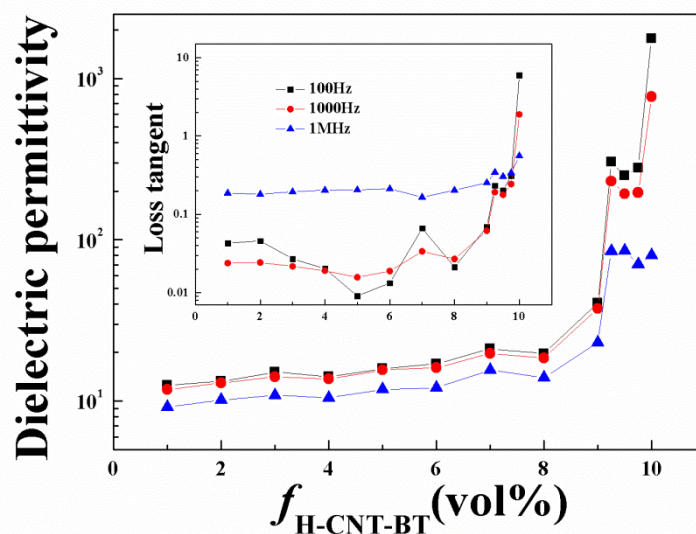
Figure 3.4 Dielectric permittivity (the large one) and dielectric loss (the insert one) of H-CNT-BT/PVDF composites as a function of $f_{H-CNT-BT}$, measured at 100, 1k, and 1MHz at room temperature.

The change of dielectric permittivity in H-CNT-BT/PVDF composites can be divided into two stages shown in *Figure 3.4*. Initially, in the first stage, when $f_{H-CNT-BT}$ is small ($f_{H-CNT-BT}<8\%$, $f_{CNT}<2.2\%$) and far away from percolative behavior, the conductive network is less effective to arouse the strong interfacial polarization. Thus, dielectric permittivity for H-CNT-BT/PVDF increases slightly compared with one of pure PVDF (10→22 at 100Hz). Meanwhile dielectric loss remains at a low lever (below 0.1 at 100Hz). Dielectric properties in this stage is as similar as most CNT reinforced PVDF composites with low f_{CNT}.

However, as $f_{H-BT-CNT}$ further increasing to the vicinity of percolation threshold f_c ($9\%<f_{H-CNT-BT}<10\%$, $2.2\%<f_{CNT}<2.76\%$) where we view it as the second stage, dielectric permittivity of H-CNT-BT/PVDF has a significant increment (for example: dielectric permittivity of H-CNT-BT/PVDF-9.25% is 304 at 100Hz). It is possibly attributed to the further shrinkage of inter distances between two CNTs as $f_{H-CNT-BT}$ increasing and the appearance of micro-capacitor near percolated behavior. But dielectric loss in this stage is still lower. This is owing to the existence of BT particles in H-CNT-BT and the thin PVDF layer at the interface of CNT we mentioned in SEM

images. The leakage current caused by percolative behavior is possibly blocked by both of them which leads to high dielectric permittivity but low loss tangent (<0.24). According to dielectric theory, Debye-type relaxation and leakage current are two factors for dielectric loss [3, 13]. In H-CNT-BT/PVDF, interfacial components of micro-capacitors are not only PVDF/CNT, but also BT/PVDF and BT/CNT. Even though the original structure of H-CNT-BT is partly lost during the procedure of processing, BTs and CNTs still have collaborative effects with each other, rather than separated in two individual agglomerations in PVDF. Although from the view of external-field effect, PVDF interfacial layer between neighboring CNTs may not strong enough to withstand the increasing local field, the existence of BTs may behave as a buffer to reduce short circuits occurring so that partial leakage current may be avoided. Therefore, high dielectric permittivity with low dielectric loss can be achieved via a special structure of H-CNT-BT.

Still in the second stage, when $f_{H\text{-}CNT\text{-}BT}$ is 9.5% (f_{CNT}=2.62%), a small decrement in dielectric permittivity appears compared with the case of $f_{H\text{-}CNT\text{-}BT}$=9.25%. This is typically percolative behavior and when $f_{H\text{-}CNT\text{-}BT}$=9.75%, dielectric permittivity increases dramatically again as well as dielectric loss. The maximum of dielectric permittivity and dielectric loss for the composite are as 1777 and 6 at 100Hz, respectively when $f_{H\text{-}CNT\text{-}BT}$ is 10%. It is worthy to mention that this high dielectric permittivity while low dielectric loss near percolated behavior is rarely seen compared with most CNT/PVDF composites. It is because an extremely low f_{CNT} (2.76%) of H-CNT-BT/PVDF is used near percolative behavior while in the case of CNT/PVDF, CNT's volume fraction is usually over than 9% for percolation threshold.

3.2 Dielectric property of composites after thermal treatment

3.2.2 Effect of volume fractions of carbon nanotube-BaTiO₃ hybrids

We compare dielectric permittivity for H-CNT-BT/PVDF composites from 0% to 10% between before and after thermal treatment. Herein, the annealing temperature is 150°C and the duration is 30min. The values of dielectric permittivity at 100Hz and

1MHz are shown in *table 3.2*.

Table 3.2 Dielectric permittivity's change of composites with different $f_{H\text{-}CNT\text{-}BT}$ between before and after annealing-cooling treatment

$f_{H\text{-}CNT\text{-}BT}$ %	ε'@100Hz		ε'@1MHz	
	Before	**After**	**Before**	**After**
0	14.8	12.7	12.4	10.7
1%	13.7	12.5	11.0	10.5
2%	15.5	14.3	11.1	10.5
3%	17.9	16.9	12.6	12.2
4%	16.3	15.6	12.1	11.9
5%	19.3	17.4	13.5	13.3
6%	20.6	19.4	14.6	14.6
7%	24.2	23.0	17.2	17.0
8%	24.2	22.5	16.6	17.3
9%	56.4	123.8	31.9	67.4
9.25%	304.2	1040.1	84.7	202.9
9.5%	250.1	851.5	85.5	209.9
9.75%	279.4	1111.5	70.2	140.7
10%	3732.4	7600.6	101.7	470.4

If we pay attention to the data of two frequencies' dielectric permittivity at the same volume fraction, we find that data in *table 3.2* can also be divided into two stages. The first stage is lower $f_{H\text{-}CNT\text{-}BT}$ (from 0 to 8%) and in this stage, neither at 100Hz nor at 1MHz, dielectric permittivity increases after thermal treatment. On the contrary, it decreases a little. But as $f_{H\text{-}CNT\text{-}BT}$ increasing gradually, this difference gradually becomes small. It is known that the composite processed by extrusion-injection way usually suffers the inhomogeneous dispersal of fillers in composites especially for composites incorporated with fibers with large aspect ratios like CNT. [134-136] During the injection procedure, the sample is pushed into a mold by large pressure and fast speed from higher temperature (240^oC) to lower temperature (60^oC). Both PVDF and CNT may be oriented toward the machine direction due to the shear of mold's surface which arrays dipoles regularly and promotes polarization. However, a thermal treatment will partly destroy dipoles' orientation so that causes a slight decrement in dielectric permittivity. Moreover, thought thermal treatment may

change CNT's network but it is not effective enough for inducing tunneling effect since in this stage, $f_{H-CNT-BT}$ is far away from the percolated threshold. Hence, even thought the change of conductive network may cause the shrinkage of neighboring CNTs' distances, original low $f_{H-CNT-BT}$ still fails to improve the dielectric property after thermal treatment.

However, in the second stage, when $f_{H-CNT-BT}$ is over than 9%, dielectric permittivity after thermal treatment has a significant increment. Meanwhile, this increment has been remained after the sample cooling down to the room temperature which means that the change of conductive network is irreversible. The thermal treatment promotes a further connection of conductive network especially near percolated behavior which may arouse strong interfacial polarization and then increase dielectric permittivity. Hence, this volume fractions' dependence shows that the increment of dielectric permittivity after thermal treatment is highly associated with percolative behavior. In order to study more about the effect of thermal treatment on sample's dielectric property near percolation threshold, different parameters including annealing temperatures, annealing durations, multi-cycle's annealing and cooling rates are investigated and discussed in the following parts.

3.2.2 Effect of annealing temperature
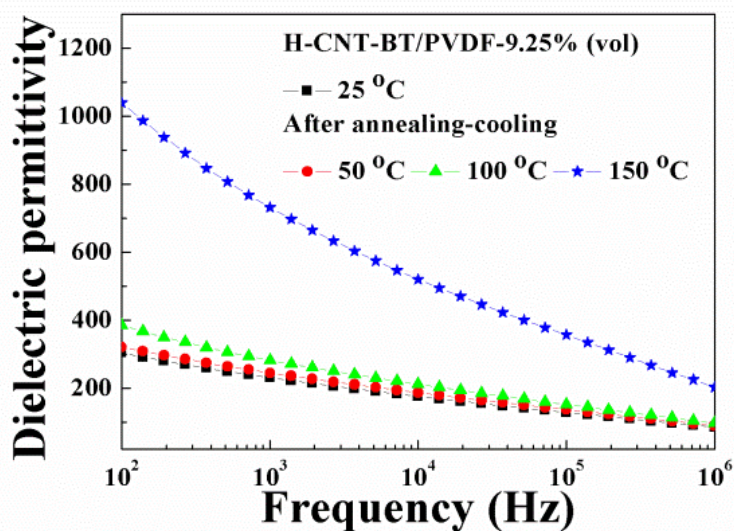
(a)
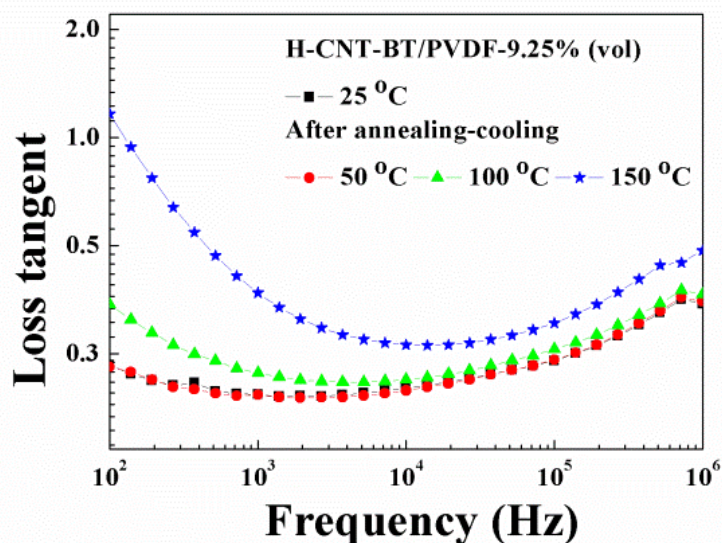
(b)

Figure 3.5 Frequency dependence of dielectric properties for H-CNT-BT/PVDF-9.25% of before and after anneal at different temperatures **(a)** for dielectric permittivity and **(b)** for loss tangent, respectively

H-CNT-BT/PVDF-9.25% is conducted at three annealing temperatures: 50, 100 and 150°C, respectively and results are shown in *Figure 3.5*. Firstly, in *Figure 3.5 (a)*,

we find that dielectric permittivity increases as annealing temperature increasing. Especially after annealed at 150^oC, dielectric permittivity displays a notable enhancement (three times larger than that of before). Generally in the case of conductive-dielectric composite, its dielectric property mainly depends on conductive network. Thus it is possible that CNT network's change and consequently the shrinkage of distance between neighboring CNTs after thermal treatment results in the increment of dielectric permittivity. Meanwhile, we notice that if temperature is lower than 150^oC, the increment in dielectric permittivity is not very obvious. This phenomenon makes us to consider the thermal property of H-CNT-BT/PVDF composite. The result in DSC shows that 150^oC is similar to crystallization's temperature of the composite. Thus, annealing at this temperature for 30*min* may induce some PVDF's crystalline melting. The change of CNT's network may happen in this re-crystallization of PVDF procedure. Additionally, if we observe frequency dependence of dielectric loss in *Figure 3.5 (b)*, after thermal treatment, the loss tangent increases a little but still remains at a low level (<1.5 at 100*Hz*). This infers that annealing at 150^oC does not change CNT's network thoroughly since low dielectric loss is still from Debye-type relaxation.

3.2.3 The change of neighboring CNTs' distance after thermal treatment

The electrical conduction of a CNT/PVDF composite is primarily governed by the tunneling of electrons through gaps between neighboring CNTs, instead of conduction through intimate CNTs contacting. [13] The dielectric permittivity's increment caused by thermal treatment is probably due to the change of neighboring CNTs' distance. Hence, we will use the theory of tunneling effect and models including series and parallel to estimate distance's change between neighboring CNTs after thermal treatment.
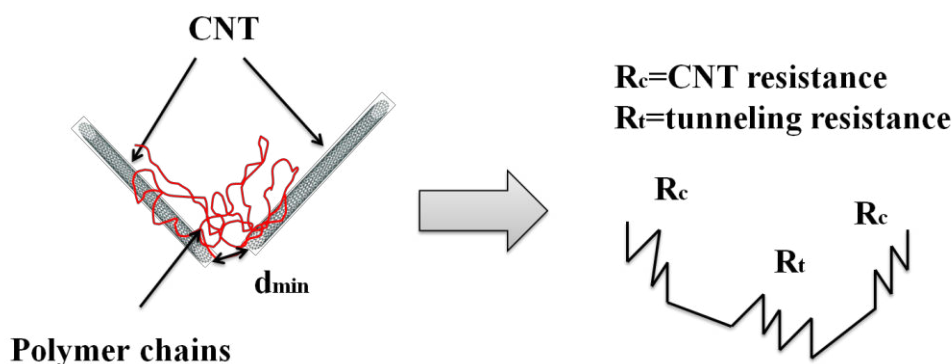
Figure 3.6 A CNT's pair with a tunneling gap between them

The scheme in *Figure 3.6* shows a typical two-dimensional sample space with two randomly generated CNTs. Since the tunneling effect of H-CNT-BT/PVDF is mainly caused by CNT, we will analog the model of CNT/PVDF composite for calculation. [137-143] The resistance of H-CNT-BT/PVDF composite can be roughly considered as CNT-PVDF's resistance since PVDF interface is effective micro-capacitor layer wrapped outside CNT which is observed by SEM. BT particles favor to promote a good dispersion of CNT in PVDF matrix, but they affect less for the tunneling effect. The tunneling resistance and tunneling conductivity between neighboring CNTs can be approximated by

$$R_t = \frac{\alpha}{A} \cdot d \cdot \exp(\beta \cdot d)$$

$$\alpha = \frac{h^2}{e^2 \cdot \sqrt{2m\lambda}} \qquad \beta = \frac{4\pi}{h} \sqrt{2m\lambda}$$

where *m* is the mass of an electron, *e* is the elementary charge, *h* is Planck's constant, *d* is the distance between CNTs, *A* is the cross-sectional area of the junction and *λ* is the tunneling energy barrier height (PVDF is 0.3*eV*), [145] respectively. If we use conductivity (σ_t) to estimate, the equation will change into:

$$\frac{1}{\sigma_t} = \alpha \cdot \exp(\beta \cdot d)$$

Usually DC conductivity is used for the calculation, but what we have tested by solartron is the AC impedance. According to related theory, the impedance can be expressed as:

$$Z = R + \frac{1}{S \cdot C}$$

where Z is the impedance, S is the parameter of frequency, R is resistance and C is capacitor, respectively. If we consider the situation at high frequency, Z can be viewed as the R since $\frac{1}{s \cdot c}$ is close to 0. Therefore, in the case of H-CNT-BT/PVDF-9.25%, we will use the Z' at 1MHz as the conductivity for the estimation of neighboring CNTs' distance in PVDF. [146]

In the case of H-CNT-BT, the conductivity is made by two parts which is also illustrated in *Figure 3.6* on the right: one is CNT's conductivity and the other is the conductivity of tunneling effect in the effective distance. We use the series model for the conductivity of H-CNT-BT.

$$\sigma_{H-CNT-BT} = [\frac{1 - \varphi}{\sigma_t} + \frac{\varphi}{\sigma_{CNT}}]^{-1}$$

Where $\sigma_{H\text{-}CNT\text{-}BT}$ is the conductivity of H-CNT-BT, σ_t is the tunneling conductivity and σ_{CNT} is the conductivity of CNT ($10^4 S/m$), respectively. φ is the ratio of R_{CNT} and R_t (2/3 is used for the calculation).

Similarly, in the case of H-CNT-BT/PVDF, the conductivity is also made of two parts: one is the conductivity of H-CNT-BT and the other is conductivity of PVDF. We use three models for the estimation. They are series, parallel and the effective medium theory (EMT) models, respectively. Among the three models, the parallel and series model are the simplest for two-phase systems and they are often used as upper and lower bounds for effective conductivity of two-phase heterogonous materials. EMT model tackles materials with a completely random distribution of all the components. The expressions of three models and calculating results are shown in *Figure 3.7* and *Figure 3.8*, respectively.

Series model

$$\sigma_e = [\frac{1-\phi}{\sigma_1} + \frac{\phi}{\sigma_2}]^{-1}$$

Parallel model

$$\sigma_e = (1-\phi)\sigma_1 + \phi\sigma_2$$

EMT model

$$(1-\phi)\frac{\sigma_1-\sigma_e}{\sigma_1+2\sigma_e} + \phi\frac{\sigma_2-\sigma_e}{\sigma_2+2\sigma_e} = 0$$
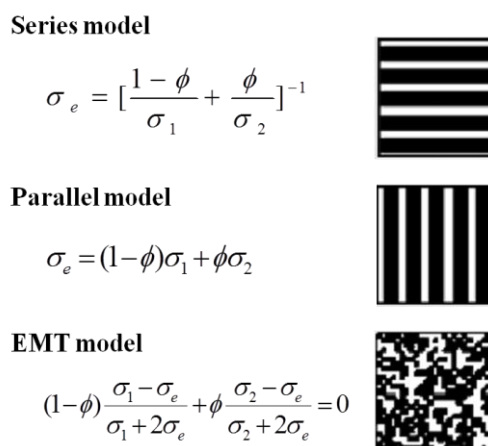
Figure 3.7 Assuming the electric field conducting in a vertical direction. Where σ_1 is the conductivity of PVDF, σ_2 is the conductivity of H-CNT-BT and σ_e is the conductivity of the composite. φ is the volume fraction of CNT, respectively.[9]
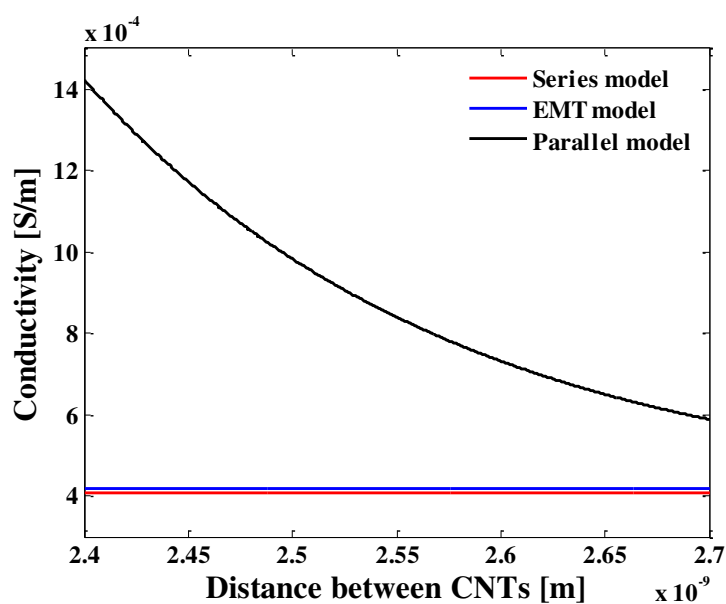
Figure 3.8 Calculations for distances between neighboring CNTs by three models

As shown in *Figure 3.8*, we can find neither series model nor EMT is suitable for the calculation since both of then fail to show the distance dependence of conductivity in the range of measurement. On the contrary, parallel model is able to show the distance dependence in this range. Therefore, we use parallel model for composite's conductivity.

Table 3.3 Impedance (Z), resistivity (ρ) and conductivity (σ) of before and after annealing at 50, 100 and 150°C for 30*min*, and then cooling naturally.

| $T(°C)$	Z'@1MHz	ρ	σ	$d(\text{Å})$
25	$1.31×10^4$	$2.01×10^2$	$4.99×10^{-3}$	22.3
50	$1.23×10^4$	$1.89×10^2$	$5.30×10^{-3}$	22.2
100	$1.13×10^4$	$1.73×10^2$	$5.77×10^{-3}$	22.0
150	$5.19×10^3$	79.7	$1.25×10^{-2}$	20.6
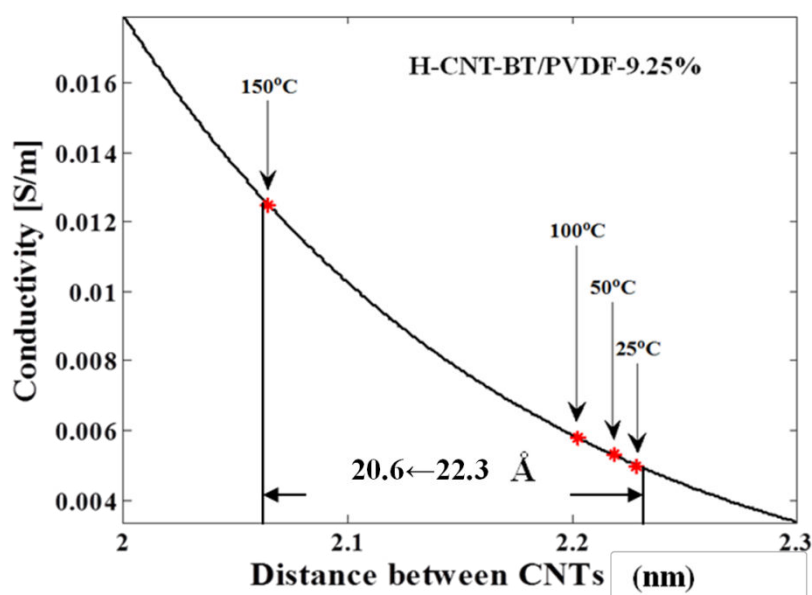
Figure 3.9 Results of calculation by parallel model

The results of calculation are listed in *table 3.3* and *Figure 3.9*, respectively. We find that after annealing at 50 and 100°C, a decrement in the distance between neighboring CNTs happens but the value is too small to induce the large increment of dielectric permittivity. After annealing at 150°C, the value decreases from 22.6 to 20.7Å that induces tunneling effect and consequently causes a significant increment in dielectric permittivity. If we compare data before and after thermal treatment at 150°C, we can find that the decrement in distances is around 2Å. This decrement is an average value since we do not consider complicated situations including overlapping area at the CNT-CNT junction, CNT's diameter, the thickness of PVDF layer between adjacent CNTs and BT's influence. This is just the simplest estimation according to

measurement results. Thus, as we mention before, only the distance between neighboring CNTs is close enough, the effective change of conductive network will induce tunneling effect and then improve dielectric permittivity after thermal treatment. In order to study more comprehensively about the effect of thermal treatment on dielectric property, we will come back to experimental works and consider more factors involving annealing duration, multi-cycle annealing and cooling rates.

3.2.4 Effect of annealing duration

In order to study the effect of annealing duration, we choose H-CNT-BT/PVDF-9.5% as the sample which is closed to f_c. The condition of the thermal treatment is annealing at 150^oC for 15, 30, 60, 90 and 120min, respectively, and then cooling naturally to the room temperature. The results are shown in *table 3.4*, *Figure 3.10 (a)* and *(b)*, respectively.

Table 3.4 Dielectric property's contrast of H-CNT-BT/PVDF-9.5% of before and after five annealing durations

H-CNT-BT/PVDF-9.5%	$tan\delta$@100Hz	ε' @100Hz	$tan\delta$@1MHz	ε' @1MHz
Before	0.21	258	0.32	71
After 15min	0.32	776	0.48	144
After 30min	0.42	1015	0.45	180
After 60min	0.49	1117	0.46	192
After 90min	0.51	1140	0.46	197
After 120min	0.55	1172	0.47	199
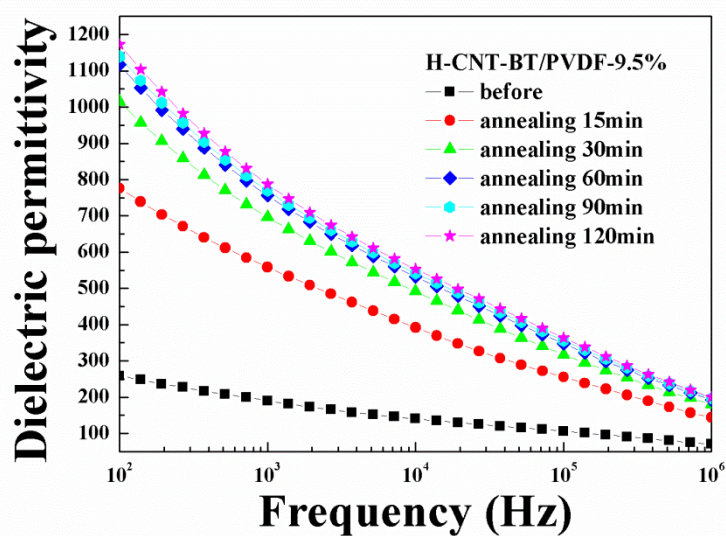
(a)
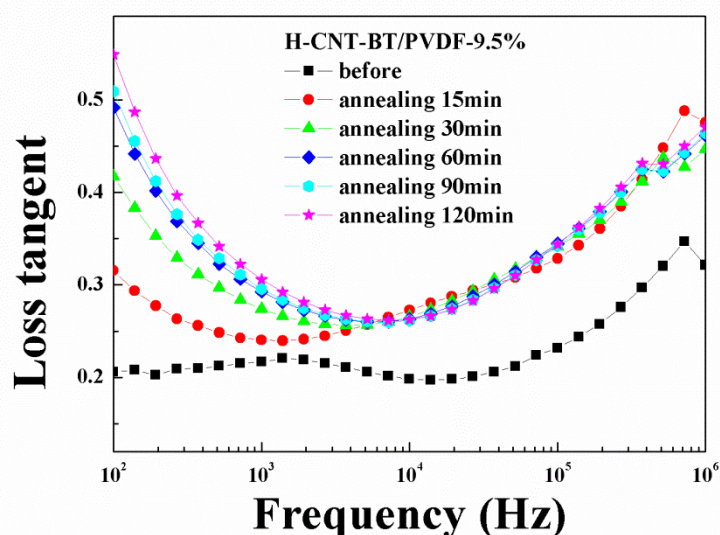
(b)

Figure 3.10 Dielectric property's comparison in different annealing durations for H-CNT-BT/PVDF-9.5%: **(a)** for dielectric permittivity, **(b)** for loss tangent, respectively.

As shown in *Figure 3.10* and *table 3.4*, we find that after 15*min*'s annealing, dielectric permittivity of H-CNT-BT/PVDF-9.5% at 100*Hz* has increased around three times than the before one (258.4→776.1). Moreover, as annealing duration increasing further, dielectric permittivity will reach over 1000. Afterwards, when the duration is

over 60*min*, dielectric permittivity becomes stable and increases just a little as duration prolonging to 120*min*. But during the whole process, dielectric loss always keeps at a low level (less than 0.6 at 100*Hz*). This property is really rare in the conductor-dielectric composites. There are some reasons for the significant improvement in dielectric performance after thermal treatment. Firstly, in the case of the dielectric permittivity's increment, the change of CNT's conductive network is forming better as annealing duration prolonging so that more interfacial polarization may be aroused at low frequency. However, this change of CNT's network is a kind of dynamic equilibrium and finally, it will become stable as the annealing duration is enough long. Thus, the change of CNT's conductive network is a kinetic and time-consuming process.

Secondly, in the case of dielectric loss, the low loss tangent shown in *Figure 3.10 (b)* infers that CNT clusters are dispersed in PVDF and they are still isolated to each other by the PVDF interfacial layer which infers that dielectric loss still partly stems from the Debye-relaxation after thermal treatment. According to Debye model description, it assumes that the identical reorienting dipoles are non-interacting and the distribution of relaxation times is affected by independently reorienting dipoles instead of thoroughly interfacial polarization between hybrids and matrix. [147] Low loss tangent near the percolation threshold is possibly attributed to the special structure of H-CNT-BT hybrids and the interaction between CNT and BT in PVDF's matrix. The special structure promotes the dispersion of CNT and releases high dielectric loss caused by interfacial polarization after thermal treatment. Hence, the results of annealing duration infer that the change of conductive network is a dynamic process and thermal treatment will promote the conductive network to become stable finally. But the factor that judges whether composites finally reaching the percolative behavior or not mainly depends on the original volume fraction of CNT. A thermal treatment may only promotes and stabilizes formed conductive network instead of directly reducing percolation threshold or changing the conductive network in a thorough mode.

3.2.5 Effect of multi-cycle annealing

A multi-cycle thermal treatment on H-CNT-BT/PVDF-9.5% is conducted for studying the change of conductive network, too. The condition of the thermal treatment for each cycle is annealing at $150^{o}C$ for $30min$ and then cooling naturally.
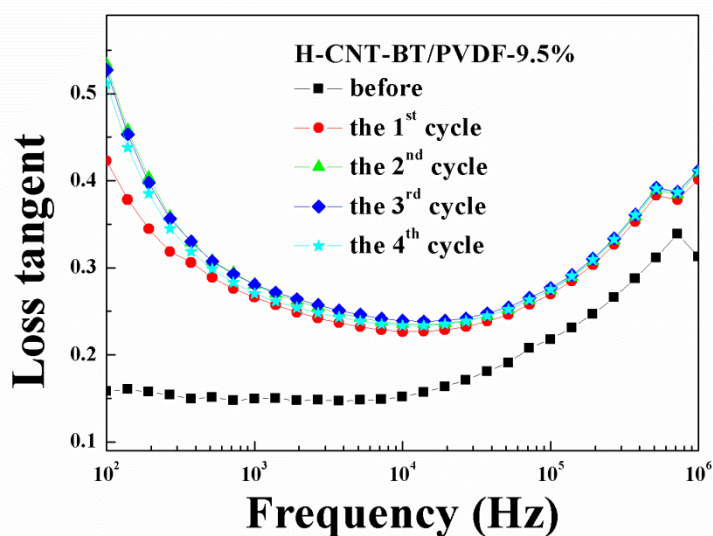
(a)
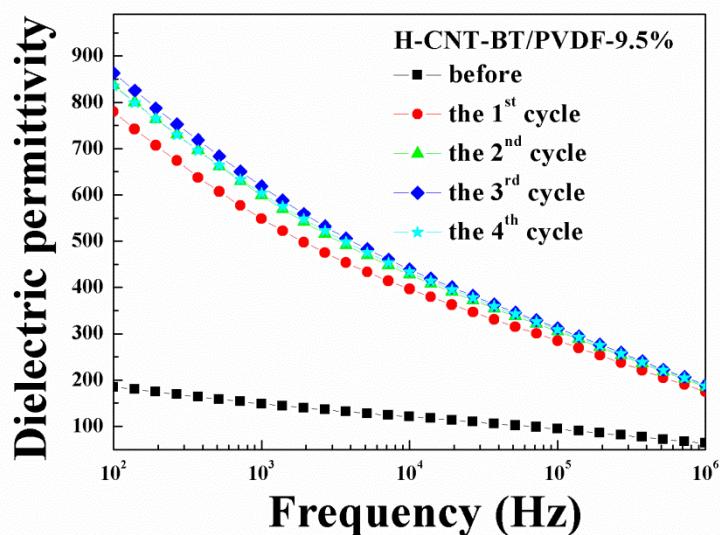
(b)

Figure 3.11 Frequency dependence of dielectric property of H-CNT-BT/PVDF-9.5% for multi-cycle thermal treatment, **(a)** for dielectric loss, **(b)** for dielectric permittivity, respectively.

Table 3.5 Dielectric property for H-CNT-BT/PVDF-9.5% of before and after multi-cycle annealing

H-CNT-BT/PVDF-9.5%	$tan\delta$@100Hz	ε'@100Hz	$tan\delta$@1MHz	ε'@1MHz
Before	0.16	184.9	0.31	63.9
The 1st cycle	0.42	780.2	0.40	174.7
The 2nd cycle	0.53	837.4	0.41	185.5
The 3rd cycle	0.53	863.1	0.41	189.2
The 4th cycle	0.51	835.4	0.41	187.3

As shown in *Figure 3.11* and *table 3.5*, we find that similarly as the case of increasing annealing duration, dielectric permittivity increases a lot after the first cycle annealing (185→780 at 100Hz, and 64→175 at 1MHz). Afterwards, after multi-cycle annealing, dielectric property is gradually stable and does not change too much (around 840 at 100Hz and 188 at 1MHz). Dielectric loss in the whole process keeps at a low level which is less than 0.53 at 100Hz and 0.42 at 1MHz. These results also prove that CNT network's change needs time and it can be viewed as a kinetic process. Actually, the effect of multi-cycle annealing for the conductive network can be analogized with prolonging annealing duration. As mentioned before, an inhomogeneous dispersion of H-CNT-BT in composites affects the change of conductive network. Meanwhile, CNT conductive network is really sensitive near the percolation threshold. Thus, a thermal treatment is able to release the conductive network's sensitivity to external stimulations. After a favorite thermal treatment, the dielectric property of composites will become more stable and higher.

3.2.6 Effect of cooling rates

The effect of thermal treatment's cooling rates on the dielectric property is also studied in this part. We compare two cooling rates for H-CNT-BT/PVDF-9.25% after annealing at 150°C for 30min: one is cooling naturally (to room temperature) as we used before and the other is quenching into the ice water.
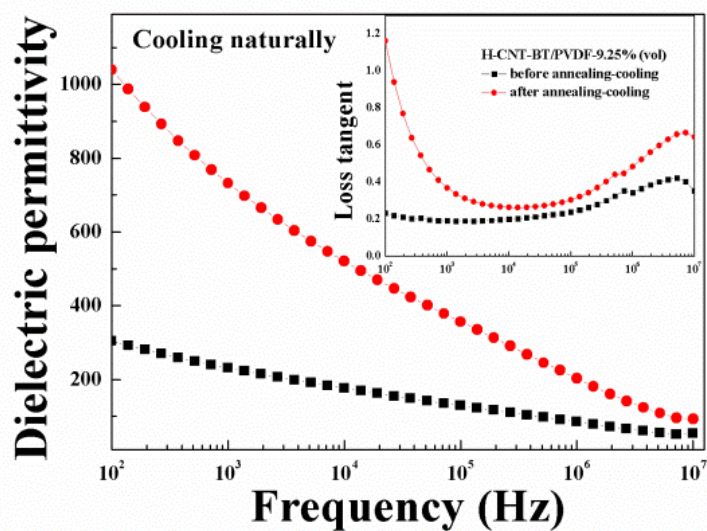
(a)
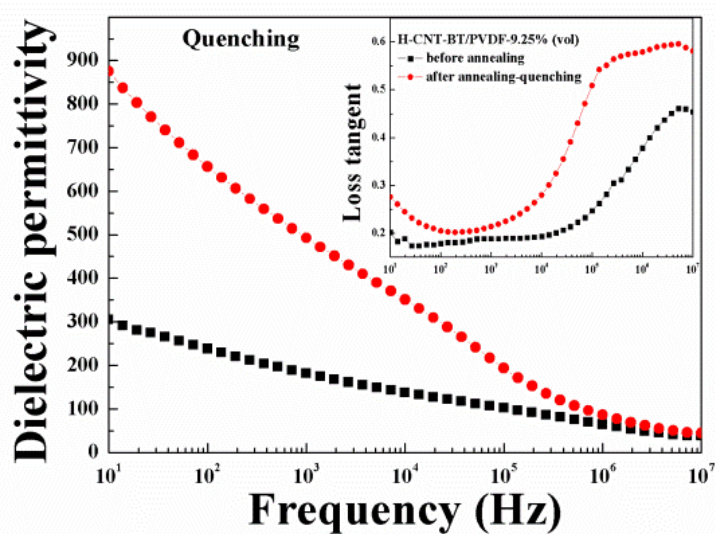
(b)

Figure 3.12 Dielectric properties of H-CNT-BT/PVDF-9.25% between before and after thermal treatment by two cooling rates. The large graph is frequency dependence of dielectric permittivity and the inset one is frequency dependence of loss tangent. **(a)** for the natural cooling, **(b)** for the quenching, respectively.

Table 3.6 Dielectric property for H-CNT-BT/PVDF-9.25% of before and after thermal treatment with different cooling rates

H-CNT-BT/PVDF-9.25%	*tanδ@100Hz*	*ε'@100Hz*	*tanδ@1MHz*	*ε'@1MHz*
Before	0.23	304	0.34	85
Cooling naturally	1.16	1040	0.48	203
Increasing rate	404%	242%	41%	139%
Before	0.18	238	0.38	64
Quenching	0.21	656	0.58	86
Increasing rate	16.7%	176%	52.6%	34.3%

Before the discussion, we have to mention again that the sample processed by extrusion-injection is inhomogeneous and CNT's dispersion differs from part to part even in the same slab due to the migration and orientation of CNT under flow during the procedure of injection molding. Thus, data in dielectric property of two samples before thermal treatment are not exactly same. It is a common problem that is widely studied and discussed especially in the field of fibers reinforced polymer matrix composite processing. [67-69] We will discuss about this point more concretely in chapter 4. Although the original data are not same, what we want to compare is the relative increasing rate in dielectric properties after thermal treatment.

Firstly as illustrated in *Figure 3.12* and *table 3.6*, we find that data of dielectric permittivity and dielectric loss increase a lot for both naturally cooling and quenching after thermal treatment. But increasing rates are different from each other and the peak in the graph of frequency dependence of loss tangent also has a shift between two cooling ways. The increment in dielectric permittivity and dielectric loss of cooling naturally is far higher than those cooling by quenching. It also supports that the change of CNT's conductive network needs time. Furthermore, that the loss tangent's peak of cooling naturally shifts to higher frequency means the thermal treatment may change the crystalline property of PVDF. As we mentioned before, dielectric permittivity's increment may be attributed to not only changes of CNT's

network but also PVDF's re-crystallization behavior. Since annealing temperature is very close to the crystallization temperature, some changes may occur in the process of re-crystallization of PVDF after the thermal treatment which may contribute to the increment of dielectric property.

3.3 In-situ simultaneous synchrotron X-ray characterization

In-situ simultaneous synchrotron wide-angle X-ray diffraction (WAXD) and small-angle X-ray scattering (SAXS) measurements are conducted to investigate the transition of crystalline polymorphs and the thickness change of PVDF's long period. The three categories that describe most synchrotron X-ray experiments are: X-ray scattering, X-ray spectroscopy and X-ray imaging. [148] By analysis obtained data, crystalline behavior of PVDF will be well studied which provides more information to understand thermal treatment's influence on H-CNT-BT/PVDF's dielectric property.

3.3.1 Wide-angle X-ray diffraction for polyvinylidene fluoride
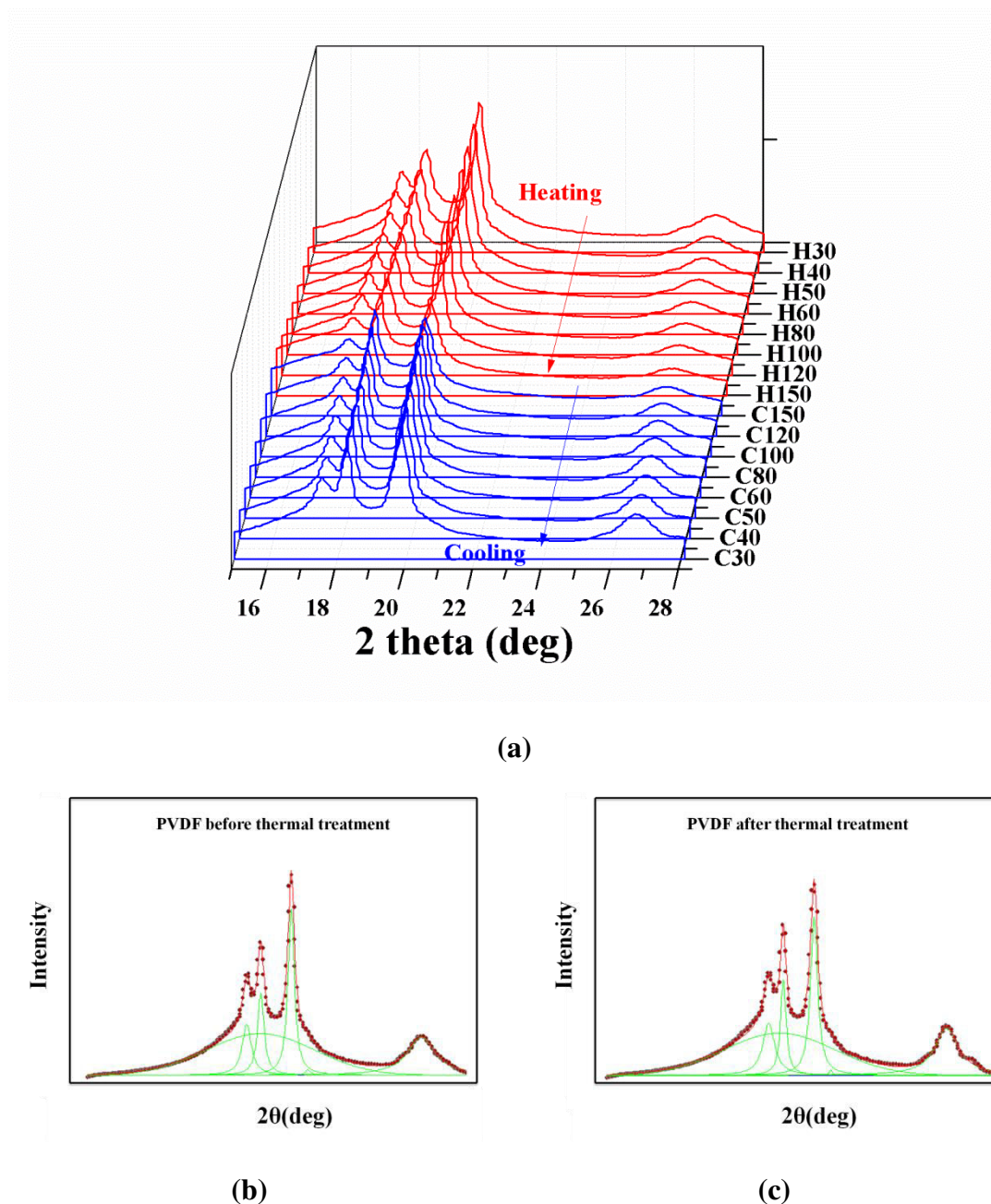

(a)

(b)   (c)

Figure 3.13 (a) WAXD for PVDF measured at different temperatures; **(b)** and **(c)** are profile analysis of diffractometer scans for before and after thermal treatment, respectively.

Table 3.7 X_c% and β% at different temperatures for PVDF calculated by the results of temperature dependence of WAXD

Temperature (^oC)	X_c%	β%
30	51.5%	0.92%
40	50.1%	0.64%
50	48.3%	0.33%
60	46.8%	0.29%
80	46.1%	0.11%
100	40.5%	
120	37.3%	
150	35.2%	
Annealing at 150^oC for 30*min*		
150	31.6%	
120	40.7%	
100	43.1%	
80	46.5%	0.25%
60	44.9%	0.27%
50	48.0%	0.32%
40	47.2%	0.51%
30	52.5%	0.49%

Temperature resolving WAXD experiments are conducted for PVDF. Results are shown in *Figure 3.13 (a)*, the fitting results of before and after thermal treatment are shown in *Figure 3.13 (b)* and *(c)*, respectively. In order to derive quantitative information related to material's microstructure such as the crystalline fraction or different crystalline polymorphs within the material, peak fitting procedure is followed. [149] Gaussian peak is assigned for the amorphous hallow, while Lorentz peak is assigned for crystalline polymorph by Origin's fitting routines. The calculation of the crystalline (X_c) and β polymorph fraction are determined according to Murthy's

methods. [149]

$$X_c\% = \frac{I_c}{I_c + I_a} \cdot 100$$

where I_c is the intensity for all crystalline diffraction peaks and I_a is the intensity for the amorphous halo. For *β%*, it is calculated by

$$\beta\% = \frac{I_\beta}{I_c} \cdot 100$$

where I_β is the intensity of β diffraction peak.

From the data listed in *table 3.7* we find that before thermal treatment $X_c\%$ of PVDF is around 51% which has a relative high crystallinity due to the orientation by injection. Meanwhile, according to references for PVDF, [86, 88] diffraction peaks at *2θ* for α crystalline polymorph appear at 17.66^o for (100), 18.3^o for (020), 19.9^o for (110) and 26.56^o for (021), respectively. For β crystalline polymorph, the diffraction peak appears at 20.26^o for (110) with (200). Thus as illustrated in *Figure 3.13 (a)*, the main crystalline polymorph for PVDF is α polymorph and *β%* is so tiny that can be nearly neglected. This is in agreement with literatures [91] we mentioned in chapter 1: without drawing-poling or additives, the β polymorph in PVDF is hard to induce due to a high transition energy barrier.

As the temperature increasing, we find that intensities of crystalline peaks become weak gradually especially in annealing stage as the signature of a melting process. It is known that the melting process applied to polymer suggests not a solid-liquid phase transition but a transition from a crystalline or semi-crystalline phase to a solid amorphous phase. In other word, the property in question is more properly called the crystalline melting process. For PVDF, tested melting point is around 170^oC and the crystallization one is around 150^oC. Thus, annealing at 150^oC for 30*min* partly destroys crystalline and during the cooling process, PVDF will re-crystallize and its *Xc%* will return back to 52.5% at 30^oC. In the whole thermal process, the main crystalline polymorph of PVDF is always α polymorph with tiny β polymorph (0.49%). Thus merely annealing does not promote the β polymorph formation which is also in agreement with the literature. [91]
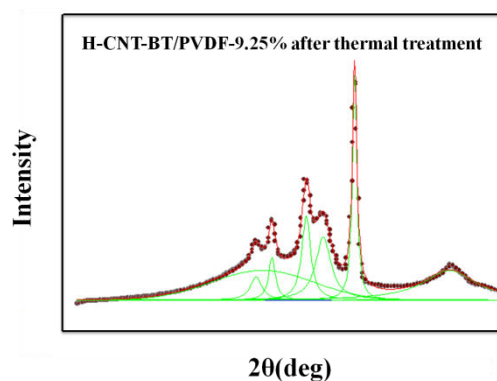
3.3.2 Wide-angle X-ray diffraction for the composite
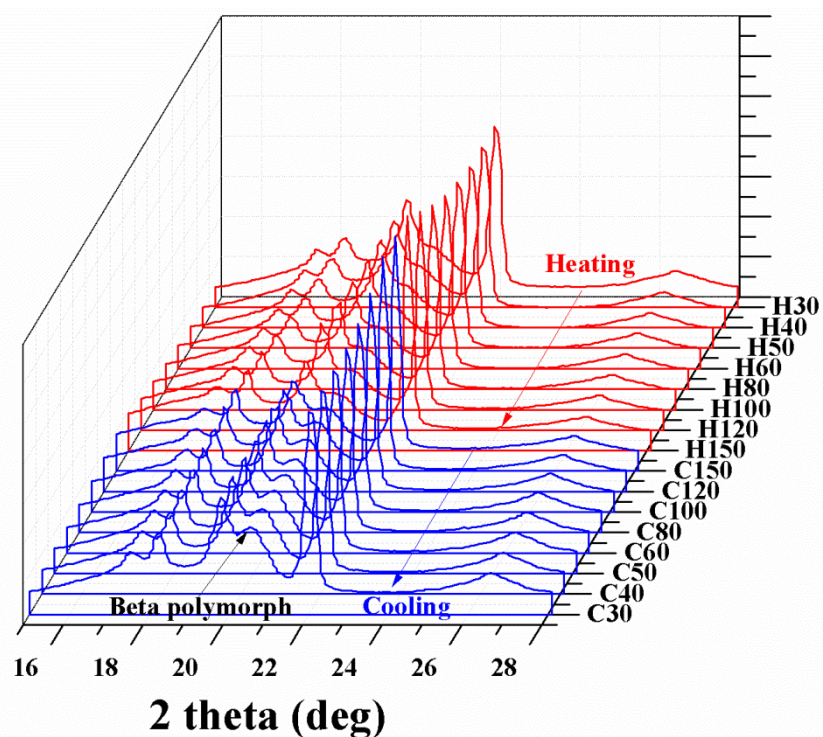
(a)
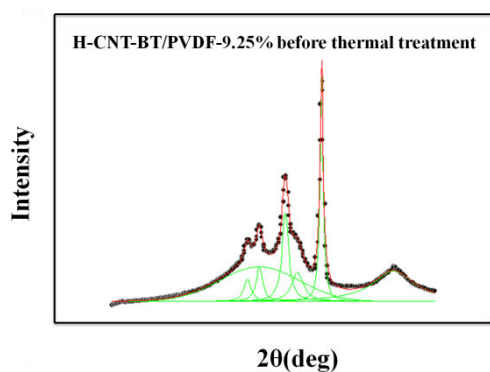
(b)

(c)

Figure 3.14 (a) WAXD of H-CNT-BT/PVDF-9.25% at different temperatures; **(b)** and **(c)** are profile analysis of diffractometer scans for before and after thermal treatment, respectively.

Table 3.8 $X_c\%$ and $\beta\%$ at different temperatures for H-CNT-BT/PVDF-9.25%

calculated by the results of temperature dependence of WAXD

Temperature (^{o}C)	$X_c\%$	$\beta\%$
30	58.6%	13.0%
40	58.0%	14.6%
50	56.6%	15.5%
60	56.1%	15.9%
80	54.5%	17.4%
100	52.9%	18.3%
120	51.2%	19.7%
150	49.0%	21.5%
Annealing at 150°C for 30*min*		
150	52.3%	23.9%
120	55.9%	24.6%
100	59.2%	25.2%
80	60.8%	22.9%
60	62.5%	23.9%
50	63.5%	25.1%
40	64.7%	25.3%
30	65.7%	25.1%

Comparing with data in *table 3.8*, we find three interesting phenomena. Firstly, $X_c\%$ of H-CNT-BT/PVDF-9.25% is higher than that of PVDF since CNT in H-CNT-BT is as the nuclei which promotes PVDF's crystallization. Meanwhile, there is some β polymorph appearing in the crystalline which is marked by a black arrow in *Figure 3.15(a)*. Secondly, during the heating stage, $X_c\%$ of H-CNT-BT/PVDF-9.25% decreases as temperature increasing which is as similarly as pure PVDF. But *β%* of H-CNT-BT/PVDF-9.25% is increasing gradually according to fitting results. Thirdly, *β%* is further increasing during the cooling stage. When the sample comes back to the room temperature, *β%* of H-CNT-BT/PVDF-9.25% reaches 25%. It is almost twice as

much as that of before thermal treatment (13%→25%). These phenomena mean that CNT may not only induce but also stabilize the β polymorph in H-CNT-BT/PVDF-9.25% which effectively prevents crystalline transition from β to α. According to the report, [91] the interaction between CNT and PVDF will induce β polymorphs in CNT reinforced PVDF composite by means of decreasing the energy barrier of crystalline transition from α to β. Our results happen to provide the evidence for this statement and it also infers that a thermal treatment possibly provides more energy to overcome the transition barrier from α to β and even back to the room temperature, *β%* does not decrease but increases more.

It is known that interfacial interaction between CNT and PVDF promotes interfacial crystallization process. Hence, well dispersion of CNT in PVDF matrix should induce higher crystalline fraction as a result of high surface interfaces. The high crystalline fraction for the reinforced PVDF is most probably the results of the surface interface increasing between CNT and PVDF matrix. Meanwhile, interfaces are the places that have stronger interaction caused by PVDF's polarity and CNT's π delocalized electrons compared with other part of PVDF. Thus, increasing amounts of β polymorph are probable to be formed on CNT-PVDF interfaces. Furthermore, CNTs in H-CNT-BT by CVD have different diameter's distribution, bundling characterizations and lengths. This various morphologies cause different surface energies and affects PVDF's volumetric exclusion. These nano-inclusion factors all affect PVDF's crystallization and amount of β polymorph.
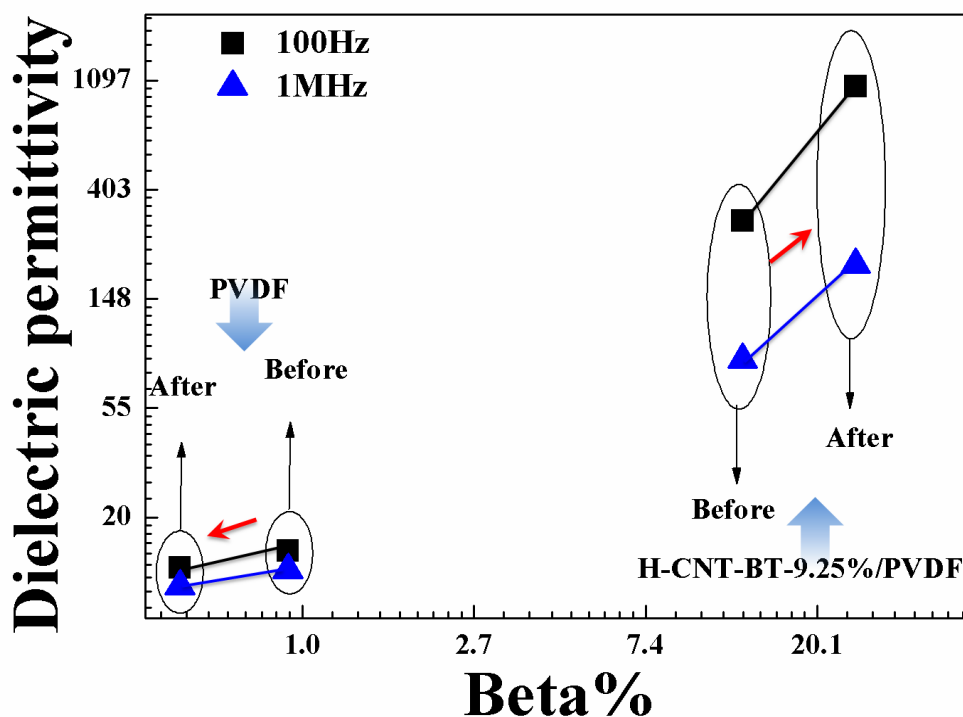
Figure 3.15 *β%* dependence of dielectric permittivity for PVDF and H-CNT-BT/PVDF-9.25%

Figure 3.15 shows *β%* dependence of dielectric permittivity for PVDF and H-CNT-BT/PVDF-9.25%. We find that the dielectric permittivity increases with the increasing of *β%* for both PVDF and H-CNT-BT/PVDF-9.25%. It is known that the dielectric permittivity of composite is largely influenced by original polymer matrix since polymer matrix is the phase with much more volume fraction according to mixing laws. β polymorph is the crystalline polymorph with the highest dielectric permittivity among all crystalline polymorphs of PVDF. Thus the increment of dielectric permittivity is possibly attributed to the increase of β polymorph in the composite. Moreover, as we mentioned before, dielectric loss for H-CNT-BT/PVDF-9.25% after thermal treatment is still at a low level (less than 1.5 at 100*Hz*). This low *tanδ* is also due to the formation of the β polymorph at the interface between CNT and PVDF. It is known that an ideal composite [3] for the high dielectric property should comprise nanoparticles with grading dielectric permittivities from the center to the border. The high dielectric permittivity of β

polymorph will be as the bridge for better combining CNT and α polymorph of PVDF in the composite which reduces dielectric loss. Due to establishing a buffer layer with medium dielectric permittivity between CNT and α polymorph in PVDF, the field intensification aroused by CNT's percolative behavior may be effectively reduced which favors to keep a low dielectric loss.

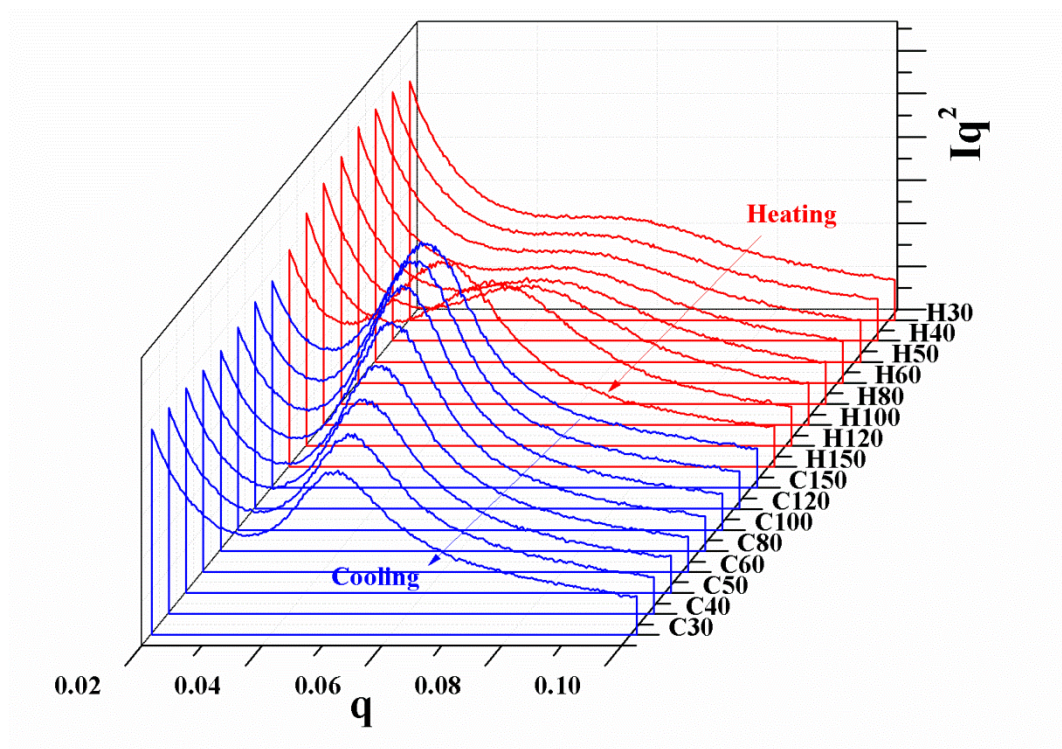### 3.4.3 Small-angle X-ray scattering for the composite

Figure 3.16 SAXS for H-CNT-BT/PVDF-9.25% at different temperatures

Table 3.9 Data of long periods at different temperatures calculated from SAXS's results

Temperature (^oC)	$X_c\%$	$L_p(\text{Å})$	$L_c(\text{Å})$	$L_a(\text{Å})$
30	58.6%	125.3	73.5	51.9
40	58.0%	127.4	73.9	53.5
50	56.6%	129.5	73.9	53.5
60	56.1%	119.6	67.1	52.5
80	54.5%	122.7	66.8	55.8
100	52.9%	122.7	64.9	57.8
120	51.2%	122.7	62.8	59.9
150	49.0%	139.6	68.4	71.2
Annealing at 150°C for 30min				
150	52.3%	139.6	73.0	66.6
120	55.9%	138.0	77.1	60.9
100	59.2%	132.5	78.4	54.1
80	60.8%	130.8	79.5	51.3
60	62.5%	128.7	80.4	48.3
50	63.5%	127.4	80.9	46.5
40	64.7%	122.7	79.4	43.3
30	65.7%	122.7	80.6	42.1

Data in *Figure 3.16* and *table 3.9* are the results of SAXS measurement. The state of nanoparticle's dispersion can be characterized by synchrotron SAXS in a straightforward fashion. From the view of SAXS, semi-crystalline polymers can be considered as periodic, condensed systems involving two regions of different electron-density-crystalline lamellae and amorphous layers, with a diffuse transition layer between them. [150, 151] Alternating crystalline and amorphous layers form characteristic stacks which can be clearly distinguished inside spherulites filling polymer volume although the structure of stacks is not perfect. Layers are not ideally

parallel and they may be curved in space changes continuously. However, since lateral dimensions of stacks are much bigger than the wavelength of X-rays, by scattering from such specific layered structures can be described by the scattered intensity which is completely determined by the electron density variation occurring in only one direction perpendicularly to layers. Thus, the analysis of SAXS curves makes possible determination of several important parameters of stacks, such as the thickness of amorphous layers and crystalline lamellae.

For a simple estimation for the thickness of long period, amorphous layers and crystalline lamellae, we use equations as follows:

$$L_p = \frac{2\pi}{q}$$

$$L_c = L_p \cdot Xc\%$$

$$L_a = L_p - L_c$$

where L_p, L_c and L_a are the thickness of long period, crystalline lamellae and amorphous layers, respectively. q is the momentum transfer or scattering vector. Herein, we choose its value of the peak in the curve of q-Iq^2 plotted in *Figure 3.16*.

Firstly, in *Figure 3.16* as the temperature increasing, peaks of curves shift to smaller q during the heat stage while in the cooling stage, q shifts to bigger value again. Meanwhile, the intensity of peak is much stronger than that of before thermal treatment. Generally, the larger the inhomogeneity size in a system is, the smaller the q value will be needed in order to determine the structure. [152] The peak shifting to smaller q means L_p of PVDF and H-CNT-BT's dispersion have some change during the thermal treatment. If comparing with the calculated L_p, L_a and L_c, in *table 3.8*, we find that as the temperature increasing, data of L_a does not change so much at first (from 30 to 120°C) but data of L_c decreases. However, as the temperature reaching 150°C, data of L_a has increased from 51.9 to 71.2Å. After annealing for 30*min*, L_a begins to shrink gradually and until the sample cooling to the room temperature. This gradually decrease of L_a demonstrates that the shrinkage of neighboring CNTs' distance and the change of conductive network possibly happens in this process.

It is know that CNT's dispersion largely depends on processing ways and usually

the discussion of thermal treatment's effect focuses on the annealing temperature which is a bit above the melting point. [153-159] In other word, if the composite is annealed above polymer matrix's melting point, the secondary agglomeration of CNT possibly occurs in the melting stage which easily causes the reformation of conductive network. However, in this study we find that not only during the melting stage but also in the re-crystallization stage influences the change of CNT's conductive network. Thus, the conductive network in a composite is affected not only by CNT's volume fraction, but also by the nature of polymer matrix and their processing ways, especially for semi-crystalline polymer matrix. If the sample is conducted by a thermal treatment, the system will be in a thermodynamic equilibrium state, the CNT's conductive network will become very sensitive especially approaching to the percolation threshold. Moreover, the difference in the interfacial energy between the CNT and PVDF including coefficient of thermal expansion (CTE) is usually high which will make the conductive network increase sensitivity to the thermal treatment. [160] Hence, the change in the thickness of L_p, L_c and L_a detected by SAXS suggests that distance's change between neighboring CNT after thermal treatment is mainly attributed to PVDF's amorphous layers.

By a comparison of data in *table 3.10*, we find that both at 100Hz and 1MHz, dielectric permittivity after thermal treatment has a significant increment but the thickness of crystalline lamellae increase while the thickness of amorphous layers decrease. This is associated with collaborative effects of two kinds' polarizations on dielectric property. On the one hand, the crystalline PVDF usually has more regular structure which will promote dipoles orientational polarization. This kind of polarization usually happens at high frequency which has shown in chapter one. The increment of dielectric permittivity at 1MHz can be associated with the change of L_c. Moreover, considering the increment of $\beta\%$ after thermal treatment, it can be inferred that the increment of dielectric permittivity at 1MHz is possibly caused by the crystalline polymorph transition and the increment of L_c. On the other hand, as we have already mentioned before, the increment in dielectric permittivity at 100Hz is attributed to strong interfacial polarization. The shrinkage of amorphous layers after

thermal treatment provides more possibility for reducing the distance between neighboring CNTs. Furthermore, if we compare with the calculation results of tunneling effect, the shrinkage of around $10\mathring{A}$ in L_a will provide enough possibility for neighboring CNTs' distance change and arousing the tunneling effect.

Table 3.10 The comparison of changes in the dielectric permittivity and the long period before and after thermal treatment

H-CNT-BT/PVDF-9.25%	$\varepsilon'@100Hz$	$\varepsilon'@1MHz$	$L_c(\mathring{A})$	$L_a(\mathring{A})$
Before	304	85	73.5	51.9
After	1040	203	80.6	42.1
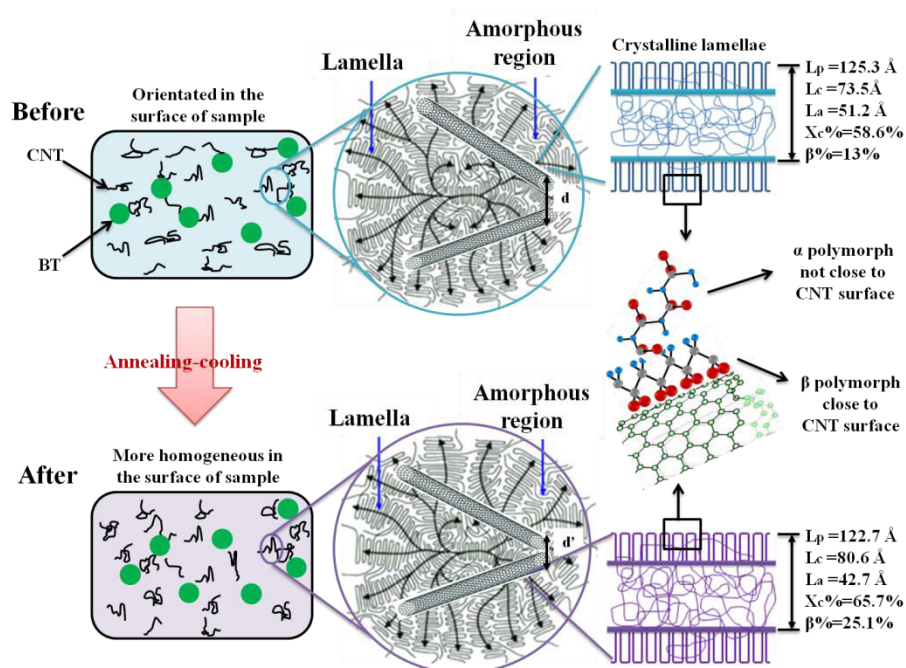
Figure 3.17 Scheme of changes of PVDF's long period and CNT's dispersion between before and after annealing treatment

After the analysis of WAXD and SAXS, a brief summary of thermal treatment's effect is illustrated in *Figure 3.17* from two aspects. On the one hand, in the case of conductive network's reformation, the thermal treatment may change the orientation of PVDF and CNT which makes CNT to disperse in more random mode in the

composites. This effect for the dielectric property largely depends on $f_{H\text{-}CNT\text{-}BT}$ and percolative behavior. If $f_{H\text{-}CNT\text{-}BT}$ is far away from f_c, the dielectric permittivity will decrease a bit due the less regularity of the dipole after the thermal treatment. If $f_{H\text{-}CNT\text{-}BT}$ is approaching to f_c, as the case of H-CNT-BT/PVDF-9.25% shown in the scheme, the effective conductive network's change will lead to tunneling effect and consequently improve the dielectric permittivity by strong interfacial polarization. This process mainly happens in the PVDF's amorphous part via the shrinkage in the thickness of L_a after thermal treatment. On the other hand, in the case of PVDF's crystalline part which is expressed by spherulities, the thermal treatment will increase crystallinity and promote the β polymorph at the interface of CNT and PVDF. This interfacial crystalline layer composed by β polymorph forms an ideal dielectric structure with grading dielectric permittivities from the center to the border, namely CNT→PVDF's β polymorph→PVDF's α polymorph. Combined with this ideal dielectric structure and BT particles' buffer of the leakage current caused by percolative behavior, the dielectric permittivity of H-CNT-BT/PVDF-9.25% increases a lot while dielectric loss remains at a low level after thermal treatment. Therefore, the change of CNT's network in the amorphous layer and β polymorph increment after thermal treatment are mainly attributed to the high dielectric performance.

3.4 Partial conclusion

H-CNT-BT/PVDF composite processed by solution casting plus extrusion-injection way has high dielectric permittivity and low dielectric loss. This high dielectric property is attributed to a good dispersion of CNT in composites. It is due to H-CNT-BT's special structure achieving an extremely low CNT's percolation threshold (f_{CNT}=2.77%) for H-CNT-BT/PVDF composites. Furthermore, this good dispersion of CNT favors to induce β polymorph of PVDF and improves the dielectric property in a wide range of frequency.

After thermal treatment, the dielectric property of the composite is further increased even the sample is cooling to the room temperature. This increment of

composite's dielectric permittivity depends on hybrid's volume fraction and parameters of the thermal treatment involving annealing temperature, annealing duration and multi-cycle annealing, and cooling rates. Concretely, firstly, the volume fraction of hybrids should be close to the percolation threshold so that the effective decrement of neighboring CNT's distance can induce the tunneling effect. Secondly, the annealing temperature should be high enough to cause partly melting in the crystalline of PVDF and arouse the effective shrinkage of amorphous layers. Thirdly, the reformation of CNT's conductive network is the kinetic process which needs enough time to complete contacting of CNTs. Prolonging annealing duration and multi-cycle annealing will reduce the sensitivity of CNT's conductive network which stabilizes and enhances dielectric performance of composites. Fourthly, cooling rate also affects the final increment of dielectric permittivity since it influence PVDF re-crystallization behavior.

According to the results of in-situ synchrotron X-ray measurement, the increment in dielectric permittivity of H-CNT-BT/PVDF after thermal treatment is attributed to two points: one is the reformation of CNT's conductive network happens in the amorphous layer of PVDF. Thermal treatment reduces the thickness of L_a and consequently shrinks neighboring CNTs' distance. The other is more β polymorph induced at the interface of CNT-PVDF. By analysis of the re-crystallization of PVDF, we know more comprehensively about the interaction between CNT and PVDF as well as CNT's percolative behavior in a semi-crystalline polymer. It provides us useful information for achieving high dielectric property. Meanwhile, we have to consider more factors including the processing way of composites, the structure of fillers and the original property of polymer matrix.

Chapter 4 Comparison of the composites' dielectric property with different fillers——modeling and experimental investigation

_____

Introduction

In this chapter, we will investigate the dispersion of CNT in PVDF composites from three aspects. Firstly, we use the theory of excluded volume to calculate the possible percolation threshold of H-CNT-BT/PVDF composites and make comparison with the experimental one in order to discuss the structure's effect of H-CNT-BT on the dispersion of CNT. Secondly, AC conductivity of H-CNT-BT/PVDF-9.5% and CNT/PVDF-8% is compared at different depth of sample vertical to injection direction in order to study CNT's dispersion processed by extrusion-injection way. Thirdly, we incorporate hybrids with different structures but with the same volume fraction of BT and CNT into PVDF for preparation composites. Via analysis of dielectric property, we will discuss the structure of hybrid's effect on CNT's dispersion and the percolative behavior for PVDF composite.

4.1 Calculation for the percolation threshold of carbon nanotube-BaTiO₃ hybrids/polyvinylidene fluoride

4.1.1 The excluded volume and percolation threshold

The percolation threshold f_c is a critical value of composite at which conductive particles form channels through composite. It strongly depends on the size and shape of conductive fillers. In order to estimate the f_c for composite, the theory of excluded volume is widely applied in many researches. The excluded volume is the volume around an object into which the center point of an identical object is prohibited, if the two are not overlap. [161] We take a sphere as an example:
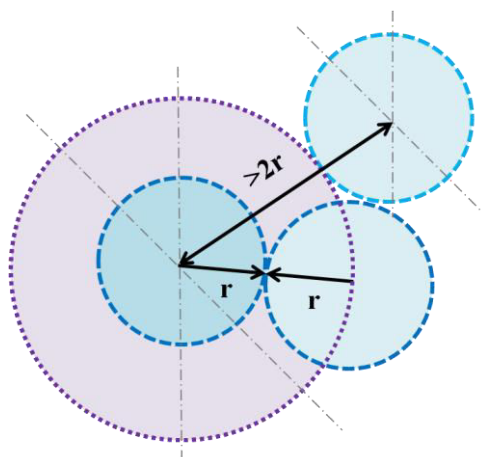

Figure 4.1 Scheme of the excluded volume of a sphere

As shown in *Figure 4.1*, radiuses of both spheres are *r* and if there is no mutual contacting, the distance between two centers of them should be larger than double times of their radius. Thus the excluded volume of a sphere can be written as:

$$V_{sphere} = \frac{4}{3} \cdot \pi \cdot (2 \cdot r)^3 = \frac{32}{3} \cdot \pi \cdot r^3$$

In a CNT reinforced polymer system, in order to calculate f_c by the theory of excluded volume, most of works have consistently modeled CNT as a penetrable, straight, capped cylinder. As pointed out by L. Berhan and A.M. Sastry's hard-core model, [162]

if treating CNT as a spherocylinder of the length *L* and the radius *R*, the excluded volume is given by

$$V_{ex} = \frac{32\pi}{3} R^3 \left[1 + \frac{3}{4}\left(\frac{L}{R}\right) + \frac{3}{8\pi}\langle \sin\theta \rangle \left(\frac{L}{R}\right)^2 \right]$$

where $\langle \sin\theta \rangle$ is the average value for two sticks with the angle θ between them. For a random distribution:

$$\langle \sin\theta \rangle = \frac{\pi}{4}$$

The core volume of a single spherocylinder can be written as

$$V = \frac{4\pi}{3} R^3 + \pi R^2 L$$

By Monte Carlo simulations, f_c is found to be inversely proportional to the excluded volume. The analytical solution for the volume fraction near percolation threshold is often expressed as

$$f_c = \frac{V}{V_{ex}} c$$

where *c* is a modified factor associated with the aspect ratio of CNT. The modeling work usually focuses on how to revise f_c combining theoretical models and actually shapes by adding more modified factors into consideration.

In the classic percolation theory, the conductive network is considered to be formed through the intimate connection between adjacent conducting fillers. However, in some practical cases, it usually obeys to another mechanism. Conductive particles are connected not geometrically but electrically via tunneling. In this case, the percolation network has already been formed even thought a geometrically connected network is still absent. Therefore, simulation works can also provide a good tool to investigate the effect of parameters on the tunneling distance including CNT types, surface functionalization and molecular weight of the polymer matrix in the composite which cannot easily be carried out by experiments.

In our system, H-CNT-BT is not a simple mixture of CNT and BT particles in PVDF. Instead, it has an initial structure that BT is as core and CNT grows on its surface. Thus, by calculating f_c we can understand better the function of parameters of H-CNT-BT involving the size of BT, the aspect ratio of CNT and the thickness of

interface, etc. After the discussion about H-CNT-BT's role on f_c of H-CNT-BT/PVDF, we will have a comprehensive view of H-CNT-BT and their contribution for the improvement of dielectric property. Hence, in this part, we are based on modeling works of high-aspect-ratio fiber system and the theory of excluded volume in order to estimate f_c for H-CNT-BT/PVDF's system.

4.1.2 The parameters and method involved in the calculation

Before starting the calculation, some parameters used are defined at first in *Figure 4.2*. We assume the radius and the length of CNT per BT particle is r_c and l, respectively while the radius of BT particle is r_p. These three parameters' ranges can be observed by SEM. The SEM image for the morphology of H-CNT-BT is provided in *Figure 4.3*.

Parameters:
i: the thickness of interface outside a single particle, herein, we set it as $0.5nm$
r_p: the radius of a BT particle observed by SEM
r_c: the radius of a CNT observed by SEM
r_{c+i}: the radius of CNT with polymer interface
t: the ratio of hard core and the soft shell
l: the length of CNT
$a = l / r_{c+i}$: the aspect ratio of the CNT observed by SEM
w_t: the weight fraction of CNT in H-CNT-BT
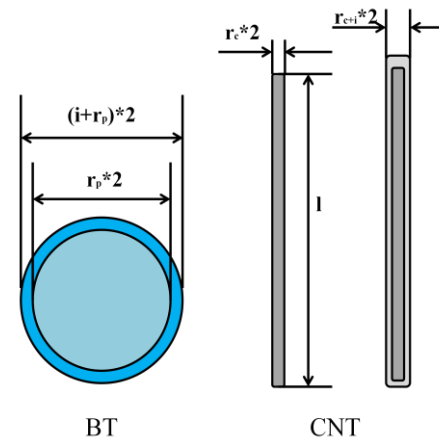n: the number of CNTs on a single particle

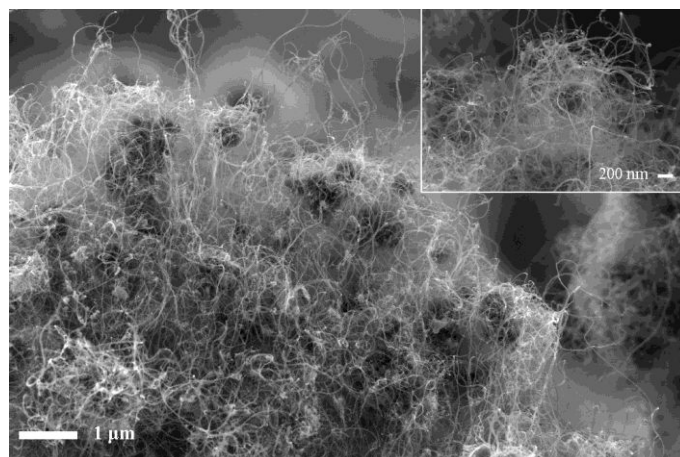**Figure 4.2** Parameters of H-CNT-BT used in the assumption

Figure 4.3 The SEM image of the morphology of H-CNT-BT

From *Figure 4.3*, we can estimate some parameters for H-CNT-BT. r_c is from 10 to 25nm, l is from 1to10μm and r_p is from 200nm to 2μm. Meanwhile, an aspect ratio, a, is also defined as the ratio of r_{c+i} and l of CNT.

When H-CNT-BT is incorporated into PVDF matrix, there is an interface wrapped around not only BT but also CNT which is so important for properties that cannot be ignored. The reason why the interface should be taken into consideration is attributed to tunneling effect in conductive behavior. As we mentioned before for electrical percolation, as the volume fraction of CNT in composite increasing, the inter-tube distance reduces and thereby increases the possibility of percolation. When the minimum distance between neighboring CNTs reduces to the maximum allowed tunneling gap, then electrons can tunnel between two CNTs. The tunneling resistance is not only associated with the polymer thickness between two adjacent CNTs but also with the chemical property of polymer matrix. Hence, the polymer interfacial region between neighboring CNT cannot be ignored for the calculation of percolation threshold. We employ i and t to describe the interface of BT-PVDF and CNT-PVDF, respectively. Additionally, the number of CNT on an individual BT particle can be marked as n which can be estimated by CNT's weight fraction (w_t) measured by TGA shown in the *Figure 4.4*.
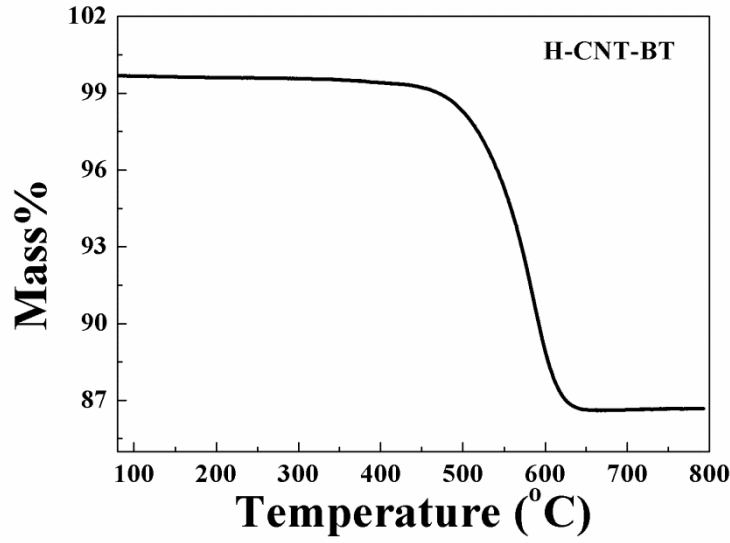
Figure 4.4 TGA for H-CNT-BT

As shown in *Figure 4.4* we can find that the weight fraction of CNT in H-CNT-BT is around 0.11. Thus, if we want to estimate the number of CNT per BT particle, we firstly suppose the mass of total CNT in H-CNT-BT as w_t while BT particles as $1\text{-}w_t$. The whole number of BT particles can be written as

$$N_{total\,BT} = \frac{(1 - w_t) \cdot N_A}{M_{BT}}$$

where N_A is the Avogadro constant, N_A=6.022 141 79(30)×10^{23} /*mol* and M_{BT} is the molar mass of BT which is 233.192*g/mol*. Meanwhile, the volume of total BT particles can be written as

$$V_{total\,BT} = \frac{1 - w_t}{\rho_{BT}}$$

where ρ_{BT} is the density of BT which is 6.02*g/cm³*. Similarly, total CNT's volume can be written as

$$V_{total\,CNT} = \frac{w_t}{\rho_{CNT}}$$

where ρ_{CNT} is the density of CNT and we use 2*g/cm³*. Thus, a volume's ratio between total BT and total CNT can be expressed as

$$\frac{V_{total\,BT}}{V_{total\,CNT}} = \frac{N_{total\,BT}}{N_{total\,CNT}} \cdot \frac{V_{single\,BT}}{V_{single\,CNT}}$$

119

The average number of CNT per BT particle, *n*, can be written as

$$n = \frac{N_{\text{total CNT}}}{N_{\text{total BT}}} = \frac{\rho_{\text{BT}} \cdot w_t \cdot V_{\text{single BT}}}{\rho_{\text{CNT}} \cdot (1 - w_t) \cdot V_{\text{single CNT}}}$$

where $V_{single\ BT}$ and $V_{single\ CNT}$ are the volume for a single BT particle and a single CNT, respectively. They can be written as

$$V_{\text{single BT}} = \frac{4}{3} \cdot \pi \cdot (r_p + i)^3$$

$$V_{\text{single CNT}} = \frac{4}{3} \cdot \pi \cdot r_{c+i}^3 + \pi \cdot l \cdot r_{c+i}^3$$

Consequently, the core volume of a single H-CNT-BT is

$$V_{\text{core}} = V_{\text{single BT}} + n \cdot V_{\text{single CNT}}$$

$$= V_{\text{single BT}} \cdot (1 + \frac{\rho_{\text{BT}} \cdot w_t}{\rho_{\text{CNT}} \cdot (1 - w_t)})$$

Herein, it is essential to point out that the radius of a BT particle should be large enough to allow CNT to grow. Thus, the boundary condition of H-CNT-CNT among r_p, *n* and r_{c+i} is

$$4 \cdot \pi \cdot r_p{}^2 \geq 4 \cdot \pi \cdot r_{c+i}^2 \cdot n$$

According to the way used in literatures, [163,164] the percolation is defined as the formation of a connected cluster that spans a representative volume element. Herein, we return to a semi-empirical, analytical result pointed out by Balberg et al. We assume CNT to be a straight cylinder of length *l* and radius *r*, with hemispheric end caps to allow comparison of results in the $l/r \rightarrow 0$ limit with the assumption that the number of objects per unit volume at percolation q_p is inversely proportional to the excluded volume V_{ex} of one of the objects, i.e.,

$$q_p \propto \frac{1}{V_{ex}}$$

where V_{ex} is the excluded volume we have mentioned (the volume around the object into which the center point of an identical object is prohibited, if the two are not overlap).

In the case of H-CNT-BT, we also treat it as a sphere which is shown in the *Figure 4.5*.
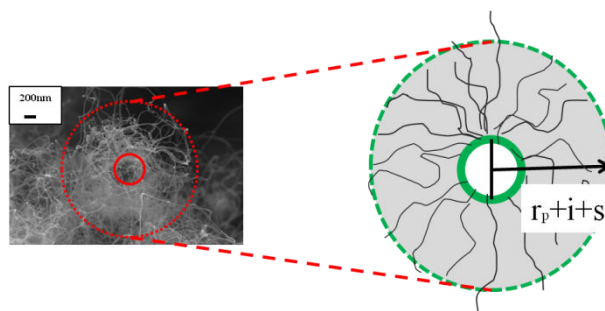
Figure 4.5 Sphere model used in H-CNT-BT for calculating its excluded volume

We consider H-CNT-BT is a sphere whose radius is composed of two parts: one is BT's radius which is marked as r_p+i while the other is the effective length of CNT which is marked as *s* as shown in *Figure 4.5*. A suitable approach to modeling percolation in the fiber reinforced polymer matrix composite is "hard-core model" where each conductive inclusion is modeled as an impenetrable hard core surrounded by a soft shell and the hard core stands for the actual inclusion and the thickness of surrounding penetrable soft shell is related to tunneling distance. Although the interface effect is considered into "hard-core model", it is still not enough for our system since treatments for the hard-core approach to model percolation of fibrous systems are limited for lower aspect ratio fillers. However, CNT in H-CNT-BT is with large aspect ratio as illustrated in the SEM image of *Figure 4.5*. Hence, "hard-core model" cannot be simply employed in our system and some modification is needed to fit H-CNT-BT's system in order to let the calculated result get closer to the experimental one.

Another popular approach in modeling percolative behaviors of composites reinforced by high aspect ratio fibers is "soft-core model" which considers the fiber as a soft core (i.e., fully permeable) rod and assumes that the onset of both geometric and electrical percolation occur simultaneously. In spite of differences between a soft-core fiber network model and an actual CNT loaded composite, "soft-core model" has been proved to predict the percolation threshold in high agreement with experimental data. Therefore, in the case of H-CNT-BT/PVDF system, we will take the way of references [162, 144] and combine two models together by means of defining a parameter,

t, as the ratio of CNT's core radius, r_c, and outer radius with a soft shell for CNT, r_{c+i}.

$$t = \frac{r_c}{r_{c+i}}$$

The soft-core limit can be expressed as *t=0* while the hard-core limit is given by *t=1*. Moreover, considering that CNT in H-CNT-BT as illustrated in *Figure 4.5*, they are helical, wavy and entangled with others rather than straight like sticks. Directly using the length of CNT as an effective length will bring much discrepancy for the calculation. Thus, a modified factor, *m*, is used to consider shape's factor. According to the research of Berhan and Sastry, they have investigated the effect of CNT's waviness on percolation threshold and the validity of excluded volume rule for systems of wavy fibers. According to their method and several tests in the calculation, for H-CNT-BT's system, the effective length of CNT, *s*, will be given by

$$s = a \cdot r_{c+i} \cdot m$$

where m=0.499. Hence, the excluded volume for hybrids can be denoted as

$$V_{ex} = \frac{32}{3} \cdot \pi \cdot [r_p + i + s]^3$$

In light of the relationship between V_{ex} and f_c as well as the high aspect ratio of CNT, the approach to predict f_c for the composite can be expressed as:

$$f_c = \frac{V_{core}}{V_{ex}}$$

The process of estimation for f_c of H-CNT-BT/PVDF is shown in *Figure 4.6*. We will discuss about the relationship among f_c and some H-CNT-BT's parameters including: the number of CNT on single BT particle, *n*, the radius of BT, r_p, the radius of CNT, r_c, the length of CNT, *l* and the ratio of hard-core to the outer radius of soft shell, *t*, respectively.
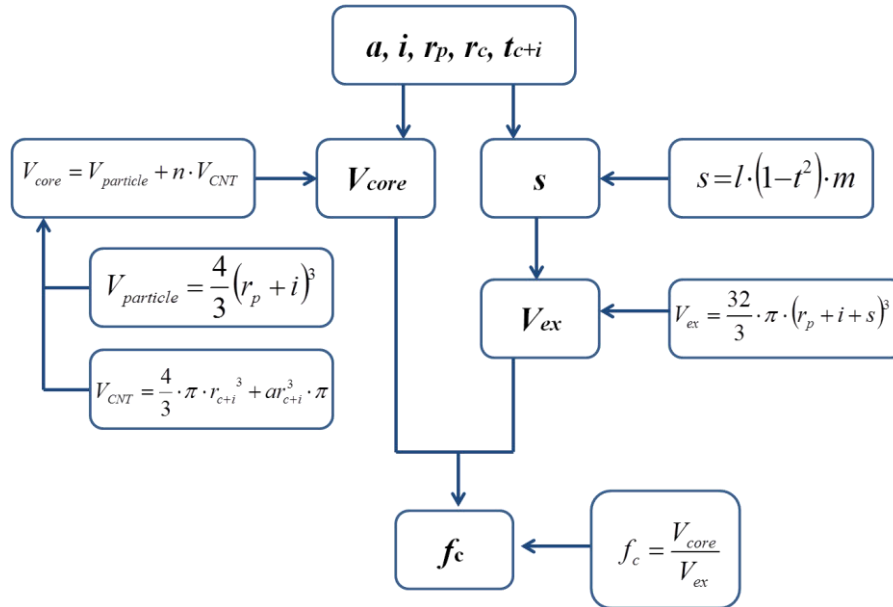
Figure 4.6 Scheme of the calculation for H-CNT-BT/PVDF

4.1.3 Results and discussion

Firstly, before calculating f_c, we firstly discuss the relationship between w_t and n. Herein, t is set at 0.85 for CNT and i at 0.5nm for BT, respectively according to the multi-core model we have mentioned in chapter one where the thickness of bonded layer is around 1nm. Meanwhile, we fix other three factors as constants for each graph and their values are shown in *Figure 4.7*.
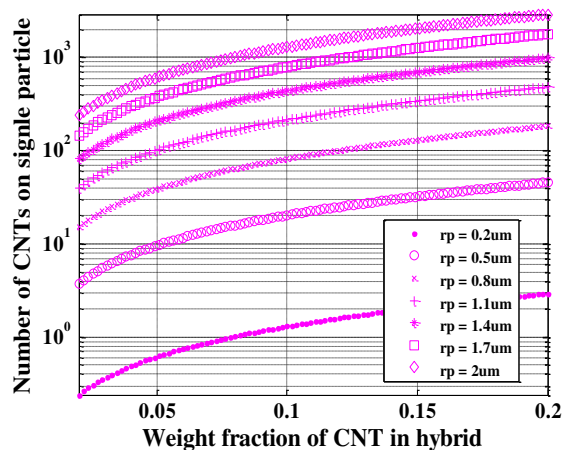
(a) *l*=7.5*μm*, *t*=0.85, *r$_c$*=15*nm*
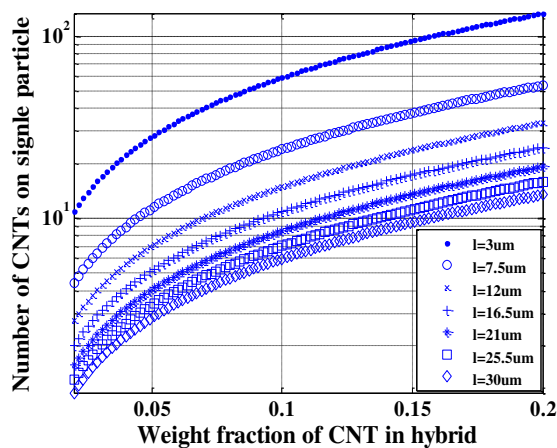
(b) *r$_p$*=500*nm*, *t*=0.85, *r$_c$*=15*nm*
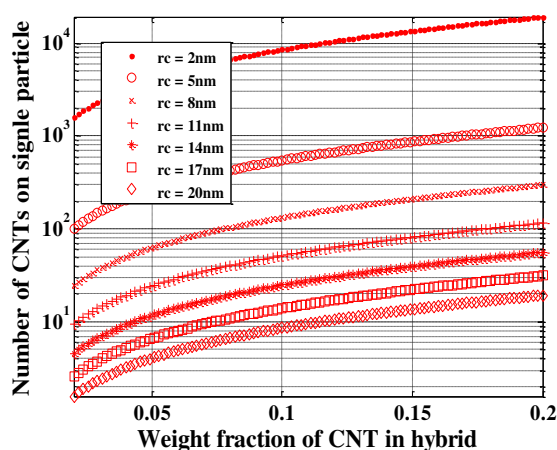
(c) *r$_p$*=500*nm*, *t*=0.85, *l*=7.5*μm*

Figure 4.7 Calculated results of the relationship between *w$_t$* and *f$_c$* changing with *r$_p$*, *r$_c$*, *l* and *t*. (a) *r$_p$*-*f$_c$*, (b) *l*-*f$_c$* and (c) *r$_c$*-*f$_c$*, respectively

Three pictures illustrated in *Figure 4.7* provide the information that n is dependent on not only w_t but also r_p, l and r_c. It is easy to understand that n increases as w_t increasing due to more amount of CNT in H-CNT-BT. Furthermore, as shown in *Figure 4.7*, we find that three shape factors of H-CNT-BT (r_p, l and r_c) influence n in various ways. Concretely, as shown in *Figure 4.7 (a)*, n increases with r_p's increasing while decreases with l and r_c's increasing as shown in *Figure 4.7 (b)* and *(c)*, respectively. It is because a BT particle can provide more space with larger radius which promotes more CNTs growing outside. Meanwhile, CNT with smaller radius and shorter length may decrease initial volume which also helps to enhance CNT's numbers on the surface of per BT particle. Therefore, these graphs infer that the number of CNT on a single BT particle depends on not only the weight fraction but also on morphology parameters of BT and CNT.

Secondly, we compare the relationship of calculated f_c, r_p, l, r_c and t. According to "soft-core model", t is the ratio of CNT's original radius and the radius of CNT with polymer's interface. Thus, an increasing of t means that the thickness of interface reduces. As defined, until $t=1$ means that there is no interface outside CNT.
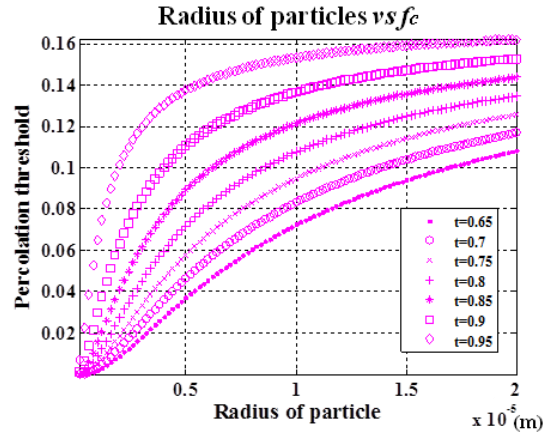
(a) r_c=15nm, w_t=0.11, a=500
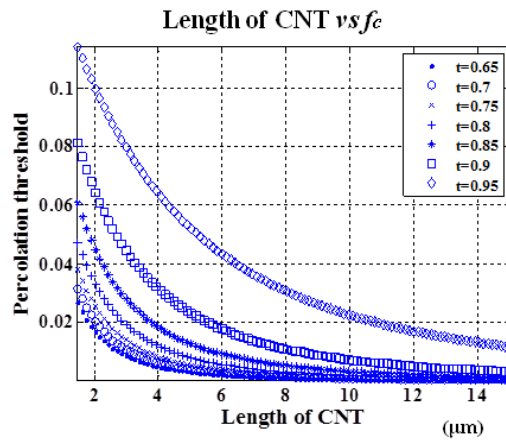
(b) r_p=500nm, r_c=15nm, w_t=0.11
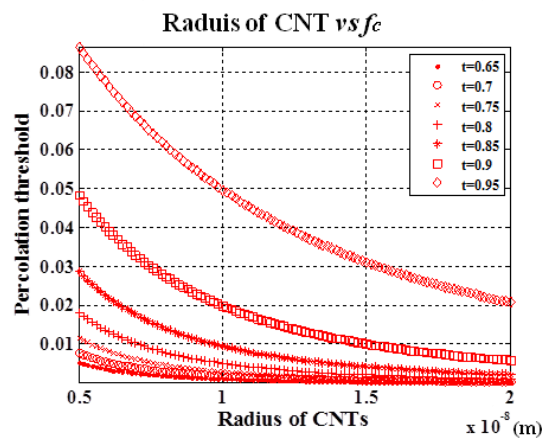
(c) r_p=500nm, w_t=0.11, a=500

Figure 4.8 Calculated results for three factors' effects on f_c with different t. **(a)** r_p-f_c, **(b)** l-f_c and **(c)** r_c-f_c, respectively

From three figures shown in *Figure 4.8*, we find that the estimated f_c for H-CNT-BT is less than 0.16 no matter how much change of r_p, r_c and l. This is in agreement with Zallen's study. [165] The theoretical value of f_c is approximately 0.16 for a homogeneously dispersed system which contains randomly oriented fillers of spherical shape with similar dimensions. Furthermore, if compared with experimental data reported in references, [3] for most spherical conductive fillers, the experimental f_c is often distributed in a broad range from 0.013 to 0.17 and f_c are usually lower than 0.16. A commonly accepted explanation for this discrepancy between theory and experiment is that the real statement of fillers in polymer matrix is a kind clusters formed by the randomly distributed conductive fillers with a complex shape and larger aspect ratio than that of each filler itself. The dimension of clusters plays a crucial role on determining f_c in percolative composites of spherical conductive fillers. Hence, we plot three parameters dependence of f_c with different t in *Figure 4.8 (a)*, *(b)* and *(c)*, respectively, in order to view morphologies' and interface's effects on f_c.

Firstly, we start by *Figure 4.8 (a)*. We set r_c at 15*nm* and the aspect ratio, a at 500, respective. We plot r_p dependence of f_c with different t. We find that f_c increases as r_p increasing. It is because during the calculation procedure, f_c is the ratio of H-CNT-BT's core volume and its excluded one. Thus, both volumes increase as r_p increasing, but the volume of core increases faster than excluded volume. This difference between two volumes' changing rates leads to f_c increasing with r_p. This shows that for a percolative system, simply increasing size of conductive fillers will not probably cause low f_c. In experimental cases, it is also a common phenomenon since the factor usually influences f_c is the dispersion of fillers rather than their real sizes.

Secondly in *Figure 4.8 (b)*, we set r_p at 500*nm* and r_c at 15*nm*, respectively. We plot l dependence of f_c with different t. As l increasing f_c reduces which means that the longer the CNT on a BT particle is, the lower f_c of the composite will be achieved. Because CNT with longer length is easier to contact with others even though in a lower volume fraction the percolative behavior in the composite will also be easy to form in this case. This is proved by experimental data. Li et.al have used Al_2O_3-CNT

hybrids with different aspect ratios in the epoxy composite. They have found that the composite reinforced by Al_2O_3-CNT hybrids with higher aspect ratio has a lower f_c compared with those of lower aspect ratio. Lin et.al have also found similar result in the system of Al_2O_3-CNT/ poly(dimethylsiloxane) (PDMS) composites.

Thirdly, we set r_p at $500nm$ and a at 500, respective. We plot r_c dependence of f_c with different t in *Figure 4.8 (c)*. We find that f_c also decreases as r_c increasing as similar as the case of r_p's effect on f_c. As we mentioned the number of CNT reduces per BT particle due to the increasing of r_c. But on the contrary, the excluded volume will increase which causes the decreasing of f_c. Moreover, given that CNT's radius increases, the possibility of inter-contacting will also increase. In addition, three graphs provide a decreasing trend of f_c with t reducing. We list the data of t, r_c and the thickness of shell, r_{c+i}-r_c, respectively in *table 4.1* to illustrate this point.

Table 4.1 The relationship among t, r_{c+i} and r_{c+i}-r_i

t	0.65	0.7	0.75	0.8	0.85	0.9	0.95
r_{c+i} (*nm*)	23	21	20	19	18	17	16
r_{c+i}-r_i (*nm*)	8	6	5	4	3	2	1

In the calculation procedure, the interface thickness is considered as a part into the radius of CNT, thus a smaller t means a thicker interface, namely, a bigger radius of CNT. As mentioned in the analysis of CNT radius's effect, we have known that CNT with a large radius favors to reduce f_c. It can be analogized to the case of t dependence of f_c. Meanwhile, as we have mentioned before, t is used as a parameter to describe the ratio of core's radius and outer soft shell's radius. The larger the t is, the more it approaches to the limit of hard-core model based on the theory. We employ this shell to describe polymer's interface wrapped around CNT. In a CNT reinforced polymer matrix composite, the tunneling distance depends not only on the distance of neighboring CNTs' distance, but also on polymer's type since the tunneling energy barrier height λ varies widely up to polymer's physical and chemical

property. For instance, some of polymers have low λ (e.g. for PMMA, $\lambda=0.17eV$, PVDF, $\lambda=0.3eV$), [145] whereas others have relatively high λ (e.g. for epoxy, $\lambda=1.5eV$). Hence, choosing of t depends on the type of polymer matrix and after several tests we set t at 0.85 for H-CNT-BT/PVDF composite in the followed calculation.

4.1.4 Comparison of the calculated percolation threshold with the experimental results

Table 4.2 Dielectric permittivity at three frequencies for H-CNT-BT/PVDF composite

$f_{H\text{-}CNT\text{-}BT}$	**100***Hz*	**1k***Hz*	**1M***Hz*
1%	12	12	9
2%	13	13	10
3%	15	14	11
4%	14	14	10
5%	16	16	12
6%	17	16	12
7%	21	20	16
8%	20	18	14
9%	41	37	23
9.25%	304	231	85
9.5%	250	193	85
9.75%	279	196	70
10%	1776	773	80

Figure 4.9 (a) shows the liner fit for H-CNT-BT/PVDF composite's dielectric permittivity measured at 100*Hz*. *Figure 4.9 (b)* illustrates a comparison between experimental and calculated f_c for H-CNT-BT/PVDF's system. Herein, aspect ratio, a, is employed to describe CNT's morphology. Dielectric permittivity at three frequencies for H-CNT-BT/PVDF composites with different volume fractions is listed in *table 4.2*. Firstly, it can be found that when $f_{H\text{-}CNT\text{-}BT}$ is around 9.25%, dielectric permittivity has a sudden increment (41→304@100Hz). As we have mentioned in

chapter 3, this dramatic increment means that $f_{H\text{-}CNT\text{-}BT}$ is approaching to f_c. After a slight decrease in dielectric permittivity, when $f_{H\text{-}CNT\text{-}BT}$ reaches 10%, dielectric permittivity increases significantly again (279→1776).
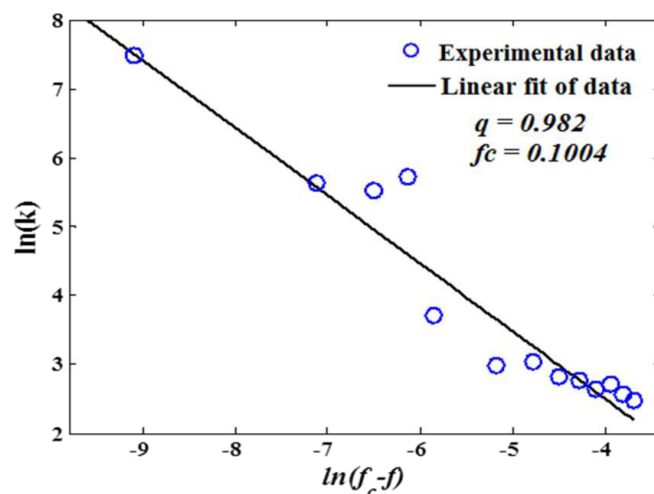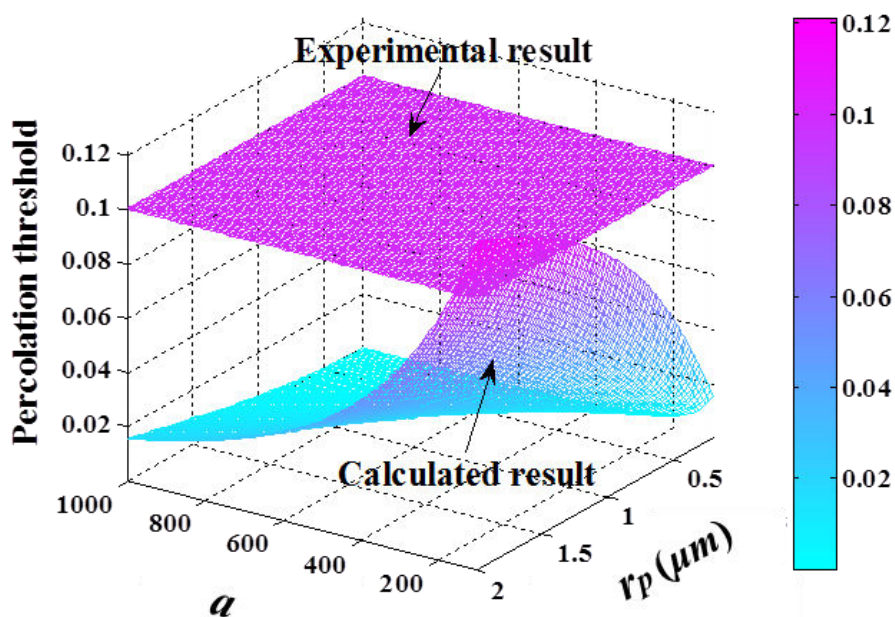

(a)

(b) *t=0.85*

Figure 4.9 (a) Best linear fit for the dielectric permittivity of H-CNT-BT/PVDF composites at 100Hz. **(b)** A comparison between experimental and calculated f_c for H-CNT-BT/PVDF system

This is a typical percolative phenomenon. The physical reason for the critical behavior of dielectric permittivity near percolation is the existence of micro-capacitor network which we have discussed in chapter 3. In order to estimate f_c from experimental data, we fit experimental permittivity data at $100Hz$ according to the equation

$$\varepsilon_{eff} \propto \varepsilon_m |f - f_c|^{-q} \quad \text{For } f < f_c$$

Where ε_{eff} is the dielectric permittivity of composite, ε_m is the dielectric permittivity of matrix, f is filler's volume fraction, respectively. The best linear fit to data at $100Hz$ to the log-log plot of the power law gives q=0.982 which agrees with the universal one (q is in the range from 0.8 to 1). Meanwhile, we find f_c=0.1004 in the law for the experimental result of H-CNT-BT/PVDF system. The fitting result is shown in *Figure 4.9 (a)*.

In the case of calculation, we mesh f_c changing with a and r_p, respectively in *Figure 4.9 (b)* and herein, we set t at 0.85. Meanwhile, we set a from 200 to 1000 and r_p from $500nm$ to $2\mu m$. In the graph, it can be found that with a increasing and r_p decreasing, f_c reduces which is in agreement with results discussed before. The experimental result (f_c=0.1004) happens to be in the range of f_c by calculation which means the treatment of CNT for H-CNT-BT is valid for H-CNT-BT/PVDF's system. Furthermore, the combination of "hard-core" and "soft-core model" by the parameter t (0.85) also works for PVDF matrix.

Via calculation work, we find that low f_c in H-CNT-BT/PVDF is possibly attributed to the unique structure of H-CNT-BT. The existence of BT particles increases the excluded volume compared with the case of merely considering the excluded volume of CNT as a spherocylinder. Meanwhile, we consider the core volume depends on the radius of BT and CNT as well as the number of CNT which also differs with the case of CNT reinforced polymer case. Thus, for H-CNT-BT/PVDF's system, the special structure is essential for a lower f_c. From the experimental view, differently from CNT reinforced polymer matrix composites, CNT in H-CNT-BT has already been dispersed by BT particles before being incorporated into PVDF and the dispersion of them by blending is the second time. Although the

blending processing partly destroys H-CNT-BT's original structure, it is still better than CNT reinforced polymer which lacks the first dispersion. Numbers of experimental results in our group can provide evidences that the dispersion of CNT by particles' carriers is better than that of merely CNT in the polymer matrix. [43, 45, 46, 47] Besides H-CNT-BT, other hybrids such as H-CNT-Al$_2$O$_3$ and H-CNT-SiC are incorporated into different polymer matrix like epoxy and PDMS to prepare composites. All composites have lower f_c than the same matrix composite reinforced only by MWNT. It is known that a good dispersion of CNT reduces f_c and finally enhances dielectric property. Hence, the application of hybrids can provide a promising way for composites with good CNT's dispersion and low percolation threshold.

4.2 Influences of hybrids' structures on carbon nanotubes' dispersion in polyvinylidene fluoride matrix

4.2.1 Comparison between carbon nanotube/polyvinylidene fluoride and carbon nanotube-BaTiO$_3$ hybrids/polyvinylidene fluoride

As we mentioned before, due to the migration and orientation of CNT under flow especially during injection process, the dispersion of CNT in PVDF is largely affected by the shear of mold's surfaces. In order to study BT's role for the composite, we compare AC conductivity in different thickness of two composites from surface to core. Herein, the reason why AC conductivity is chosen for comparison rather than dielectric permittivity is that the material in core part may become conductive which makes dielectric permittivity meaningless.

We choose two CNT/PVDF-8% samples in one slab: one is for the measurement before thermal treatment and the other is for after thermal treatment. We use an abrasive paper to polish both sides of samples simultaneously and each time the thickness is controlled by 0.1mm. In order to compare the property in a similar level, two counterparts have similar AC conductivity before thermal treatment. We plot
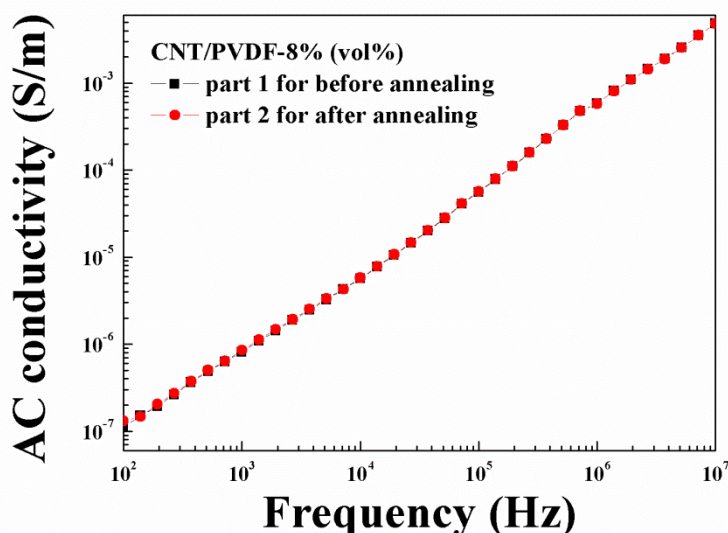
them together in *Figure 4.10* for the reference.

Figure 4.10 Frequency dependence of AC conductivity for CNT/PVDF-8% before thermal treatment.

Firstly we discuss AC conductivity for CNT/PVDF-8% before thermal treatment. Frequency dependence of AC conductivity is illustrated in *Figure 4.11*. We find that as the thickness decreasing, AC conductivity increases gradually until polishing to the core part where the value is several magnitudes larger than that of out layer part. Meanwhile, AC conductivity for each layer is strong frequency dependent but this dependence reduces as the thickness reducing. On the one hand, an obvious increment in AC conductivity in core part infers that CNT's dispersion is inhomogeneous from the surface to core. Namely, in out layer part, the dispersion of CNT is affected by molds' shearing and partly orientated. But in core part, this orientation by mold is released. The dispersion of CNT in core part is more random than that of surface part which improves the AC conductivity. On the other hand, frequency dependence of AC conductivity means that CNT/PVDF-8% is still dielectric rather than conductive even thought in core part where the dispersion of CNT is more random. Thus the dispersion of CNT may affect percolative behavior but f_c is still mainly dominant by the original volume fraction of CNT in PVDF. This is as similar as the result discussed in chapter

3. Therefore, comparing of AC conductivity in different depth of CNT/PVDF-8%, we find that in the case of CNT/PVDF processed by extrusion-injection way, CNT's dispersion largely depends on the depth vertical to the injection direction and it is more random in the core part than that of the surface part.
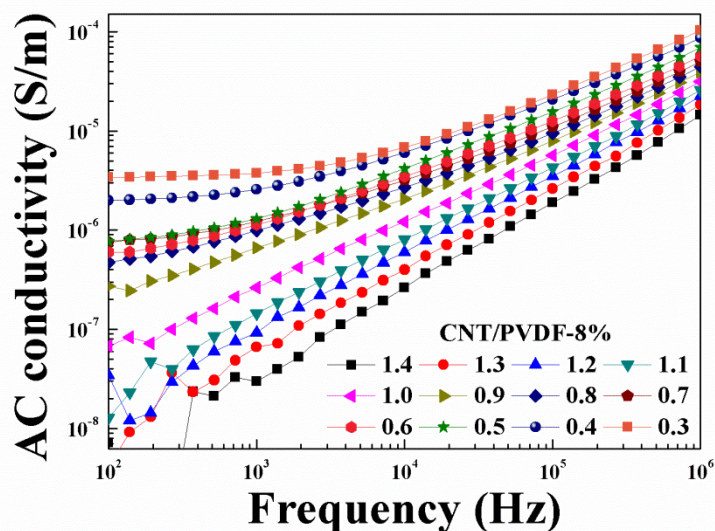

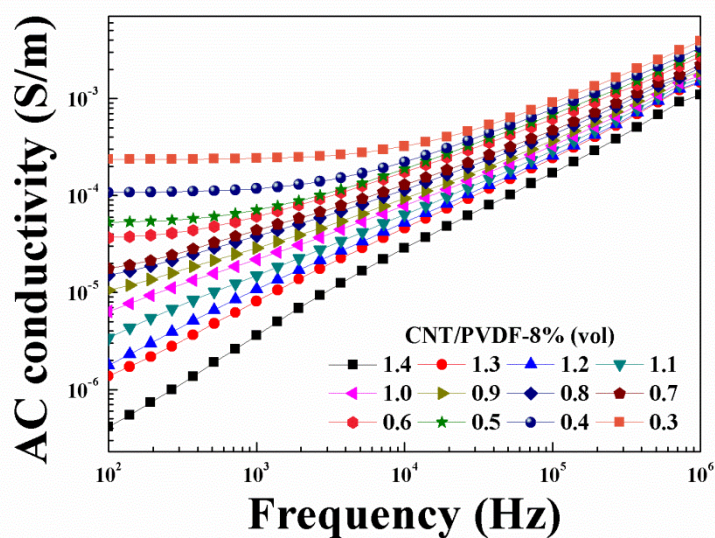**Figure 4.11** Frequency dependence of AC conductivity for CNT/PVDF-8% before thermal treatment.

Figure 4.12 Frequency dependence of AC conductivity for CNT/PVDF-8% after thermal treatment.

After thermal treatment (annealing at 150^oC for $30min$ and cooling naturally) for the counterpart, we find that AC conductivity of each layer which is shown in *Figure 4.12* has been increased near ten times than that of before. Meanwhile, each layer is still frequency dependent. We compare the increment of AC conductivity at $100Hz$ for each layer after thermal treatment and find that the increment in AC conductivity also depends on layers as illustrated in *Figure 4.13*. In the core part where CNT's dispersion is more random, the tunneling effect induced by neighboring CNTs is easy to occur due to the stimulation of thermal treatment. Therefore, for CNT/PVDF-8%, AC conductivity measured at different depth shows that CNT's dispersion is depth dependent and the more approaches to the core, the more sensitive of the conductive network will be to a thermal treatment.
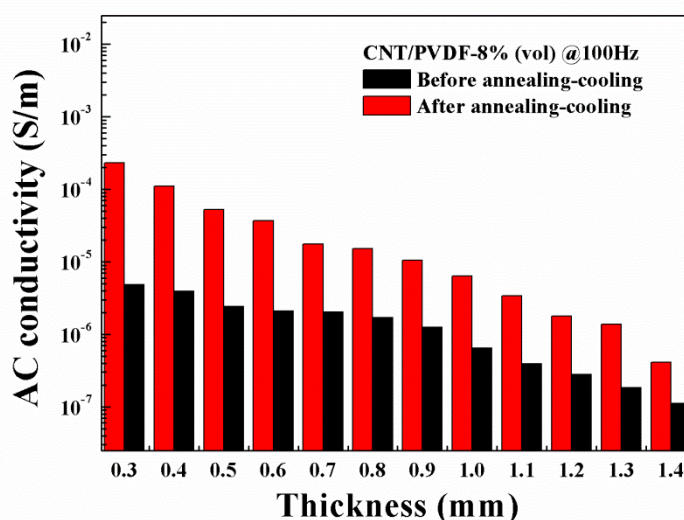

Figure 4.13 The comparison of AC conductivity at $100Hz$ of before and after thermal treatment for CNT/PVDF-8%.

We also do same measurements for H-CNT-BT/PVDF-9.5%. Similarly, at first, we choose two counterparts in one slab with similar original AC conductivity which is shown in *Figure 4.14* for the reference.
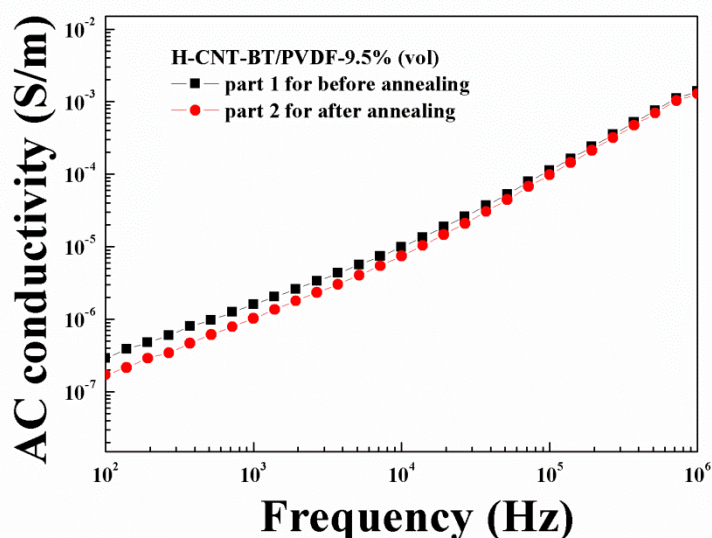
Figure 4.14 Frequency dependence of AC conductivity for H-CNT-BT/PVDF-9.5% before thermal treatment.

AC conductivity measured at 100*Hz* of before and after thermal treatment as well as their comparison are shown in *Figure 4.15 (a)*, *(b)* and *(c)*, respectively. As shown in *Figure 4.15* for H-CNT-BT/PVDF-9.5% (f_{CNT}=2.6%), comparing with CNT/PVDF-8%, we find that the dispersion of CNT in H-CNT-BT/PVDF-9.5% is less depth dependent and more random in each thickness than CNT/PVDF-8%. Although inhomogeneous dispersion of CNT by extrusion-injection processing still exists for H-CNT-BT/PVDF-9.5%, carried by BT particles, this negative effect become less since when the thickness decreases to 1.2*mm*, AC conductiviy starts to be stable and as the thickness reducing further, the value does not change in large scale. Furthermore, thermal treatment's influence for the dynamic percolative behavior also less depends on the depth for H-CNT-BT/PVDF-9.5% as shown in *Figure 4.15 (c)*. This means also that dynamic percolative behavior is more associated with the original percolation. If CNT's dispension is random and its original percolation is less sensitive with the thickness, the effect by thermal treatment will be less.
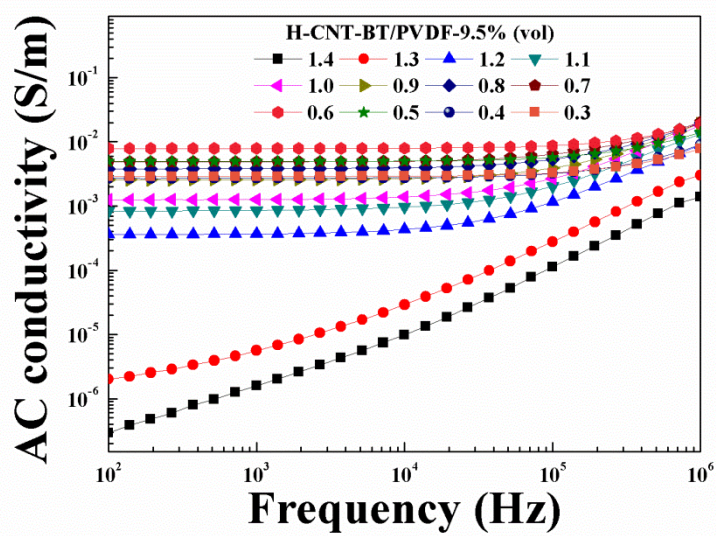
(a)
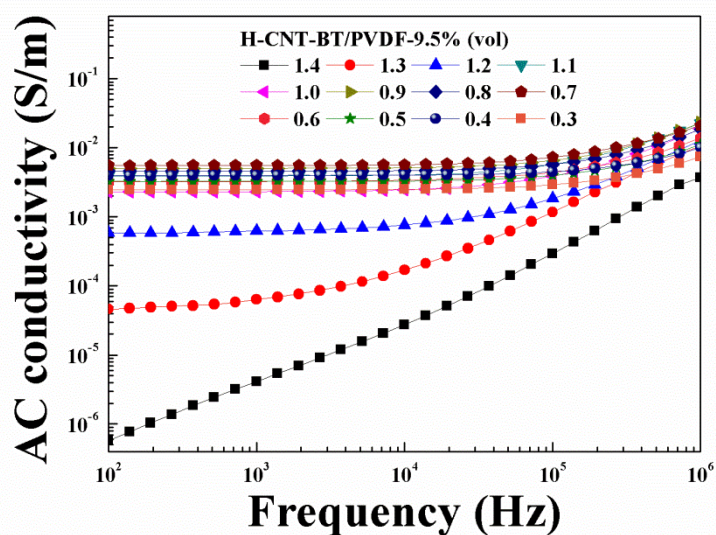
(b)
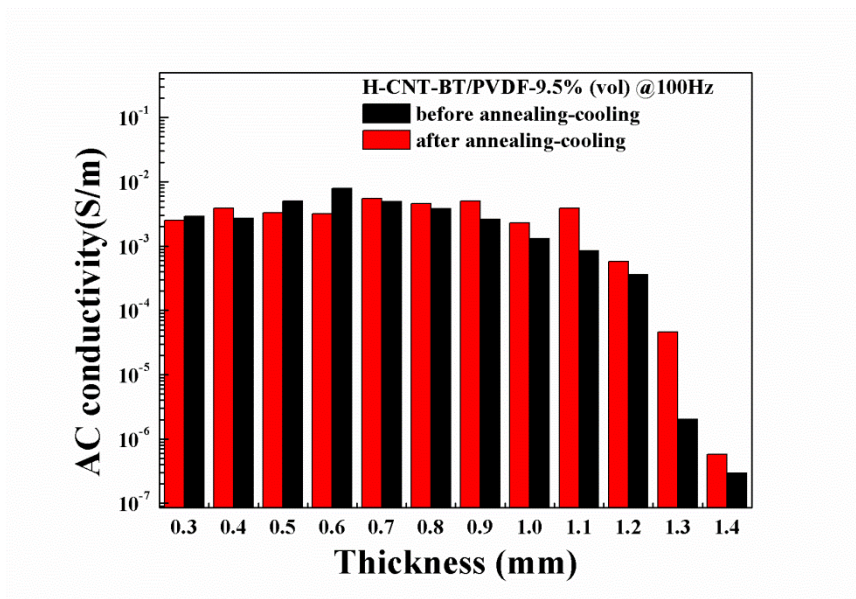
(c)

Figure 4.15 AC conductivity at 100*Hz* for H-CNT-BT/PVDF-9.5% in different thickness parts. **(a)** before thermal treatment, **(b)** after thermal treatment and **(c)** a comparison between two, respectively
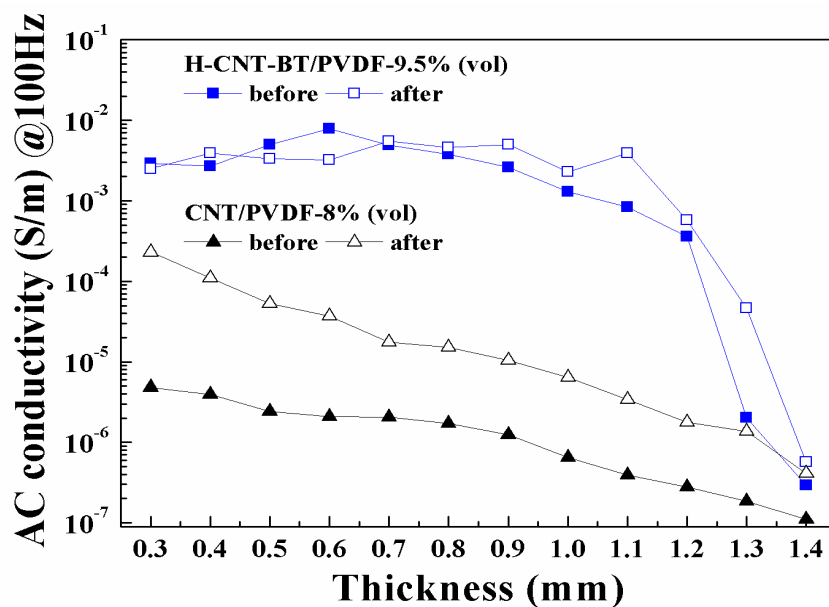
Figure 4.16 The comparsion of AC conductivity at 100*Hz* for two samples of before and after thermal treatment

We compare two samples' AC conductivity at 100*Hz* in *Figure 4.16*. We find that CNT's conductive network in H-CNT-BT/PVDF-9.5% is less sensitive to thermal

treatment than CNT/PVDF-8%. As we analysing before, CNT's dispersion largely affects the sensitivity of conductive network. The unique structrue of H-CNT-BT favors the dispersion of CNT in PVDF matrix. With the help of BT's carriers, it may be much easier to disperse CNT by traditional blending process and largely avoids CNT's aggregation. Meanwhile, CNT grown on BT may effectively prevent the restacking of BT particles and improve interfaces' amounts in the composite which may enhance synergistic effects of BT and CNT. Additionally, the surfacial growth of CNT on BT serves as bridges to connect neighboring CNTs in more easier mode than that of CNT/PVDF. These are all favorable to form more homogenerous dispersion and more stable conductive network in the composite. Therefore, H-CNT-BT not only reduces the percolation threshold for the PVDF matrix composite but also stablizes CNT's conductive network and releases negative effects by extrusion-injection process.

4.2.2 Comparison of dielectric properties for hybrids/polyvinylidene fluoride composites with different structures

Figure 4.17 TGA for H-CNT-BT and H-BT-CNT used in composites

Figure 4.17 shows results of TGA for H-CNT-BT and H-BT-CNT used in the

preparation for PVDF matrix composites. The mass loss of the thermal decomposition from 400 to $600^{o}C$ shows that CNT and BT's contents in two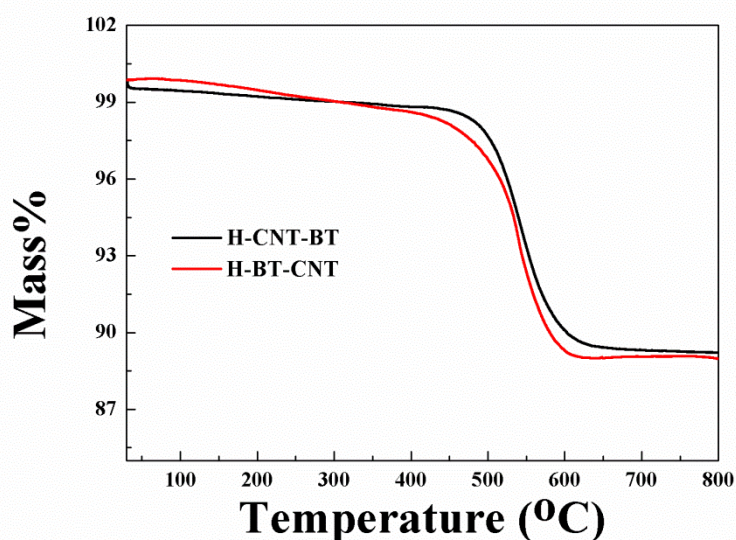 hybrids are similar and both of them have around 10% (weight fraction) of CNT. Meanwhile, it can be found that there is a bit difference in thermal stability of CNT between two samples. The CNT in H-CNT-BT is more stable than that of H-BT-CNT which may be caused by different sources. The CNT used in H-CNT-BT is prepared by CVD in our lab while the CNT in H-BT-CNT is bought from Shenzhen nanotech Port Company (China). Thus, thermal and chemical properties have a little difference. Additionally, we use this mass ratio of CNT and BT (1:9) as reference to calculate BT and CNT's contents in the case of mechanical mixing CNT/BT (M-CNT/BT) in order to have a comparison for dielectric properties. This comparison is about via fabricating three PVDF matrix composites incorporated by BT-CNT hybrids with same BT and CNT's volume fractions, 3% for CNT and 7% for BT, but with different structures.

Morphologies of three composites' fractures surfaces are shown in *Figure 4.18 (a), (b)* and *(c)*, respectively. Compared with SEM images of three fractures' surfaces, we find that two designed structures are all partly destroyed due to the process of blending with PVDF. However, some linkage between CNT and BT has been remained. Besides the situation of H-CNT-BT/PVDF-10% we mentioned in chapter 3, in the case of H-BT-CNT/PVDF-10% shown in *Figure 4.18 (b)*, we still can find some evidences of CNTs wrapped by BT particles. Moreover, in *Figure 4.18 (b)*, similarly as the case of H-CNT-BT/PVDF-10%, CNTs and BT do not agglomerate individually and their dispersion in PVDF matrix is more homogeneous than that of M-CNT/BT/PVDF-10% shown in *Figure 4.18 (c)*.
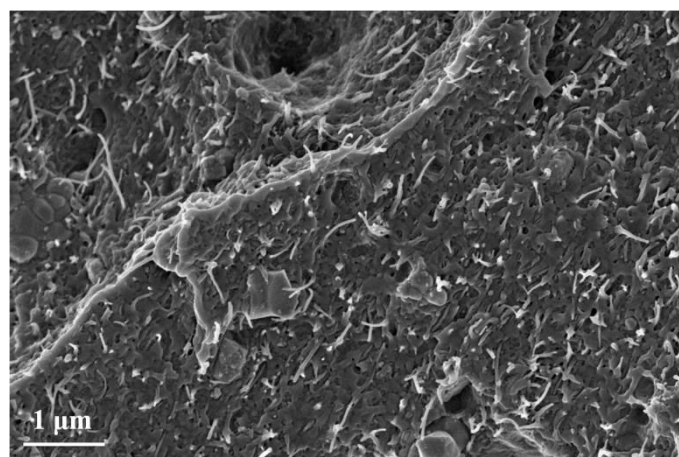
(a)
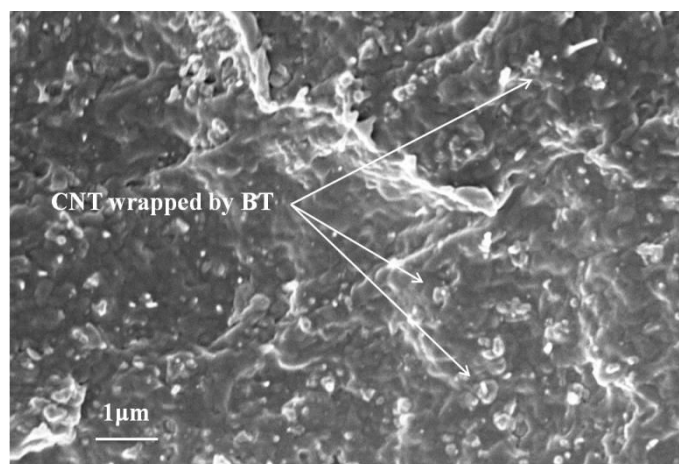
(b)
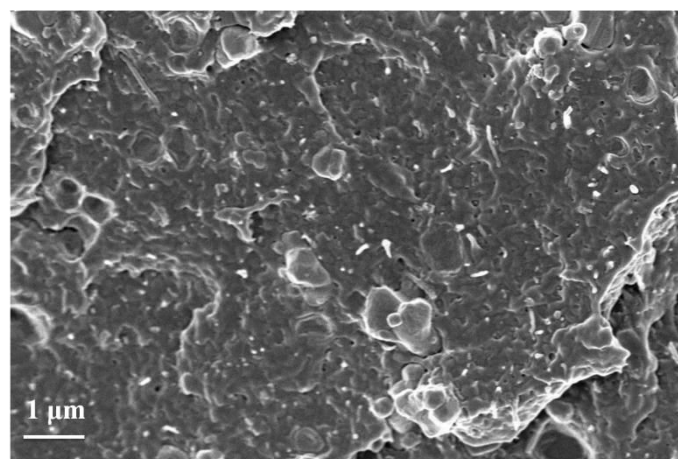
(c)

Figure 4.18 The morphology of fractures' surfaces for three hybrids reinforced PVDF composites. **(a)** H-CNT-BT/PVDF-10%, **(b)** H-BT-CNT/PVDF-10% and **(c)** M-CNT/BT/PVDF-10%, respectively.

141
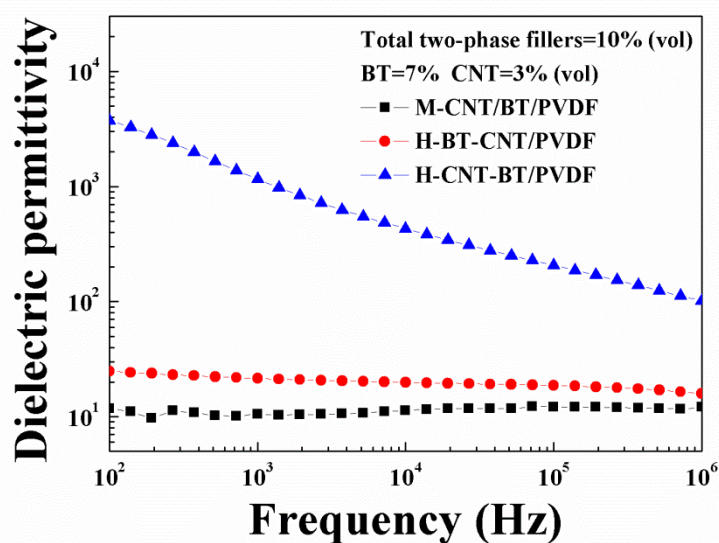
(a)
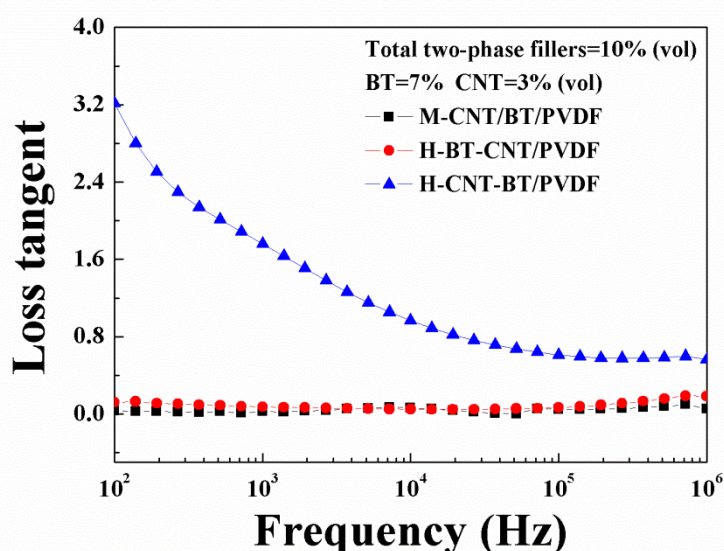
(b)

Figure 4.19 Frequency dependence of dielectric properties for three composites with hybrids of 10% volume fraction **(a)** for dielectric permittivity and **(b)** for loss tangent, respectively

Figure 4.19 (a) and *(b)* show frequency dependence of dielectric permittivity and loss tangent for three composites with hybrids of 10% volume fraction. As shown in the two figures, it is easy to figure out that there is large difference among three composites in dielectric behaviors in spite of sharing same BT and CNT volume

142

fractions. Comparing with both dielectric permittivity and loss tangent, H-CNT-BT/PVDF is the highest; H-BT-CNT/PVDF is moderate while M-CNT/BT/PVDF is the lowest. Meanwhile, we find that for H-CNT-BT/PVDF, dielectric permittivity and loss tangent is largely dependent on the frequency while the cases for other two are far less frequency dependent. This diversity in dielectric properties is possibly attributed to different structures of hybrids in PVDF matrix.

As we discussed before, H-CNT-BT has the structure that BT is as a core and CNT growing outside as a shell. This hybrid can be viewed as conductive filler since CNT can easily connect with each other without blocks of BT. They will have percolative phenomenon which we have discussed before. Thus, this high dielectric permittivity and loss tangent for H-CNT-BT/PVDF is attributed to percolative behavior which is explained by micro-capacitors model and interfacial polarization. Furthermore, although the original core-shell structure of H-CNT-BT is partly destroyed during the processing, BT and CNT still have the interaction with each other instead of separated and agglomerated individually in PVDF matrix. Thus, more interface area is possibly created for promoting interfacial polarization which benefits high dielectric property. Meanwhile, as we have analyzed before, this structure improves CNTs' dispersion in PVDF matrix. Hence, even though f_{CNT} is 3%, the bulk composite still approaches to the percolation threshold.

However, in cases of H-BT-CNT/PVDF and M-CNT/BT/PVDF, despite incorporated the same volume fraction of BT and CNT as that of H-CNT-BT/PVDF, neither of them achieves high dielectric permittivity. 3% CNT is too low to approach to the percolation threshold for either of them. Moreover, if comparing carefully, we still find the difference in dielectric properties between H-BT-CNT/PVDF and M-CNT/BT/PVDF. In the case of H-BT-CNT/PVDF, H-BT-CNT in PVDF matrix has the structure that BT coating outside of CNT. Thus, BT particles serve as blocks to reduce CNTs' mutual contacting which hinders the formation of conductive network. However, due to the coating structure, BT particles can disperse in a better mode which favors to form micro-capacitors of BT-PVDF. Meanwhile, it can reduce the possible particles' agglomeration which remains the dielectric loss at a low level

comparing with the case of M-CNT/BT/PVDF. Although, H-BT-CNT/PVDF-10% does not show percolative behivor in a low CNT volume fraction, there is the interfacial overlapping between BT and CNT due to the coating. This interfacial overlapping will possibly cause some collaborative effect among neighboring particles (far-field effect) which intensifies the effect of interfaces on the macroscopic properties of the composite and arouses strong interfacial polarization.

In the case of M-CNT/BT/PVDF, dielectric permittivity is the lowest among three samples. This illustrates that simply mechanical mixing of BT and CNT cannot have a good dielectric property. In M-CNT/BT/PVDF composite, BT particles become obstacles due to a random dispersal without any special structure which may impede CNTs and PVDF forming micro-capacitors and consequently weakens interfacial polarization. Moreover, no matter for BT particles or for CNT, neither of them has enough interfaces with this low volume fraction to achieve percolative behavior. These two reasons may cause the lowest dielectric permittivity of M-CNT/BT/PVDF among three hybrids reinforced composites. Therefore, it is the different structure of BT-CNT hybrids in the composites that causes the large variety of dielectric properties for three composites.

4.3 Partial conclusion

In this chapter, we study CNT's dispersion in PVDF matrix composite. Firstly, the theory of excluded volume has been employed to calculate f_c for H-CNT-BT/PVDF composite. A range of calculated f_c is obtained and the experimental f_c happens in the calculated range. By means of analyzing and investigating morphology parameters of H-CNT-BT including CNT's radius and length, BT's radius and the interfacial thickness, we understand better about the function of H-CNT-BT's unique structure for CNT's dispersion in PVDF which is an essential factor for achieving low percolation threshold in H-CNT-BT/PVDF composite.

Secondly, dielectric behaviors of PVDF matrix composites incorporated with

different fillers are compared with H-CNT-BT/PVDF to study structure's effect on CNT's dispersion. CNT/PVDF is the first counterpart for the comparison. By measuring AC conductivity at different depth vertical to the injection direction in the sample, we find that CNT's migration and orientation under flow especially during the injection process causes inhomogeneous dispersion in the inner composite. But H-CNT-BT/PVDF partly overcomes this negative processing effect due to the existence of BT and the unique structure. Compared with CNT/PVDF, the dispersion of CNT is more homogeneous in different depth of the composite and its conductive network is also less sensitive to thermal treatment.

Additionally, other two hybrids are incorporated into PVDF matrix and their dielectric properties are also compared with H-CNT-BT/PVDF to further demonstrate structure's effect on CNT's dispersion. It is based on the same volume fractions of CNT and BT, the structure of BT-CNT hybrids greatly affects CNT's percolative behavior in PVDF matrix and consequently differs the dielectric property from each other. Among three composites, H-CNT-BT/PVDF has the highest dielectric property due to its extremely low percolation threshold while M-CNT/BT/PVDF has the lowest dielectric property due to lacking effective interaction. Therefore, the structure of BT-CNT hybrids is crucial for achieving a good dispersion of CNT and a low percolation threshold in PVDF matrix. Carefully designing of structure can not only improve the interfacial interaction between fillers and matrix but also partly overcome inhomogeneous dispersion of CNT caused by processing which benefits for achieving a higher dielectric property.

Chapter 5 General conclusions and perspectives

_____

5.1 General conclusions

This thesis focuses on the dielectric property of BT-CNT hybrids reinforced PVDF composites via designing hybrid's structure and optimizing dispersion of CNT in PVDF matrix composite. The main results are concluded as follows:

1. The synthesis of BT-CNT hybrids

H-CNT-BT has been produced via in situ grafting CNTs on the surface of BT by CVD. CNT's weight fraction and the morphology strongly depend on experimental conditions. Firstly, the weight ratio between BT particles and catalyst $Fe(NO_3)_3 \cdot 9H_2O$ are crucial to CNT's growth and the ratio of 85:15 is studied to be effective for the synthesis. Secondly, CVD temperature also greatly influences H-CNT-BT's synthesis. An over high temperature may negatively affect obtained CNT not only in morphology but also in quality due to thermal deposition's property of acetylene. After a series of characterization and comparison by SEM and TGA, 650^oC is eventually the appropriate temperature for H-CNT-BT's preparation. Thirdly, hydrogen flow rate in the whole carrier gas is also studied for further improving the growth of CNT in H-CNT-BT and we find that 0.1*l/min* is the favorite flow rate for H-CNT-BT's synthesis.

H-BT-CNT is prepared by two steps. In the case of TBOT's hydrolysis, coating TiO_2 on the modified CNT is largely influenced by ammonia solution's content and reaction duration. A proper content of ammonia solution promotes the conversion of TiO_2 and catalyses hydrolysis reaction. Suitable reaction duration is key factor for the

morphology of TiO$_2$'s coating. We find that 0.3*ml* of ammonia solution's content and 2*h* of reaction duration are fitting for the first step. In the case of hydrothermal reaction for BT's crystallization, we find reaction temperature is essential for BT's crystallization. Meanwhile, hydrothermal reaction's duration is also important for BT's morphology deposited on the surface of CNT. By analysis of obtained experimental data, 200°*C* and 5*h* are appropriate for BT's hydrothermal condition. The obtained BT particles in the H-BT-CNT are cubic crystal phase.

2. The dielectric property of H-CNT-BT/PVDF

H-CNT-BT/PVDF composites processed by solution casting plus extrusion-injection way have high dielectric permittivity while low dielectric loss. Due to the special structure of H-CNT-BT, a much lower percolation threshold (f_{CNT}=2.77%) has been achieved compared with CNT reinforce PVDF composites by same processing way (f_{CNT}=10.4%). Furthermore, the good dispersion of CNT consequently induces β polymorph of PVDF at the interface of CNT-PVDF which further improves the dielectric property in a wide frequency range.

After thermal treatment, dielectric property of the composite is further improved even the sample are cooled to the room temperature. This dramatic increment of dielectric permittivity strongly depends on $f_{H\text{-}CNT\text{-}BT}$ and conditions of the thermal treatment including temperature, duration, multi-cycle, and cooling rate. Concretely, (1) $f_{H\text{-}CNT\text{-}BT}$ should be close to the percolation threshold so that the effective shrinkage of neighboring CNT's distance can induce the tunneling effect after thermal treatment. (2) the annealing temperature should be high enough to partly melt the crystalline part of PVDF and change amorphous layers. (3) the change of CNT's conductive network is the kinetic process which needs enough time to stabilize formed connective network. Prolonging annealing duration and multi-cycle annealing will similarly ameliorate CNT's conductive network. (4) the cooling rate also affects the final increment of dielectric permittivity due to its influences on PVDF's re-crystallization behavior.

By in-situ synchrotron X-ray characterization and modeling calculation, the increment of dielectric permittivity after thermal treatment possibly results from two

points: one possibility is the change of CNT's conductive network after thermal treatment which is probably attributed to the shrinkage of amorphous layers' thickness. The other is more amount of β polymorph is induced at the interface of CNT-PVDF due to the strong interaction of PVDF's polarity and CNT's π electrons.

3. Comparison of composites' dielectric property with different fillers

The effect of fillers' structure on CNT's dispersion is studied in chapter 4. Firstly, the theory of excluded volume has been employed to investigate the percolation threshold for H-CNT-BT/PVDF composites. The calculated percolation threshold is in agreement with the experimental data fitted by the law of percolation theory which makes the application of excluded volume valid for the modeling work. By analyzing morphology parameters of H-CNT-BT including CNT's radius and length, BT's radius and the interfacial thickness, it shows that the unique structure of H-CNT-BT improves CNT's dispersion in PVDF matrix and consequently reduces the percolation threshold.

In order to further study CNT's dispersion in the sample, H-CNT-BT/PVDF-9.5% and CNT/PVDF-8% are compared by measuring different depth's dielectric property vertical to injection direction. It is found that the core-shell structure of H-CNT-BT favors to dispense CNT in more homogeneous mode and release the negative effect by injection process. Moreover, the conductive network of H-CNT-BT/PVDF is more stable to the thermal treatment than that of CNT/PVDF composite.

Additionally, other two kinds of hybrids with different structures, namely H-BT-CNT and M-CNT/BT, are also incorporated into PVDF matrix as the references to compare the dielectric property and CNT's dispersion with H-CNT-BT/PVDF composite. The experimental results show that not all hybrids have positive effect on CNT's dispersion in PVDF. Dielectric property highly depends on hybrid's structure because the percolation threshold is largely affected by the way of BT particle's existence. By the comparison and analysis for three composites prepared by the same processing way and with the same BT and CNT's volume fraction but different BT-CNT structures, we find H-CNT-BT/PVDF has the highest dielectric property due to the unique structure of H-CNT-BT which effectively reduces the percolation

threshold. H-BT-CNT/PVDF is moderate while M-CNT-BT/PVDF is the lowest. Hence, designing an appropriate structure is the key factor for CNT's dispersion in PVDF matrix composite and achieving high dielectric property.

5.2 Perspectives

As we have mentioned in the thesis, an inhomogeneous structure in composite caused by injection process still needs to be modified. As the filler with large aspect ratio, CNT's migration and flow in the polymer matrix is largely influenced by the injection parameters. In order to achieve more homogeneous CNT's dispersion in composites, processing parameters need to be well studied including injection rate, injection pressure and difference in temperature between mold and nozzle.

H-CNT-BT's core-shell structure is partly destroyed during the blending process. The study of the morphology at different stages' blending including SEM and TEM will provide useful information about the structure's evolution and deformation during the whole processing procedure. This work is essential for optimizing the blending parameters involving the force, rotating rate and blending duration which benefits for remaining the H-CNT-BT's structure as much as possible in PVDF matrix.

In light of the calculation's result, the percolation threshold of H-CNT-BT/PVDF is associated with the aspect ratio of CNT on BT particles. It may be achieved by adjusting CVD parameters which can provide experimental results for the effect of CNT's aspect ratio on percolation threshold.

Temperature dependence of dielectric property will be recommended to conduct since it may provide more details about PVDF chains' movement during the thermal treatment, especially in the cooling stage. Temperature dependence of dielectric property will provide us more information about the polarization in PVDF's re-crystallization stage.

The difference of the thermal property between CNT and PVDF may affect the interfacial crystallization. The thermal property can be studied and the result may infer more information to understand better about the β polymorph's inducing.

[1] S.O. Kasap. Principles of electronic materials and devices. Chapter 7 Dielectric materials and insulation. Mc Graw Hill Education. 2007. P583-609

[2] Charles Kittel. Introduction to solid state physics. Chapter 6 Dielectric properties. John Wiley & Sons, Inc. 1953. P96-111

[3] Z.M. Dang, J.K. Yuan, S.H. Yao and R.J. Liao, Flexible nanodielectric materials with high permittivity for power energy storage. Advanced. Materials. 2013. 25

[4] L. Zhang and Z.Y. Cheng, Development of polymer-based 0-3 composites with high dielectric constant, Journal of Advanced Dielectrics, 2011, 1, 4, 389

[5] Z.M. Dang, J.K. Yuan, J.W. Zha, T. Zhou, S.T. Li, G.H. Hu, Fundamentals, processes and applications of high-permittivity polymer-matrix composites, Progress in Materials Science 2012. 74

[6] D. Lu, C.P. Wong (eds.), Materials for Advanced Packaging, Chapter 14 Embedded Passives. Springer SciencetBusiness Media. 2009. P460

[7] Thomas Hanemann and Dorothee Vinga Szabo. Polymer-nanoparticle composites: from synthesis to modern applications. Materials 2010. 3

[8] L.J. Qi, L. Petersson and T.L. Liu, Review of Recent Activities on Dielectric Films for Capacitor Applications. Journal of International Council on Electrical Engineering. 2014. 4

[9] M. Wang and N. Pan, Predictions of effective physical properties of complex multiphase materials. Materials Science and Engineering R. 2008. 63

[10] T. Zakri, J.P. Lanrent, M. Vauclin, Theoretical evidence for "Lichtenecker's mixture formulae's based on the effective medium theory. Journal of Physics D-Applied Physics. 1998. 31

[11] K. Wagner. The after effect in dielectrics. Arch Electrontech. 1914. 378

[12] C.W. Nan, Physics of inhomogeneous inorganic materials. Progress in Materials Science. 1993. 37

[13] C.W. Nan, Y. Shen, and J. Ma, Physical properties of composites near percolation. The Annual Review of materials Research. 2010. 40

[14] A.L. Efros, B.I. Shklovskii. Physica Status Solidi (B). 1976. 76

[15] T J Lewis, Interfaces are the dominant feature of dielectrics at the nanometric level. IEEE Transaction on dielectric and electrical insulation. 2004. 11

[16] T. Tanaka, M. Kozako, N. Fuse, Y. Ohki, Proposal of a multi-core model for polymer nanocomposite dielectrics. IEEE Transaction on dielectric and electrical insulation. 2005. 12

[17] S.T. Li, G.L.Yin, G.Chen, J.Y.Li, S.N. Bai, L.S. Zhong, Y.X. Zhang and

Q.Q.Lei, Short-term breakdown and long-term failure in nanodielectrics: A review, IEEE Transaction on dielectric and electrical insulation. 2010. 17

[18]   B.Balasubramanian, K.L.Kraemer, N.A.Reding, R.Skomski,S.Ducharme and D.J. Sellmyer, Synthesis of Monodisperse TiO_2−Paraffin Core−Shell Nanoparticles for Improved Dielectric Properties. ACS Nano. 2010. 4

[19]   C. Zou, D. Kushner, S. Zhang, Wide temperature polyimide/ZrO_2 nanodielectric capacitor film with excellent electrical performance. Applied Physics Letters. 2011. 98

[20]   B.H. Fan, J.W. Zha, D.R. Wang, J. Zhao, Z.F. Zhang, Z.M. Dang, Preparation and dielectric behaviors of thermoplastic and thermosetting polymer nanocomposite films containing $BaTiO_3$ nanoparticles with different diameters. Composites Science and Technology. 2013. 80

[21]   B.H. Fan, J.W. Zha, D.R. Wang, J. Zhao, Z.M. Dang, Size-dependent low-frequency dielectric properties in the $BaTiO_3$/poly(vinylidene fluoride) nanocomposite films. Applied Physics Letter. 2012. 100

[22]   B.H. Fan, J.W. Zha, D.R. Wang, J. Zhao, Z.M. Dang, Experimental study and theory prediction of dielectric permittivity in $BaTiO_3$/Polyimide nanocomposite films. Applied Physics Letter. 2012.100

[23]   Z.M. Dang, T. Zhou, S.H. Yao, J.K. Yuan, J.W. Zha, H.T. Song, J.Y. Li, Q. Chen, W.T. Yang, J. Bai, Advanced calcium copper titanate/polyimide functional hybrid films with high dielectric permittivity. Advanced Materials. 2009. 21

[24]   H. Tang, Y. Lin, H.A. Sodano, Enhanced energy storage in nanocomposite capacitors through aligned PZT nanowires by uniaxial strain assembly. Advanced Energy Materials. 2012. 2

[25]   Z.M. Dang, H.P. Xu, H.Y. Wang, Significantly enhanced low-frequency dielectric permittivity in the $BaTiO_3$/poly(vinylidenefluoride) nanocomposite. Applied Physics Letter. 2007. 90

[26]   S.O. Kasap. Principles of electronic materials and devices. Chapter 7 Dielectric materials and insulation. Mc Graw Hill Education. 2007. P647-653

[27]   Charles Kittel. Introduction to solid state physics. Chapter 7 Ferroelectric crystals. John Wiley & Sons, Inc. 1953. P116-117

[28]   P. Kim, N.M. Doss, J.P. Tillotson, P.J. Hotchkiss, M.J. Pan, S.R. Marder, J.Y. Li, J.P. Calame and J.W. Perry, High energy density nanocomposites based on surface-modified $BaTiO_3$ and a ferroelectric polymer. ACS Nano. 2009. 3

[29]   D.H. Kuo, C.C. Chang, T.Y. Su, W.K. Wang, B.Y. Lin, Dielectric properties of three ceramic/epoxy composites. Materials Chemistry and Physics. 2004. 85

[30]   T. Zhou, J.W. Zha, R.Y. Cui, B.H. Fan, J.K. Yuan and Z.M. Dang, Improving dielectric properties of $BaTiO_3$/ferroelectric polymer composites by employing surface hydroxylated $BaTiO_3$ nanoparticles. ACS Applied Materials and Interfaces. 2011. 3

[31]   L. Xie, X. Huang, C. Wu, P. Jiang, Core-shell structured poly (methyl methacrylate)/$BaTiO_3$ nanocomposites prepared by in situ atom transfer

radical polymerization: a route to high dielectric constant. Journal of Materials Chemistry. 2011. 21

[32] Iijima S. Helical microtubules of graphitic carbon. Nature. 1991. 354

[33] M.T. Byrne and Y.K. Gun'ko, Recent advances in research on carbon nanotube-polymer composites. Advanced Materials. 2010. 22

[34] M. Kumar and Y. Ando, Chemical vapor deposition of carbon nanotubes: a review on growth mechanism and mass production. Journal of Nanoscience and nanotechnology. 2010. 10

[35] A.C. Dupuis, The catalyst in the CCVD of carbon nanotubes—a review. Progress in Materials Science. 2005. 50

[36] M.A. Ermakova, D.Y. Ermakov, A.L. Chuvilin, G.G. Kuvshinov. Decomposition of methane over iron catalysts at the range of moderate temperatures: the influence of structure of the catalytic systems and the reaction conditions on the yield of carbon and morphology of carbon filaments. Journal of catalysis.2001. 201

[37] S.S. Pan, Z.W. Xie, B.H. Chang, L.F. Sun, W.Y. Zhou, G. Wang. Direct growth of aligned open carbon nanotubes by chemical vapor deposition. Chemical Physics Letters. 1999. 299

[38] R.R. Bacsa, C. Laurent, A. Peigney, W.S. Bacsa, T. Vaugien, A. Rousset. High specific surface area carbon nanotubes from catalytic chemical vapor deposition process. Chemical Physics Letters. 2000. 323

[39] J.P. Pinheiro, M.C. Schouler, P. Gadelle. Nanotubes and nanofilaments from carbon monoxide disproportionation over Co/MgO catalysts I. Growth versus catalyst state. Carbon. 2003. 41

[40] Y. Li, J. Liu, Y. Wang, Z.L. Wang. Preparation of monodispersed Fe-Mo nanoparticles as the catalyst for CVD synthesis of carbon nanotubes. Chemistry of Materials. 2001.13

[41] C.L. Cheung, A. Kurtz, H. Park, C.M. Lieber. Diameter-controlled synthesis of carbon nanotubes. Journal of Physical Chemistry B. 2002.106

[42] A. Dichiara, Y. Lin, D. He and J. Bai, Bio-inspired method to improve the carbon nanotube adhesion strength onto substrates. Science of Advanced materials. 2014. 6

[43] W.K. Li, D.L. He, Z.M. Dang and J.B. Bai, In situ damage sensing in the glass fabric reinforced epoxy composites containing CNT-Al_2O_3 hybrids. Composites Sciences and Technology. 2014. 99

[44] Y.Q. Lin, A. Dichiara, D.L. He, P. Haghi-Ashtiani, J.B. Bai, Uniform diameter multi-walled carbon nanotubes with a controlled wall number obtained by a simple chemical vapor deposition method. Chemical Physics Letters. 2012. 554

[45] W.K. Li, A. Dichiara, J.B. Bai, Carbon nanotube-graphene nanoplatelet hybrids as high-performance multifunctional reinforcements in epoxy composites. Composites Science and Technology. 2013. 74

[46] W.L. Li, J.K. Yuan, Y.L. Lin, S.H. Yao, Z.Y. Ren, H. Wang, M.Q. Wang, J.B. Bai, The controlled formation of hybrids structures of multi-walled carbon

nanotubes on SiC plate-like particles and their synergetic effects as a fillers in poly(vinglidene fluoride) based composites. Carbon. 2013. 51

[47]   W.K. Li, J.K. Yuan, A. Dichiara, Y.Q. Lin, J.B. Bai, The use of vertically aligned carbon nanotubes grown on SiC for in situ sensing of elastic and plastic deformation in electrically percolative epoxy composites. Carbon. 2012. 50

[48]   R.T.K. Baker, Catalytic growth of carbon filaments. Carbon 1989. 27

[49]   S.B. Sinnott, R. Andrews, D. Qian, A.M. Rao, Z. Mao, E.C. Dickey, F. Derbyshire, Model of carbon nanotube growth through chemical vapor deposition. Chemical Physics Letters. 1999. 315

[50]   H.C. Wu, X.L. Chang, L. Liu, F. Zhao and Y.L. Zhao, Chemistry of carbon nanotubes in biomedical applications. Journal of Materials Chemistry. 2010. 20

[51]   H. Kitano, K. Tachimoto, M. Gemmei-Ide, N. Tsubaki, Interaction between polymer chains covalently fixed to single-walled carbon nanotubes. Macromolecular Chemistry and Physics. 2006. 207

[52]   Eric D. Laird and Christopher Y. Li, Structure and morphology control in crystalline polymer−carbon nanotube nanocomposites. Macromolecules. 2013. 46

[53]   N.G. Sahoo, S. Rana, J.W. Cho, L. Li, S.H. Chan, Polymer nanocomposites based on functionalized carbon nanotubes. Progress Polymer Science. 2010. 35

[54]   F. Husszin, M. Hojjati, Polymer-matrix nanocomposites, processing, manufacturing, and application: An overview, Journal of composite materials. 2006. 40

[55]   S.W. Kim, T. Kim, Y.S. Kim, H.S. Choi, H.J. Lim, S.J. Yang, C.R. Park, Surface modifications for the effective dispersion of carbon nanotubes in solvents and polymers. Carbon. 2012. 50

[56]   Y.Y. Huang and E. M. Terentjev, Dispersion of carbon nanotubes: Mixing, sonication, stabilization, and composite properties. Polymers. 2012. 4

[57]   L.D. Tijinga, C.H.Parkb, W.L.Choia, M.T.G. Rueloa, A. Amarjargal, H.R. Pant, I.T.Im, C.S. Kim, Characterization and mechanical performance comparison of multiwalled carbon nanotube/polyurethane composites fabricated by electrospinning and solution casting. Composites Part B: Engineering. 2013. 44

[58]   Z.M. Dang, S.H. Yao, J.K. Yuan, J.B. Bai, Tailored dielectric properties based on mictrostructure change in $BaTiO_3$-carbon nanotube/polyvinylidene fluoride three-phase nanocomposites. Journal of physical chemistry C. 2010, 114

[59]   H. Xia, Q. Wang, G. Qiu, Polymer-encapsulated carbon nanotubes prepared through ultrasonically initiated in situ emulsion polymerization. Chemistry of materials. 2003. 15

[60]   S. Yu, W. Zheng, W. Yu, Y. Zhang, Q. Jiang, and Z. Zhao, Formation mechanism of β-Phase in PVDF/CNT composite prepared by the sonication

method. Macromolecules. 2009. 42

[61]   H. Zhang, Z. Zhang, Impact behavior of polypropylene filled with multi-walled carbon nanotubes. European Polymer Journal. 2007. 43

[62]   W. Tang, M.H. Santare, S.G. Advani. Melt processing and mechanical property characterization of multi-walled carbon nanotube/high density polyethylene (MWNT/HDPE) composite films. Carbon. 2003. 41

[63]   P. Potschke, A.R. Bhattacharyya, A. Janke, Melt mixing of polycarbonate with multiwalled carbon nanotubes: microscopic studies on the state of dispersion. European Polymer Journal. 2004. 40

[64]   R.E. Gorga, R.E. Cohen, Toughness enhancements in poly(methylmethacrylate) by addition of oriented multiwall carbon nanotubes. Journal of Polymer Science Part B: Polymer Physics. 2004. 42

[65]   Y. Zeng, Z. Ying, J. Du, H.M. Cheng, Effects of carbon nanotubes on processing stability of polyoxymethylene in melt-mixing process. The journal of physical chemistry. 2007. 111

[66]   O. Meincke, D. Kaempfer, H. Weickmann, C. Friedrich, M. Vathauer, H. Warth, Mechanical properties and electrical conductivity of carbon-nanotube filled polyamide-6 and its blends with acrylonitrile/butadiene/styrene. Polymer. 2004. 45

[67]   S. Pegel, P. Po¨tschke, G. Petzold, I. Alig, S. M. Dudkin, D. Lellinger, Dispersion, agglomeration, and network formation of multiwalled carbon nanotubes in polycarbonate melts. Polymer. 2008. 49

[68]   S.N. Li, B. Li, Z.M. Li, Q. Fu, K.Z. Shen, Morphological manipulation of carbon nanotube/polycarbonate/polyethylene composites by dynamic injection packing molding. Polymer. 2006. 47

[69]   T. Villmow, S. Pegel, P. Potschke, U.Wagenknecht, Influence of injection molding parameters on the electrical resistivity of polycarbonate filled with multi-walled carbon nanotubes. Composites Science and Technology. 2008. 68

[70]   J.W. Zha, B.H. Fan, Z.M. Dang, S.T. Li, and G. Chen, Microstructure and electrical properties in three-component $(Al_2O_3–TiO_2)$/polyimide nanocomposite films. Journal of Materials Research. 2010. 25

[71]   Z.M. Dang, Y.Q. Lin, H.P. Xu, C.Y. Shi, S.T. Li, J.B. Bai, Fabrication and dielectric characterization of advanced BaTiO3/polyimide nanocomposite films with high thermal stability. Advanced Functional Materials. 2008. 18

[72]   N. Hu, H. Zhou, G. Dang, X. Rao, C. Chen, W. Zhang, Efficient dispersion of multi-walled carbon nanotubes by in situ polymerization. Polymer international. 2007. 56

[73]   M. Cochet, W.K. Maser, A.M. Benito, M.A. Callejas, M.T. Martinez, J.M. Benoit, J. Schreiber and O. Chauvet, Synthesis of a new polyaniline/nanotube composites: "in-situ" polymerization and charge transfer through site-selective interaction. Chemical Communications. 2001. 21

[74]   N.G. Sahoo, Y.C. Jung, H.H. So, J.W. Cho, Polypyrrole coated carbon nanotubes: synthesis, characterization, and enhanced electrical properties.

Synthetic Metals. 2007. 157

[75]   T.J. Kang, M. Cha, E.Y. Jang, J. Shin, H.U. Im, Y. Kim, J. Lee, Y.H. Kim, Ultra-thin and Conductive Nanomembrane Arrays for Nanomechanical Transducers. Advanced Materials. 2008. 20

[76]   B. S. Shim, P. Podsiadlo, D. G. Lilly, A. Agarwal, J. Leet, Z. Tang, S. Ho, P. Ingle, D. Paterson, W. Lu, N. A. Kotov, Nanostructured Thin Films Made by Dewetting Method of Layer-By-Layer Assembly. Nano Letters. 2007. 7

[77]   S. Srivastava, N. A. Kotov, Composite Layer-by-Layer (LBL) Assembly with Inorganic Nanoparticles and Nanowires, Accounts of chemical research. 2008. 41

[78]   B. S. Shim, W. Chen, C. Doty, C. L. Xu, N. A. Kotov, Smart Electronic Yarns and Wearable Fabrics for Human Biomonitoring made by Carbon Nanotube Coating with Polyelectrolytes. Nano Letters. 2008. 8

[79]   M. Endo, H. Muramatsu, T. Hayashi, Y. A. Kim, M. Terrones, N. S. Dresselhaus, Nanotechnology: 'Buckypaper' from coaxial nanotubes. Nature. 2005. 433

[80]   S. D. Bergin, V. Nicolosi, P. V. Streich, S. Giordani, Z. Y. Sun, A. H. Windle, P. Ryan, N. P. P. Niraj, Z. T. T. Wang, L. Carpenter, W. J. Blau, J. J. Boland, J. P. Hamilton, J. N. Coleman, Towards Solutions of Single-Walled Carbon Nanotubes in Common Solvents. Advanced Materials. 2008. 20

[81]   W. Ding, S. Pengcheng, L. Changhong, W. Wei, F. Shoushan, Highly oriented carbon nanotube papers made of aligned carbon nanotubes. Nanotechnology. 2008. 7

[82]   E. Fukada, S. Tasaka, H. Nalwa, Ferroelectric Polymers. Nalwa, H., Ed. Marcel Dekker: New York. 1995. p 353

[83]   Seiler DA. In: Scheirs J, ed. Modern Fluoropolymers. Chichester: John Wiley & Sons, 1997. p 487.

[84]   R.E. Cais, J.M. Kometani, New isomers of poly(vinyl fluoride) with controlled regiosequence microstructure. Polymer. 1988. 29

[85]   H. Nakano, K. Shimizu, S. Takahashi, A. Kono, T. Ougizawa, H. Horibe, Resistivity-temperature characteristics of filler-dispersed polymer composites. Polymer. 2012. 53

[86]   R. G. Jr. E. M. UENO, Effect of crystalline phase, orientation and temperature on the dielectric properties of poly (vinylidene fluoride) (PVDF). Journal of materials science. 1999. 34

[87]   C.H. Du, B.K. Zhu, Y.Y. Xu, Effects of stretching on crystalline phase structure and morphology of hard elastic PVDF fibers. Journal of Applied Polymer Science. 2007. 24

[88]   R. G. Jr. Determination of the α, β, and γ crystalline phases of poly(vinylidene fluoride) films prepared at different conditions. Journal of Applied Polymer Science. 2006. 100

[89]   C. Marega, A. Marigo, Influence of annealing and chain defects on the melting behaviour of poly(vinylidene fluoride). European Polymer Journal. 2003. 39

[90] B.S. Ince-Gunduz, R.t Alpern, D. Amare, J. Crawford, B. Dolan, S. Jones, R. Kobylarz, M. Reveley, P. Cebe, Impact of nanosilicates on poly(vinylidene fluoride) crystal polymorphism: Part 1. Melt-crystallization at high supercooling. Polymer. 2010. 51

[91] M. Bohlen and K. Bolton. Inducing the β-phase of poly(vinylidene fluoride) – a review. Annual review of nanoscience and nanotechnology. 2015. 1 150110

[92] A. Hartono1, S. Satira, M. Djamal, R. Ramli, H. Bahar, E. Sanjaya, Effect of mechanical treatment temperature on electrical properties and crystallite size of PVDF film. Advances in Materials Physics and Chemistry. 2013. 3

[93] A. Lund, and B. Hagström, Melt spinning of poly(vinylidene fluoride) fibers and the influence of spinning parameters on β-phase crystallinity. Journal of Applied Polymer Science. 2010. 116

[94] H. Su, A. Starchan, and W. A. Goddard III, Density functional theory and molecular dynamics studies of the energetics and kinetics of electroactive polymers: PVDF and P(VDF-TrFE). Physical Review B. 2004. 70

[95] KP Pramoda, A. Mohamed, I.Y. Phang and T.X. Liu, Crystal transformation and thermomechanical properties of poly(vinylidene fluoride)/clay nanocomposites. Polymer International. 2005. 54

[96] B.E. El Mohajir, and N. Heymans, Changes in structural and mechanical behaviour of PVDF with processing and thermo-mechanical treatments. 1. Change in structure. Polymer. 2001. 42

[97] A. Salimi, and A. A. Yousefi, FTIR studies of β-phase crystal formation in stretched PVDF films. Polymer Testing. 2003. 22

[98] M. M. D. Ramos, H. M. G. Correia, and S. Lanceros-Méndez, Atomistic modelling of processes involved in poling of PVDF. Computational Materials Science. 2005. 33

[99] K. C. Satyanarayana, and K. Bolton, Molecular dynamics simulations of α- to β-poly(vinylidene fluoride) phase change by stretching and poling. Polymer. 2012. 53

[100] M. Bohlen, and K. Bolton, Effect of single wall carbon nano-tubes on the conformation of Poly(vinylidene fluoride). Quantum Matter. 2014. 3

[101] E. Erdtman, K. C. Satyanarayana, and K. Bolton, Simulation of α- and β-PVDF melting mechanisms. Polymer. 2012. 53

[102] B.J. Chu, X. Zhou, K.L. Ren, B. Neese, M.R. Lin, Q. Wang, F. Bauer, Q. M. Zhang, A dielectric polymer with high electric energy density and fast discharge speed. Science. 2006. 313

[103] B. Ploss, B. Ploss, Dielectric nonlinearity of PVDF–TrFE copolymer. Polymer. 2000. 41

[104] L. Zhu and Q. Wang, Novel ferroelectric polymers for high energy density and low loss dielectrics. Macromolecules. 2012. 45

[105] L. Zhu, Exploring strategies for high dielectric constant and low loss polymer dielectrics. Journal of Physical Chemistry Letters. 2014. 5

[106] R. W. Holman, and G. J. Kavarnos, A molecular dynamics investigation of

the structural characteristics of amorphous and annealed poly(vinylidene fluoride) and vinylidene fluoride-trifluoroethylene copolymers. Polymer. 1996. 37

[107] S. S. Je, T. Sharma, Y. Lee, B. Gill, and J. X. Zhang, A thin-film piezoelectric PVDF-TrFE based implantable pressure sensor using lithographic patterning, in Proceedings of IEEE Conference on Micro Electro Mechanical Systems (IEEE, 2011). P644-647

[108] P. Costa, J. Silva, V. Sencadas, C.M. Costa, F.W.J. van Hattum, J.G. Rocha, S. Lanceros-Mendez, The effect of fiber concentration on the α to β-phase transformation, degree of crystallinity and electrical properties of vapour grown carbon nanofiber/poly(vinylidenefluoride) composites. Carboon. 2009. 47

[109] G.H. Kim, S.M. Hong and Y. Seo, Piezoelectric properties of poly(vinylidene fluoride) and carbon nanotube blends: β-phase development. Physical Chemistry Chemical Physics. 2009. 11

[110] N. Levi, R. Czerw, S. Xing, P. Iyer, and D.L. Carroll, Properties of polyvinylidene difluoride-carbon nanotube blends, Nano Letters. 2004. 4

[111] P. Sajkiewicz, A. Wasiak, and Z. Gocłowski, Phase transitions during stretching of poly(vinylidene fluoride). European Polymer Journal. 1999. 35

[112] E. Nilsson, A. Lund, C. Jonasson, C. Johansson, and B. Hagstom, Poling and characterization of piezoelectric polymer fibers for use in textile sensors. Sensors and Actuators A. 2013. 201

[113] K. C. Satyanarayana, and K. Bolton, Molecular dynamics simulations of α- to β-poly(vinylidene fluoride) phase change by stretching and poling. Polymer. 2012. 53

[114] R.G. Jr., and M. Cestari, Effect of Crystallization Tem-perature on the Crystalline Phase Content and Morphology of Poly(vinylidene Fluoride). Journal of Polymer Science Part B: Polymer Physics. 1994. 32

[115] Z. Guo, E. Nilsson, M. Rigdahl, and B. Hagström, Melt spinning of PVDF fibers with enhanced β phase structure. Journal of Polymer Science. 2013. 130

[116] N. Levi, R. Czerw, S. Xing, P. Iyer, and D. L. Carroll, Properties of polyvinylidene difluoride-carbon nanotube blends. Nano letters. 2004. 4

[117] S. Manna, and A. K. Nandi, Piezoelectric β polymorph in poly(vinylidene fluoride)-functionalized multiwalled carbon nanotube nanocomposite films. Journal of Physical Chemistry C. 2007. 111

[118] M. El Achaby, F.E. Arrakhiz, S. Vaudreuil, E.M. Essassi, A. Qaiss, and M. Bousmina, Nanocomposite films of poly(vinylidene fluoride) filled with polyvinylpyrrolidone-coated multiwalled carbon nanotubes: enhancement of β-polymorph formation and tensile properties. Polymer Engineering and Science. 2013. 53

[119] M. Pérez-Cabero, I. Rodríguez-Ramos, A. Guerrero-Ruíz, Characterization of carbon nanotubes and carbon nanofibers prepared by catalytic decomposition of acetylene in a fluidized bed reactor. Journal of Catalysis. 2003. 215

[120] O.A. Nerushev, S. Dittmar, R.E. Morjan, F. Rohmund and E.E.B. Campbell, Particle size dependence and model for iron-catalyzed growth of carbon nanotubes by thermal chemical vapor deposition. Journal of Applied Physics. 2003. 93

[121] R.E. Morjan, O.A. Nerushev, M. Sveningsson, F. Rohmund, L.K.L. Falk, E.E.B. Campbell, Growth of carbon nanotubes from C60. Applied Physics A. 2004. 78

[122] A. Loiseau, P. Launois, P. Petit, S. Roche, J.P. Salvetat. Understanding carbon nanotubes from basics to application. Springer. Chapter 2 Synthesis methods and growth mechanisms. P64-65

[123] D.L. He, M. Bozlar, M. Genestoux, J. Bai. Diameter- and length-dependent self-organizations of multi-walled carbon nanotubes on spherical alumina microparticles. Carbon. 2010. 48

[124] P. Wang, D. Chen and F.Q. Tang, Preparation of Titania-Coated Polystyrene Particles in Mixed Solvents by Ammonia Catalysis. Langmuir. 2006. 22

[125] Q.M. Cao, Q.M. Yu, D.W. Connell, G. Yu, Titania/carbon nanotube composite (TiO_2/CNT) and its application for removal of organic pollutants. Clean Technologies and Environmental Policy. 2013. 15

[126] X.C. Jiang, T. Herricks and Y.N. Xia, Monodispersed spherical colloids of titania: synthesis, characterization and crystallization. Advanced Materials. 2003. 15

[127] W. Li, J.P. Yang, Z.X. Wu, J.X. Wang, B. Li, S.S. Feng, Y.H. Deng, F. Zhang, and D.Y. Zhao, A versatile kinetics-controlled coating method to construct uniform porous TiO_2 shells for multifunctional core−shell structures. Journal of the American Chemical Society. 2012. 134

[128] C. Bi, M.F. Zhu, Q.H. Zhang, Y.G. Li, H.Z. Wang, Electromagnetic wave absorption properties of multi-walled carbon nanotubes decorated with La-doped $BaTiO_3$ nanocrystals synthesized by a solvothermal method. Materials Chemistry and Physics. 2011. 126

[129] Q. Huang and L. Gao, Manufacture and electrical properties of multiwalled carbon nanotube/$BaTiO_3$ nanocomposite ceramics. Journal of Materials Chemistry. 2004. 14

[130] Q. Huang, L. Gao, Y.Q. Liu and J. Sun, Sintering and thermal properties of multiwalled carbon nanotube–$BaTiO_3$ Composites. Journal of Materials Chemistry. 2005. 15

[131] X. Huang, Z.J. Pu, M.N. Feng, L.F. Tong and X.B. Liu, $BaTiO_3$@MWCNT score/shell nanotubes embedded PEN nanocomposite films with high thermal stability and high permittivity. Materials Letters. 2013. 96

[132] X. Huang, M.N. Feng, X.B. Liu, Synergistic enhancement of dielectric constant of novel core/shell $BaTiO_3$@MWCNTs/PEN nanocomposites with high thermal stability. Journal of Materials Science: Materials in Electronics. 2014. 25

[133] J.C. Rendón-Angeles, Z. Matamoros-Veloza and K. Yanagisawa, Crystallization – Science and Technology. Chapter 8 Preparation of selected

ceramic compounds by controlled crystallization under hydrothermal conditions. P215-219

[134] S.N. Li, B. Li, Z.M. Li, Q. Fu, K.Z. Shen, Morphological manipulation of carbon nanotube/polycarbonate/polyethylene composites by dynamic injection packing molding. Polymer. 2006. 47

[135] R.J. Crowson, M.J. Folkes, and P. F. Bright, Rheology of short glass fiber-reinforced thermoplastics and its application to injection molding 1. Fiber motion and viscosity measurement. Polymer Engineer and Science. 1980. 20

[136] S.S. Katti and J.M. Schultz, The microstructure of injection-molded semicrystalline polymers: A review. Polymer Engineer and Science. 1982. 22

[137] N. Hu, Z. Masuda, C. Yan, H. Fukunaga and T. Hashida. The electrical properties of polymernanocomposites with carbon nanotube fillers. Nanotechnology. 2008. 19

[138] Y.B. Yi and E. Tawerghi, Geometric percolation thresholds of interpenetrating plates in three-dimensional space. Physical Review E. 2009. 79

[139] N. Hu, Y. Karube, M. Arai, T. Watanabe, C. Yan,Y. Li, Y.L. Liu, H. Fukunaga, Investigation on sensitivity of a polymer/carbon nanotube composite strain sensor. Carbon. 2010. 48

[140] F. Dalmas, R. Dendievel, L. Chazeau, J.Y. Cavaille, C. Gauthier, Carbon nanotube-filled polymer composites: Numerical simulation of electrical conductivity in three-dimensional entangled fibrous networks. Acta Materialia. 2006. 54

[141] N. Hu, Y. Karube, C. Yan, Z. Masuda, H. Fukunaga, Tunneling effect in a polymer/carbon nanotube nanocomposite strain sensor. Acta Materialia. 2008. 56

[142] A.V. Kyrylyuk and Paul van der Schoot, Continuum percolation of carbon nanotubes in polymeric and colloidal media. PNAS. 2008. 105

[143] A.B. Oskouyi, P. Mertiny, Monte Carlo model for the study of percolation thresholds in composites filled with circular conductive nano-disks. Procedia Engineering. 2010. 10

[144] Y. Kinoshita, M. Kawachi, T. Matsuura, N. Ohno, Axial buckling behavior of wavy carbon nanotubes: A molecular mechanics study. Physica E. 2013. 54

[145] R. Rahman and P. Servati, Effects of inter-tube distance and alignment on tunneling resistance an strain sensitivity of nanotube/polymer composite films. Nanotechnology. 2012. 23

[146] Andrzej Lasia, Electrochemical Impedance Spectroscopy and its Applications. Springer, 2014. P145

[147] M. Gałązka, E. Juszyńska-Gałązka, N. Osiecka, M. Massalska-Arodź, and A. Bąk, On new scaling of dielectric response. Journal Of Applied Physics. 2015. 118

[148] Argonne National Laboratory, The advanced photon source, a national synchrotron radiation research facility. ANL/APS/TB-25-Rev. 1997

[149] N.S. Murthy and H. Minor, General procedure for evaluating amorphous

scattering and crystallinity from X-ray diffraction scans of semi-crystalline polymers. Polymer. 1990. 31

[150] S. Rabiej and M. Rabiej, Determination of the parameters of lamellar structure of semi-crystalline polymers using a computer program SASDAT. Polymer. 2011. 56

[151] A. Wurm, D. Lellinger, A.A. Minakov, T. Skipa, P. Pötschke, R. Nicula, I. Alig, C. Schick, Crystallization of poly(ε-caprolactone)/MWCNT composites: A combined SAXS/WAXS, electrical and thermal conductivity study. Polymer. 2014. 55

[152] B. Chu and B. S. Hsiao, Small-angle X-ray scattering of polymers, Chemical Reviews. 2001. 101

[153] I. Alig, T. Skipa, D. Lellinger, M. Bierdel and H. Meyer, Dynamic percolation of carbon nanotube agglomerates in a polymer matrix: comparison of different model approaches. Basic Solid State Physics. 2008. 254

[154] C. Zhang, P. Wang, C.A. Ma, G.A. Wu, M. Sumita, Temperature and time dependence of conductive network formation: Dynamic percolation and percolation time. Polymer.2006. 47

[155] F.M. Du, R.C. Scogna, W. Zhou, S. Brand, J.E. Fischer and K.I. Winey, Nanotube networks in polymer nanocomposites: rheology and electrical conductivity. Macromolecules 2004, 37

[156] C. Su, L.H. Xu, C. Zhang and J. Zhu, Selective location and conductivity network formation of multiwalled carbon nanotubes in polycarbonate/poly(vinylidene fluoride) blends. Composites Sciences and Technology. 2011. 71

[157] H. Deng, L. Lin, M.Z. Ji, S.M. Zhang, M.B. Yang and Q. Fu, Progress on the morphological control of conductive network in conductive polymer composites and the use as electroactive multifunctional materials. Progress in Polymer Science. 2014. 39

[158] I. Alig, P. Potschke, D. Lellinger. T. Skipa, S. Pegel, G.R. Kasaliwal and T. Villmow, Establishment, morphology and properties of carbon nanotube networks in polymer melts. Polymer. 2012. 53

[159] H. Deng, T. Skipa, E. Bilotti, R. Zhang, D. Lellinger, L. Mezzo, Q. Fu, I. Alig, and T. Peijs, Preparation of high-performance conductive polymer fibers through morphological control of networks formed by nanofillers. Advanced Functional materials. 2010. 20

[160] N.Y. Ning, S.R. Fu, W. Zhang, F. Chen, K. Wang, H. Deng, Q. Zhang and Q. Fu, Realizing the enhancement of interfacial interaction in semicrystalline polymer/filler composites via interfacial crystallization. Progress in Polymer Science. 2012. 37

[161] I. Balberg, C. H. Anderson, S. Alexander and N. Wagner, Excluded volume and its relation to the onset of percolation. Physical Review B. 1984. 30

[162] L. Berhan and A.M. Sastry, Modeling percolation in high-aspect-ratio fiber systems. Physical Review E. 2007. 75

[163] N. Hu, Z. Masuda, C. Yan, G. Yamamoto, H. Fukunaga1 and T. Hashida, The

electrical properties of polymer nanocomposites with carbon nanotube fillers. Nanotechnology. 2008. 19

[164]   Y. B. Yi and E. Tawerghi, Geometric percolation thresholds of interpenetrating plates in three-dimensional space. Physical Review E. 2009. 79

[165]   R. Zallen, The physics of amorphous solids. Wiley. New York. 1983